

Design Studies and Sensor Tests for the Beam Calorimeter of the ILC Detector

DISSERTATION

zur Erlangung des akademischen Grades
doctor rerum naturalium
(Dr. rer. nat.)
im Fach Physik

eingereicht an der
Mathematisch-Naturwissenschaftlichen Fakultät I
Humboldt-Universität zu Berlin

von

Frau Magister Ekaterina Kuznetsova
geboren am 10.08.1976 in Leningrad, USSR

Präsident der Humboldt-Universität zu Berlin:
Prof. Dr. Hans Jürgen Prömel

Dekan der Mathematisch-Naturwissenschaftlichen Fakultät I:
Prof. Thomas Buckhout, PhD

Gutachter:

1. Prof. Dr. Hermann Kolanoski
2. Prof. Dr. Thomas Lohse
3. Prof. Dr. Achim Stahl

eingereicht am: 30. November 2005
Tag der mündlichen Prüfung: 20. April 2006

Abstract

The International Linear Collider (ILC) is being designed to explore particle physics at the TeV scale. The design of the Very Forward Region of the ILC detector is considered in the presented work. The Beam Calorimeter - one of two electromagnetic calorimeters situated there - is the subject of this thesis.

The Beam Calorimeter has to provide a good hermeticity for high energy electrons, positrons and photons down to very low polar angles, serve for fast beam diagnostics and shield the inner part of the detector from backscattered beamstrahlung remnants and synchrotron radiation.

As a possible technology for the Beam Calorimeter a diamond-tungsten sandwich calorimeter is considered. Detailed simulation studies are done in order to explore the suitability of the considered design for the Beam Calorimeter objectives. Detection efficiency, energy and angular resolution for electromagnetic showers are studied. At the simulation level the diamond-tungsten design is shown to match the requirements on the Beam Calorimeter performance.

Studies of polycrystalline chemical vapour deposition (pCVD) diamond as a sensor material for the Beam Calorimeter are done to explore the properties of the material. Results of the measurements performed with pCVD diamond samples produced by different manufacturers are presented.

Keywords:

ILC, Beam Calorimeter, diamond, electromagnetic calorimeter

Zusammenfassung

Der zukünftige Linearbeschleuniger (International Linear Collider - ILC) wird für die Teilchenforschung im Energiebereich bis zu einem Tera-Elektronenvolt (TeV scale) entwickelt. In dieser Arbeit wird der Entwurf des inneren Vorwärtsbereichs (Very Forward Region) eines Detektors für diesen Beschleuniger beschrieben. Das Beam-Kalorimeter - eines der zwei elektromagnetischen Kalorimeter, die hier angeordnet sind - ist Gegenstand dieser Arbeit.

Das Beam-Kalorimeter muß eine gute Hermetizität für hochenergetische Elektronen, Positronen und Photonen bis hinab zu sehr kleinen Polarwinkeln gewährleisten. Es dient für die schnelle Strahldiagnose und als Abschirmung des inneren Detektors gegen rückgestreute Beamstrahlungsreste und Synchrotronstrahlung.

Als eine mögliche Technologie für das Beam-Kalorimeter wird eine Sandwich-Anordnung aus Diamantsensoren und Wolfram-Absorberplatten betrachtet. Es werden detaillierte Simulationen einer solchen Anordnung durchgeführt. Die Nachweiseffektivität und die Energie- sowie Winkelauflösung für elektromagnetische Schauer werden untersucht. Im Ergebnis der Simulationsrechnungen wird nachgewiesen, dass die vorgeschlagene Anordnung die Anforderungen an ein Beam-Kalorimeter erfüllt.

Zusätzlich werden Untersuchungen an polykristallinem Diamantmaterial, hergestellt mittels Abscheidung aus der Dampfphase (Chemical Vapour Deposition - CVD), durchgeführt, um dessen Eigenschaften als Sensormaterial für ein Beam-Kalorimeter zu ermitteln. Die Ergebnisse der Messungen von Mustern verschiedener Hersteller werden dargestellt diskutiert.

Schlagwörter:

ILC, Beam-Kalorimeter, Diamant, elektromagnetisches Kalorimeter

Contents

1	Introduction	1
2	Physics case of the ILC	3
2.1	The ILC parameters	5
2.2	The requirements on the ILC detector	6
2.3	The ILC detector	9
3	Very Forward Region	13
3.1	Luminosity Calorimeter	14
3.2	Beam Calorimeter	18
4	Simulation studies of the diamond-tungsten Beam Calorimeter	27
4.1	Simulation	27
4.2	Reconstruction	29
4.3	Fake rate and detection efficiency	30
4.4	Energy resolution	34
4.5	Angular resolution	41
5	CVD diamond	45
5.1	CVD diamond growth	47
5.2	Electrical properties of pCVD diamond	54
5.3	Signals from ionizing particles in a CVD diamond detector	61
6	CVD diamond measurements	67
6.1	Capacitance measurements	69
6.2	Current-voltage characteristics	71
6.3	Measurements of the Charge Collection Distance	80
6.4	Measurements of the Charge Collection Distance as a function of the absorbed dose.	85
6.5	Further studies	92

6.6	Linearity of diamond response	100
7	Summary	109
7.1	Simulation studies	110
7.2	pCVD diamond sensor tests	110
7.3	Conclusion	112
A	Fast Beam Diagnostics	113
B	Material analysis	115
B.1	Raman spectroscopy	115
B.2	Photo-induced luminescence	117
C	Correction for a geometry effect of the LED light intensity	118

Chapter 1

Introduction

The International Linear Collider (ILC) is an e^+e^- collider proposed for precise physics studies at the TeV-scale. The ILC would allow to explore the mechanism of the electroweak symmetry breaking, to probe physics beyond the Standard Model via precision measurements on basic physics processes and to make discoveries.

A precise luminosity measurement and an excellent hermeticity of the ILC detector are required for the physics program foreseen at the ILC and will be provided by the instrumentation of the Very Forward Region of the detector.

The design of the Very Forward Region of the ILC detector is considered in the presented work. Two electromagnetic calorimeters are located there. The Luminosity Calorimeter is purposed for the luminosity measurement based on the small-angle Bhabha scattering. The Beam Calorimeter will be positioned just adjacent to the beampipe covering the lowest possible polar angles. This calorimeter improves the hermeticity of the whole detector measuring high energy electrons, positrons and photons down to polar angle of about 6 mrad. Another purpose of the Beam Calorimeter is to serve for a fast beam diagnostics detecting e^+e^- pairs originating from the beamstrahlung photon conversion. In addition, the calorimeter shields the inner part of the detector from backscattered beamstrahlung remnants and synchrotron radiation.

The design of the Beam Calorimeter is the subject of this thesis. The calorimeter is exposed to e^+e^- pairs originating from beamstrahlung which cause a huge energy deposition for each bunch crossing. This deposition is used for the fast beam diagnostics, but forms a background for the detection of a single high energy electron or photon. Moreover, due to these harsh radiation condition the active material of the Beam Calorimeter must be radiation hard.

As a possible technology for the Beam Calorimeter, a diamond-tungsten sampling calorimeter is considered in this work. The performance for detection of a single high energy electron determined from full simulation of signal and background events. Detection efficiency, energy and angular resolution for electromagnetic showers in the Beam Calorimeter are studied. The results of the studies indicate requirements to the calorimeter segmentation, diamond sensor properties and read out electronics for the diamond-tungsten Beam Calorimeter.

The measurements of polycrystalline diamond sensors done to explore their performance for the detection of ionizing particles in a calorimeter are discussed in this work as well. The electrical properties, signal size and stability of the response under electromagnetic radiation are studied for diamond samples produced by different manufacturers. Results of beam test measurements done to examine a linearity of the diamond response over a large dynamic range are presented.

Chapter 2 briefly describes the physics goals at the ILC. The corresponding technical requirements on the ILC detector are discussed as well. The main accelerator and beam parameters and the detector design are reviewed. A detailed description of the Very Forward Region is done in Chapter 3. The tasks, requirements and possible designs of the Luminosity and Beam Calorimeters are discussed. The simulation studies of diamond-tungsten Beam Calorimeter are described in Chapter 4. The obtained detection efficiency, energy and angular resolution are presented. General properties of polycrystalline chemical vapour deposition diamonds (pCVD) are reviewed in Chapter 5. The growth process, electrical properties and signal formation in a diamond sensor are discussed there. The results of measurements done with different pCVD diamond samples are presented in Chapter 6. The Chapter 7 summarizes the results obtained from the simulation studies and the measurement results.

Chapter 2

Physics case of the ILC

Experimentally observed elementary particles and their interaction can be successfully described within the Standard Model (SM) [1, 2, 3]. The SM describes three of the four known forces as subjects of the electroweak theory and Quantum Chromodynamics (QCD) [4, 5, 6]. Gravity is not included in the SM. The interactions between elementary particles forming matter - fermions - are mediated by means of gauge field quanta - gluons in the strong interaction, W^\pm and Z-boson in the weak and the photon γ in the electromagnetic interactions. The gauge fields appear in the SM as a consequence of the local gauge invariance of the free particle Lagrangian. However, the local gauge invariance within the SM can be achieved only for massless fermions and gauge bosons. The experimentally observed existence of massive fermions and W^\pm and Z-bosons requires the gauge symmetry to be broken in the electroweak sector. The electroweak symmetry breaking is achieved spontaneously by the Higgs mechanism [7, 8, 9]. Masses of the particles are dynamically generated via interaction with a background scalar field. Within the SM the Higgs mechanism requires at least one weak isodoublet scalar field that results in the existence of a real scalar particle - the Higgs boson. Searches for the Higgs boson still remain one of the most crucial items in modern particle physics.

Since the SM Higgs boson contributes to the electroweak observables via radiative corrections, precision electroweak measurements are sensitive to the Higgs boson mass. The upper limit of the Higgs boson mass derived from LEP, SLC and Tevatron data is $M_H < 186 \text{ GeV}$ [10] at 95% confidence level. The direct searches for the Higgs boson performed at LEP give a lower limit on the Higgs boson mass of 114.4 GeV at 95% confidence level [11].

The SM predictions are in excellent agreement with results obtained at accelerator experiments. The same time, the SM can not provide the theoretical basement for the baryon asymmetry observed in the universe and can

not explain, for example, results of cosmic microwave background measurements [12]. The latter require the existence of so-called Cold Dark Matter in addition to the baryonic matter. The SM has no candidate for the Cold Dark Matter.

Moreover, the SM contains several theoretical imperfections. As extensions to the SM a variety of theories is developed to find a more general description of nature. The same time, the SM must remain a valid extrapolation of these theories to the low energy scale.

One of the promising extensions of the SM is Supersymmetry (SUSY) [13, 14, 15]. For every SM particle the Supersymmetry introduces a superpartner whose spin differs by $1/2$; all other quantum numbers as well as the masses of the superpartners are the same.

The experimentally excluded existence of superparticles at the explored energy range shows that SUSY must be a broken symmetry and supersymmetric particles are of larger mass than their ordinary partners.

One of the attractive features of SUSY is the possibility to explain cosmological observations. The assumption of the conservation of the so-called R-parity (a multiplicative quantum number equal to $+1$ for particles and -1 for their superpartners) results in the stability of the lightest supersymmetric particle (LSP). The LSP would have to be neutral and weakly interacting that makes it an excellent candidate for cosmological nonbarionic Cold Dark Matter [16]. Moreover, SUSY as a local gauge theory includes gravity.

In supersymmetric models the Higgs sector contains at least two scalar doublets, that results in 5 physical Higgs bosons.

Other models consider a new strong interaction to be responsible for the electroweak symmetry breaking. These models imply no Higgs bosons (technicolor) or consider the Higgs bosons as a heavy bound state. The main consequence of the strong electroweak symmetry breaking is the strong interaction among gauge bosons at the TeV scale.

These and many other topics of Particle Physics are subjects of intensive studies at future experiments. The Large Hadron Collider (LHC) will start operation in year 2007. With a center-of-mass energy of 14 TeV and a luminosity of $10^{34} \text{ cm}^{-2} \text{ s}^{-1}$ it will be a powerful machine for discoveries in the Higgs sector or physics beyond. However, the proton-proton collisions imply high QCD backgrounds. Furthermore, the composite structure of a proton leads the undefined initial state of interactions.

A TeV-scale e^+e^- linear collider has been proposed as a complementary facility. This machine would allow to explore the mechanism of the electroweak symmetry breaking. A rich particle world of supersymmetry might be detected with the facility as well. The clean experimental environment and known collision energy allows for precision measurements of many quan-

tities like cross sections, masses and asymmetries.

These precision measurements may be especially important if the new physics scale is not reached directly. In this case new physics can be probed at the loop level [17]. Precision measurements on fermion couplings to gauge bosons, triple and quartic gauge boson self-couplings will give hints on the physics beyond the SM. The desired precision of the measurements requires high and precisely measured luminosity [18].

The International Linear Collider (ILC) project joins European (TESLA¹), North American (NLC²), and Asian (GLC³) efforts on the linear collider design. In the past, two different machine technologies were under development. The NLC/GLC assumed warm rf cavities operating at 11.4 GHz [19, 20], while the TESLA design considered a superconducting rf linac operating at 1.3 GHz [18]. The final choice of the cold acceleration technology for the ILC was made in year 2004 [21].

The electron and positron bunches accelerated with the linacs are brought into collision in the interaction point (IP). The detector situated around the IP records the e^+e^- annihilation events.

The design of the Very Forward Region of the detector is considered in the presented work. One of two electromagnetic calorimeters situated there - the BeamCal - is the subject of this thesis. Simulation studies of the BeamCal based on the TESLA TDR⁴ beam parameters and detector design [18] are done to explore the feasibility of a diamond-tungsten sandwich calorimeter. Studies of polycrystalline diamond as a sensor material for the BeamCal are done to explore the properties of the material.

2.1 The ILC parameters

The International Linear Collider is planned to operate at center-of-mass energies, \sqrt{s} , ranging between 90 GeV and 1 TeV. This allows both direct measurements of possible new phenomena at high energies as well as highly precise electroweak measurements at the Z-pole (so-called GigaZ program).

Both the electron and positron beams are foreseen to be polarized. This is essential for many studies within and beyond the SM. In spite being challenging, the positron polarization is especially desired for supersymmetry studies and for precise electroweak measurements [22].

¹Tera Electron Volt Energy Superconducting Linear Accelerator

²Next Linear Collider

³Global Linear Collider

⁴Technical Design Report

Other possible options for colliding beams considered for the ILC are e^-e^- , $\gamma\gamma$ and $e^-\gamma$ scattering. For the latter two options an additional laser system and a second interaction region are necessary [23].

In the TESLA design the e^+e^- mode assumed opposite momenta of electron and positron beams, usually denoted as "head-on collisions" or "zero crossing angle". The ILC design currently considers the possibilities for 2 and 20 mrad crossing angles [23].

At the time of writing this thesis the final ILC design and beam parameters are still under discussion. However, due to the choice of the cold acceleration technology the currently discussed ILC beam parameters are similar to the ones of the TESLA machine.

The main accelerator and beam parameters for the $\sqrt{s} = 500 \text{ GeV } e^+e^-$ TESLA design are shown in Table 2.1.

\sqrt{s}	0.5 TeV
gradient	23.4 MeV/m
repetition rate	5 Hz
beam pulse length	950 μs
No. of bunches per pulse	2820
per pulse bunch spacing	337 ns
charge per bunch	$2 \cdot 10^{10}$
beam size, σ_x	553 nm
beam size, σ_y	5 nm
bunch length, σ_z	0.3 mm
luminosity	$3.4 \cdot 10^{34} \text{ cm}^{-2}\text{s}^{-1}$
e^- polarization	80%
e^+ polarization	45 – 60%

Table 2.1: The main TESLA TDR beam parameters for the $\sqrt{s} = 500 \text{ GeV } e^+e^-$ baseline design [18].

2.2 The requirements on the ILC detector

The physics program at the Linear Collider establishes strong requirements on the performance of the ILC detector. This can be illustrated with the following examples.

- The Higgs-strahlung $e^+e^- \rightarrow ZH$ and WW-fusion $e^+e^- \rightarrow \nu_e\bar{\nu}_eH$ are the main SM Higgs boson production mechanisms at the linear collider. The mass and couplings measurements of the Higgs boson can be performed with high precision.

For example, the process $e^+e^- \rightarrow HZ \rightarrow Hl^+l^-$ allows the Higgs boson cross section and mass to be measured independently of the Higgs decay mode via the recoil mass of the di-lepton system [24]. In order to ensure a sharp Higgs boson signal, the track transverse momentum resolution must be $\delta p_t/p_t^2 \approx 5 \cdot 10^{-5} \text{ GeV}^{-1}$ [25]. This is more than one order of magnitude better than the one realized at the LEP experiments.

- The SM predicts Higgs couplings to fermions and bosons to be proportional to their masses. Thus the Higgs couplings derived from branching fraction measurements allow to test this fundamental feature of the electroweak symmetry breaking mechanism [26].

The branching fraction measurements from $HZ \rightarrow q\bar{q}l^+l^-$ and $HZ \rightarrow q\bar{q}q'\bar{q}'$ decays require a good separation of the $b\bar{b}$, $c\bar{c}$ and $\tau\bar{\tau}$ pairs. The lifetime of B and D mesons results in a few mm distance between the IP and the decay vertex. Thus b and c identification (so-called b- and c-tagging) requires an excellent detection of the secondary vertices. The performance of the vertex detector expressed in the resolution of the impact parameter projections to the $(r\phi)$ and (rz) planes is required to be

$$\sigma_{r\phi} = \sigma_{rz} = \frac{3.8 \oplus 7.8}{p \sin^{3/2} \theta} \mu\text{m} ,$$

where p is the momentum in GeV and θ is the polar angle [27]. The required resolution is about 10 times better than at LEP detectors.

- A lot of physics processes are expected to produce hadrons in intermediate states. The final multiparton states must be resolved and measured with good resolution. For example, the $t\bar{t}$ -production, $e^+e^- \rightarrow t\bar{t}$, is followed by the top decay to Wb . Thus the process will result in a six-jet final state.

The excellent jet resolution is needed also for the studies of strong electroweak symmetry breaking. In this case gauge bosons become strongly interacting and the channel $e^+e^- \rightarrow WW\nu\nu$ can be used to probe this effect. The process is characterized by a four-jets final state and missing energy and momentum.

The analysis of the processes mentioned above requires an excellent jet energy and angular resolution. To reach this, tracks and correspond-

ing clusters in the calorimeters are separated from the clusters with no corresponding tracks - the neutral clusters. The jet energy and direction are obtained by adding up the momenta of the tracks and neutral clusters. This procedure is referred to as energy flow technique and prefers the tracking system and both the calorimeters (electromagnetic and hadronic) to be located inside the coil to minimize the amount of inactive material in front of the calorimeters [18].

- The precision measurements require a luminosity accuracy at the level $\delta L/L \leq 10^{-3}$ [28]. The precision measurements at low energies within the GigaZ program need even better accuracy: $\delta L/L \sim 2 \cdot 10^{-4}$ [28]. The luminosity measurement will be performed using the small-angle Bhabha scattering, $e^+e^- \rightarrow e^+e^-(\gamma)$. Since the process has a large cross section which can be precisely calculated [29], the luminosity can be determined from the Bhabha event rate with a very high accuracy.
- A good detection capability of the forward region is crucial for new particle searches. As an example the SUSY stau production can be considered. Staus, $\tilde{\tau}$, are produced pairwise in the process $e^+e^- \rightarrow \tilde{\tau}^+\tilde{\tau}^-$. For a SUSY scenario where the lightest SUSY particle (LSP) is the lightest neutralino, the $\tilde{\tau}$ decays into a τ -lepton and a neutralino χ^0 . The stau mass can be measured via a mass threshold scan; however, this requires a clean detection of this channel. The cross section of the stau production is about 10 fb near the threshold. The background in this region is dominated by two-photon processes with cross sections at the nb level [16]. Thus the measurements of the stau mass require an efficient background suppression.

Fig. 2.1 shows diagrams of the stau production (a) and the main two-photon background process $e^+e^- \rightarrow \tau^+\tau^-e^+e^-$ (b). Both processes have a very similar event signature. The slepton production is characterized by a missing energy carried away by neutralinos and by a low energy of the visible particles from τ -decay. In the two-photon events the beam electrons carry away most of the energy and scatter at a very low angle. If they are not detected, the topology of the low energetic remnants is very similar to one of the SUSY event. However, a veto on the high energetic electrons at very low angles allows to reduce the background down to an acceptable level [16].

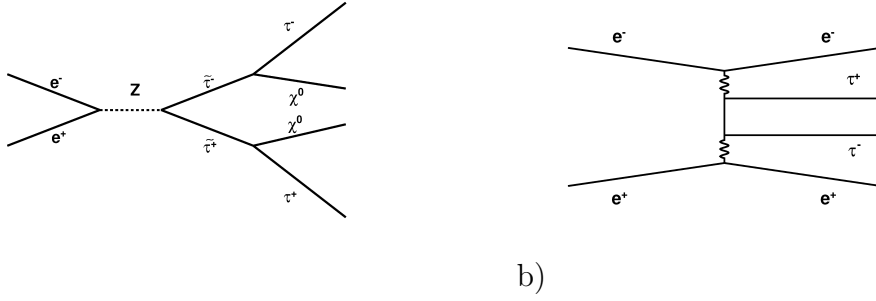


Figure 2.1: The diagrams of the stau production (left) and the two-photon process (right).

2.3 The ILC detector

Three different concepts of the ILC detector are under consideration. The Global Large Detector (GLD) [30], the Large Detector (LDC) [31] and the Silicon Detector SiD [32] differ mostly in the size, the tracker technologies and the magnetic field strength and have a very similar performance. The LDC is based on the TESLA detector design.

Fig. 2.2 shows a schematic view of the TESLA detector [18]. The detector consists of the tracking system surrounded by the electromagnetic and hadron calorimeters, the magnet coil, the muon system, which also serves as a return yoke for the magnetic flux, and two calorimeters in the Very Forward Regions. The whole tracking system and the calorimeters are immersed in a solenoidal magnetic field of 4 T [18].

2.3.1 Tracking System

The Vertex Detector (VTX), Silicon Intermediate Tracker (SIT), Forward Tracking Disks (FTD), Time Projection Chamber (TPC) and Forward Chambers (FCH) belong to the tracking system of the detector.

The required performance of the Vertex Detector can be reached with 5 layers of silicon pixel sensors with a pitch of about $20 \mu\text{m}$. The required radiation hardness is about 100 krad per 5 years [18]. Several technologies, like CCD (Charge Coupled Device), DEPFET (Depleted Field Effect Transistor) and MAPS (Monolithic Active Pixel Sensor) are tested for the Vertex Detector [27].

The Central Tracking System provides the information on spatial coordinates of a particle and on its energy loss along the track. The performance

goal of the central tracker is $\delta p_t/p_t^2 \approx 5 \cdot 10^{-5} \text{ GeV}^{-1}$ [18]. In the TESLA detector design, the central tracker consist of the TPC and the FCH located between the TPC and the calorimeter endcap. The goal of the TPC point resolution is $100 \mu\text{m}$ in the $(r\phi)$ -plane and $500 \mu\text{m}$ in the z -coordinates. The required double track resolution is 2 and 5 mm in $(r\phi)$ and z coordinates, respectively. As a possible working gas the 93%Ar + 2%CO₂ + 5%CH₄ mixture is considered. Electrons produced via ionization along the track of a charged particle drift under the electric field to the endplates. There gas amplification is needed to provide a detectable signal. To obtain an optimal amplification and to provide excellent spatial resolution gas avalanche micro detectors - GEM (Gas Electron Multipliers) and Micromegas - are considered for the TPC read out. Both options have been tested with similar success [27].

The performance of the Central Tracking System operated with the barrel part only would deteriorate already at the polar angles below $\theta \sim 20^\circ$ due to reduction of the track length inside the TPC. The FCH is purposed to improve the momentum resolution at lower polar angles. The FCH design is based on the ATLAS Transition Radiation Tracker technology [33].

The Intermediate Tracking System is purposed to improve the track momentum resolution providing additional space points and to link tracks found in the TPC with the corresponding tracks in the VTX. It consists of the SIT and FTD detectors. The SIT is positioned around the VTX and consists of two cylinder of double-sided silicon detectors providing the spatial resolution of $10 \mu\text{m}$ in the $(r\phi)$ and $50 \mu\text{m}$ in the (rz) planes [18]. Seven silicon discs of the FTD are located in the forward region to improve the momentum resolution at low polar angles. The presence of the FTD and the FCH are especially important for polar angles $\theta < 12^\circ$ where particles do not cross any vertex detector layer [18]. The FTD combines pixel and strip detectors.

2.3.2 Calorimetry

The tracking system is surrounded by the electromagnetic (ECAL) and hadronic (HCAL) calorimeters. The energy flow concept, mentioned in Section 2.2, requires a fine granularity of the calorimeters to match tracks in the tracker to corresponding clusters in calorimeters.

As a possible technology of the ECAL a fine segmented silicon-tungsten sampling calorimeter is considered. The longitudinal segmentation of the calorimeter provides 40 layers of tungsten absorber alternating with silicon sensors. Transversely the calorimeter is segmented into readout cells of $1 \times 1 \text{ cm}^2$ size, which corresponds to about one Moliere radius [18].

As an alternative solution a silicon-scintillator lead sandwich calorimeter is proposed. The latter is also a highly segmented calorimeter with longi-

tudinal sampling, where silicon and scintillator planes are used as sensitive layers. The energy resolution⁵ $\sigma_E/E \approx 11\%/\sqrt{E}$ has been reached with a prototype of the silicon-scintillator lead calorimeter [27].

Two technologies are proposed for the HCAL. The analog readout HCAL is a tile sampling calorimeter with stainless steel as an absorber and scintillator tiles as sensors. For the readout silicon photomultipliers (SiPM) are used. The digital option of the HCAL uses GEMs or RPCs (Resistive Plate Chamber) as active elements. The energy resolution for single hadrons is estimated to be in the range of $(35 - 40)\%/\sqrt{E}$ depending on the HCAL technology [18].

The necessary jet energy resolution can be reached with the mentioned energy flow concept [27]. The concept uses the calorimeter only for neutral particles, while for the charged ones the track momentum measured by the Central Tracker (TPC) is used. This provides the jet energy resolution $\sigma_{E_{jet}}/E_{jet} \approx 30\%/\sqrt{E_{jet}}$ [34].

⁵Here and further the energy in the parameterization of the energy resolution is expressed in units of GeV.

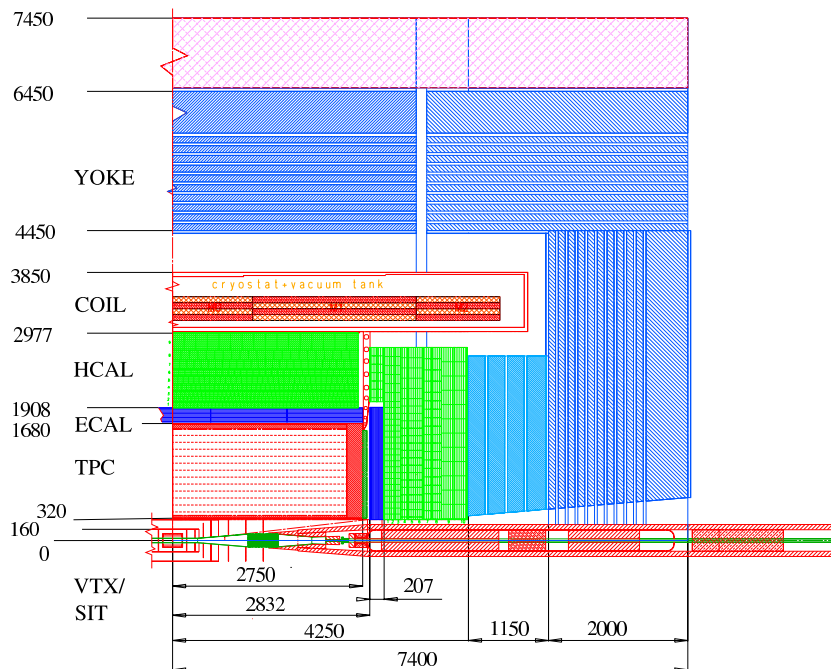


Figure 2.2: A schematic view of the TESLA detector TDR design [18]. The tracking system of the detector contains the Vertex Detector (VTX), the Silicon Intermediate Tracker (SIT) and the Time Projection Chamber (TPC). The Forward Tracking Disks (FTD) are located in the forward region covering polar angle between $\sim 7^\circ$ and $\sim 25^\circ$. The Forward Chambers (FCH) are located between the TPC endplate and the electromagnetic calorimeter endcap. The trackers and the calorimeters are located inside a magnet providing a 4 T solenoidal magnetic field.

Chapter 3

Very Forward Region

Two electromagnetic calorimeters are planned in the Very Forward Region (VFR) of the ILC detector.

The Beam Calorimeter (BeamCal) will be positioned just adjacent to the beampipe in front of the final focus quadrupoles covering the lowest possible polar angles. The calorimeter improves the hermeticity of the whole detector measuring high energy electrons down to very low angles. As mentioned in Section 2.2, the measurements at very low angles are especially crucial for SUSY studies. Another purpose of the BeamCal is to serve for a fast beam diagnostics detecting e^+e^- pairs originating from the beamstrahlung photon conversion. The capability of the fast beam diagnostics is discussed in Appendix A. In addition, the calorimeter shields the inner part of the detector from backscattered beamstrahlung remnants and synchrotron radiation.

The Luminosity Calorimeter (LumiCal) is purposed for the luminosity measurement based on the small-angle Bhabha scattering. The cross section of Bhabha scattering is large at small polar angles giving an appropriate event rate to obtain a statistical error better than 10^{-3} . However, the LumiCal must be placed at angles large enough to avoid the background from beamstrahlung pairs.

The calorimeters are located just before the final quadrupole magnets of the beam delivery system. The position of the final quadrupole magnets is defined by the focal length of the final focus system L^* .

Fig. 3.1 shows the TESLA TDR design with $L^* = 3$ m [18]. In this design the LumiCal covers polar angle between 27.5 and 83.1 mrad and sits before the ECAL end-caps. The BeamCal covers 5.5 to 27.5 mrad at a distance of 220 cm from the interaction point (IP).

The detector design for the small focal length $L^* = 3$ m limits the performance of the luminosity calorimeter [35]. The structure of the LumiCal is not sufficiently compact. Large leakage of the shower from high energy

electrons leads to a poor angular resolution and makes the control of the systematics impossible. In addition, it may cause fake events in the ECAL end-caps. Moreover, the small focal length design limits the space for readout electronics of the calorimeters.

Fig. 3.2 shows a layout of the VFR for the currently considered design with a focal length of 4.05 m. The LumiCal is located behind the ECAL at polar angles from 26 to 92 mrad. The calorimeter has a compact geometry and hence a small shower leakage.

3.1 Luminosity Calorimeter

3.1.1 Luminosity measurement

As mentioned in Chapter 2, the precision measurements within the GigaZ program need the luminosity measurement to be performed with the accuracy of $\delta L/L \sim 2 \cdot 10^{-4}$ [28]. At LEP the best result for the luminosity measurement accuracy was reached at the OPAL experiment where the systematic measurement uncertainty of $3.4 \cdot 10^{-4}$ has been achieved [36].

Fig. 3.3 shows the Feynman diagrams of the Bhabha scattering. The process is well suited for the luminosity measurement due to the high cross section at small polar angles and the accurate theoretical calculations [29]. At the OPAL experiment the theoretical errors contributed with $5.4 \cdot 10^{-4}$ to the luminosity uncertainty exceeding the achieved systematics [36].

The differential cross section at the Born level can be expressed as

$$\frac{d\sigma}{d\Omega} = \frac{\alpha^2}{2s} \left[\frac{1 + \cos^4 \theta/2}{\sin^4 \theta/2} - 2 \frac{\cos^4 \theta/2}{\sin^2 \theta/2} + \frac{1 + \cos^2 \theta}{2} \right],$$

where θ is the polar angle and \sqrt{s} is the center-of-mass energy.

At small polar angles the cross section is dominated by the t -channel photon exchange that corresponds to the first term in the expression above and results in strong angular dependence:

$$\frac{d\sigma}{d\theta} \propto \frac{1}{\theta^3}.$$

The rate of the Bhabha events, dN/dt , is proportional to the luminosity:

$$\frac{dN}{dt} = L \int_{\theta_{min}}^{\theta_{max}} \frac{d\sigma}{d\theta} d\theta,$$

where θ_{min} and θ_{max} are defined by the acceptance radii of the LumiCal. For 500 GeV center-of-mass energy and the luminosity of $3.4 \cdot 10^{34} \text{ cm}^{-2}\text{s}^{-1}$ this

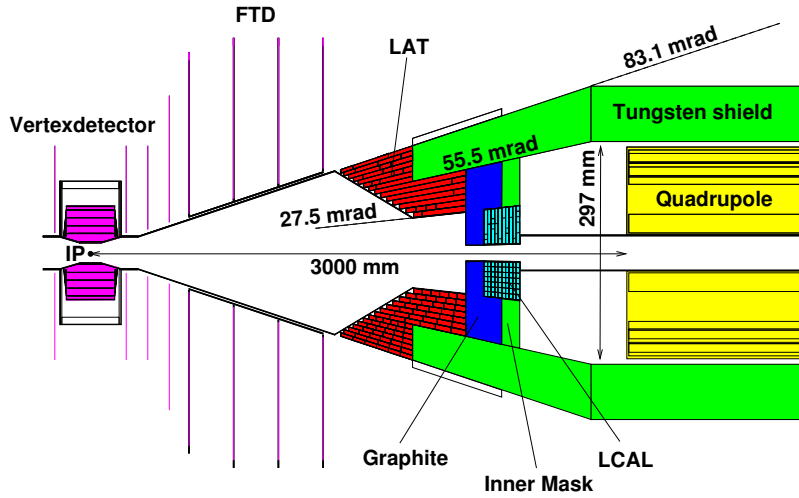


Figure 3.1: The Very Forward Region of the TESLA detector with $L^* = 3$ m. The vertical scale of the plot is stretched to show the detectors in the VFR. The LAT represents the LumiCal and LCAL corresponds to the BeamCal. The final quadrupoles are surrounded by a tungsten shield. The tungsten mask together with the graphite ring protects the inner layers of the Vertex Detector and the TPC against particles backscattered from the quadrupoles.

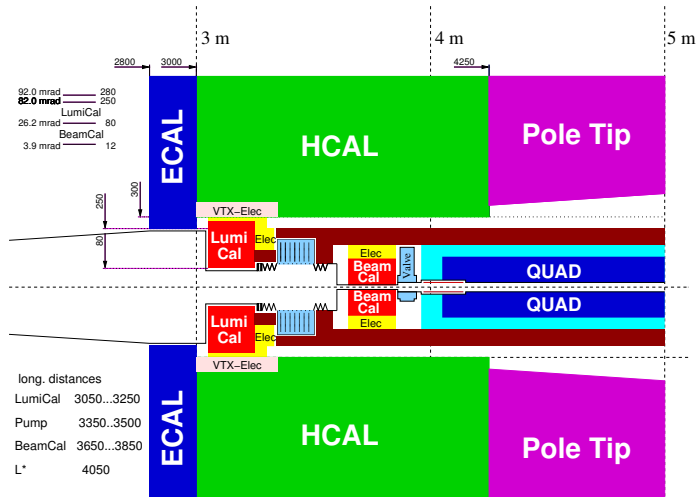


Figure 3.2: The Very Forward Region for $L^* = 4.05$ m. The conical beampipe on the left points to the IP. The distance between the IP and the LumiCal is 3050 mm and between the IP and the BeamCal 3650 mm. QUAD is the final quadrupole of the beam delivery system.

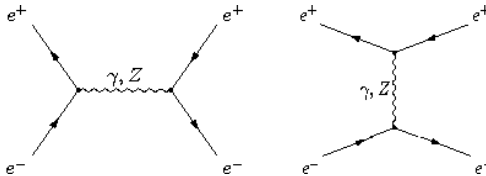


Figure 3.3: The Feynman diagrams of the Bhabha scattering.

gives about 10^9 events per year for the calorimeter acceptance $\theta_{min} = 30$ mrad and $\theta_{max} = 75$ mrad [37]. Thus the statistical error will be better than 10^{-4} for one year of accelerator running.

The systematic measurement uncertainty is defined by the accuracy of polar angle and energy measurements and by the precision of the cross section calculation. Due to the strong angular dependence of the cross section, assuming absolutely precise cross section calculations, the luminosity measurement accuracy will be dominated by a systematic error of the angular measurements $(\Delta\theta)_{sys}$ [38]:

$$\frac{\delta L}{L} \sim 2 \frac{(\Delta\theta)_{sys}}{\theta}.$$

3.1.2 LumiCal

The baseline design of the LumiCal is a silicon-tungsten sampling calorimeter consisting of 30 layers. The thickness of the tungsten in each layer is about one radiation length (3.4 mm) and the gap for silicon sensors is a few mm. Pad and strip designs of the silicon sensors are under consideration [35].

In the pad option a silicon sensor plane of 0.5 mm thickness is subdivided radially into rings and azimuthally into sectors, forming readout pads. Each sensor plane is subdivided into 15 rings and 24 sectors. The gap for the sensors plane is assumed to be 4 mm.

In the strip version, the sensor planes alternate between sensors with 64 concentric strips and sensors with 120 radial sectors. Sensors of 0.5 mm thickness are glued on a ceramic carrier of 1.5 mm thickness. For bonds and signal readout 1 mm additional space is left between the tungsten disks.

The simulation studies of strip and pad designs have shown both of them to be feasible [35, 39]. Bhabha events were generated with the BHLUMI [40] and BHWIDE [41] packages. The initial and final state radiation was taken into account. A distortion of beam energy spectrum due to beam-beam interactions was included in the studies using the CIRCE program [42] along with a Gaussian beam spread of $0.05\%\sqrt{s}$. The full detector simulation

was done for both designs [35]. The studies have demonstrated that such a compact calorimeter would allow to control the systematic uncertainty of the luminosity measurement better than $\mathcal{O}(10^{-4})$ [39].

The luminosity measurement requires a precise alignment of the two LumiCal detectors to each other and precise positioning with respect to the beam axis and the IP. This requires a stable mechanical design and position monitoring. Due to the strong dependence of the Bhabha cross section on the polar angle, the diameter of the inner radius of the calorimeter acceptance has the most crucial impact on the luminosity measurement accuracy. The required precision for the inner radius is estimated to be $4\ \mu\text{m}$ [38].

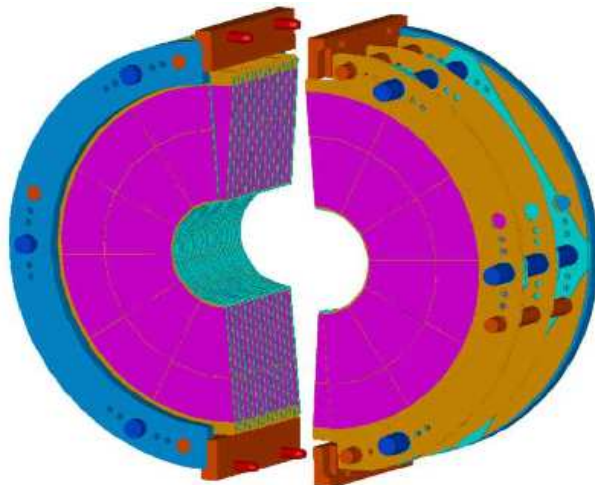


Figure 3.4: A mechanical design of the LumiCal. The segmented silicon sensors are interspersed into the tungsten disks. The calorimeter consists of two half barrels to allow for mounting on a closed beam pipe [35].

A possible mechanical design is shown in Fig. 3.4. The calorimeter consists of two half barrels to allow for mounting on a closed beam pipe. The mechanical supports of the absorber disks and sensor planes are done separately. The accuracy requirements for the absorber support frame are moderate, however the support for the sensor planes must ensure the requirement on the inner radius accuracy.

3.2 Beam Calorimeter

3.2.1 Beamstrahlung and pair production

Due to the small size and high electric charge of a bunch in the linear collider electromagnetic forces squeeze crossing bunches and cause photon emission. The photon emission is referred to as beamstrahlung.

Beamstrahlung can be characterized by the critical frequency ω_c

$$\omega_c = \frac{3\gamma^3 c}{2\rho},$$

where ρ the bending radius of the beam particles trajectory and γ is the relativistic factor

$$\gamma = \frac{E_{beam}}{m_e}.$$

Often a parameter Υ , which is a ratio of the critical photon energy, $\hbar\omega_c$, to the beam energy E_{beam} , is used instead. Υ is not constant during the bunch crossing and in the case of a gaussian beam with r.m.s. radii σ_x and σ_y the average value can be estimated as [43]

$$\Upsilon \equiv \frac{2}{3} \frac{\hbar\omega_c}{E_{beam}} \approx \frac{5}{6} \frac{Nr_e^2\gamma}{\alpha\sigma_z(\sigma_x + \sigma_y)},$$

where N is the number of electrons in a bunch, σ_z is the bunch length, α is the fine structure constant, r_e is the classical electron radius.

The average number of beamstrahlung photons per incoming beam particle can be calculated as [44]

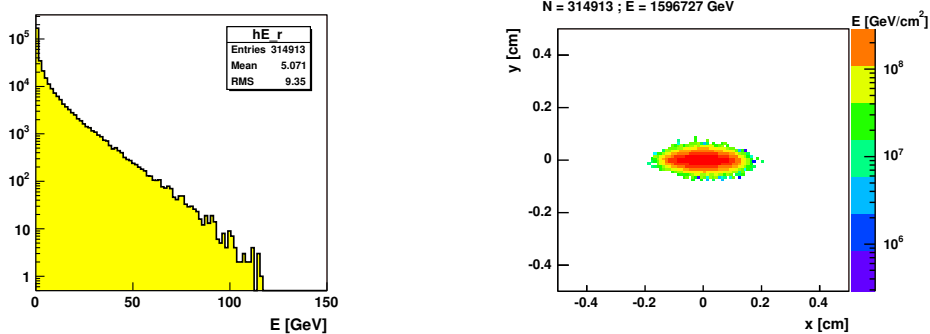
$$N_\gamma \approx 2.12 \frac{\alpha Nr_e}{\sigma_x + \sigma_y} \frac{1}{\sqrt{1 + \Upsilon^{2/3}}}.$$

The average energy loss per incoming particle is

$$\delta_B \approx \frac{r_e^3 N^2 \gamma}{\sigma_z (\sigma_x + \sigma_y)^2} \frac{1}{(1 + 1.5\Upsilon^{2/3})^2}.$$

For the nominal TESLA parameters with $\sqrt{s} = 500$ GeV the Υ parameter is 0.06, $N_\gamma = 1.6$ and the average fractional beam energy loss due to beamstrahlung $\delta_B = 3.2\%$.

The energy distribution of the beamstrahlung photons is shown in Fig. 3.5 (a). The beamstrahlung photons have a very narrow angular distribution as can be seen from Fig. 3.5 (b) and will be emitted downstream from the IP through the beampipe. Although they do not form a background in the



a)

b)

Figure 3.5: Beamstrahlung photons generated in one bunch crossing. The energy spectrum (a) and the energy distribution in the (xy) -plane orthogonal to the beam axis at a distance $z = 365$ cm from the IP (b). This distance corresponds to the BeamCal position in the $L^* = 4.05$ m detector design. The photons are generated with the Monte Carlo program Guinea Pig [45]. The plots show only a fraction of 10^{-5} of the produced photons.

detector by themselves, they create a large number of e^+e^- pairs deflected to larger angles.

There are two possibilities of e^+e^- pair production from beamstrahlung photons. The coherent pair production is caused by the interaction with the collective electromagnetic field of the bunch. However, this process is exponentially suppressed for small Υ and plays a role only starting with $\Upsilon > 0.3$ [43].

The incoherent pair production, through the scattering on individual particles of a bunch, dominates for small Υ . The processes involved are¹

- real photon scattering, $\gamma\gamma \rightarrow e^+e^-$ (Breit-Wheeler process),
- virtual photon scattering, $ee \rightarrow ee e^+e^-$ (Landau-Lifshitz process),
- and their combination, $e\gamma \rightarrow ee^+e^-$ (Bethe-Heitler process).

The corresponding diagrams are shown in Fig. 3.6.

Fig. 3.7 shows the energy distribution of the created electrons and positrons in a plane perpendicular to the beam direction in the absence of a magnetic field. The plane is chosen at the distance $z = 365$ cm from the IP, which corresponds to the BeamCal position in the $L^* = 4.05$ m detector design. The pairs are generated with the Guinea Pig Monte Carlo program [45] for the

¹The Bhabha scattering is not discussed here since it contributes with less than one event in the BeamCal per bunch crossing.

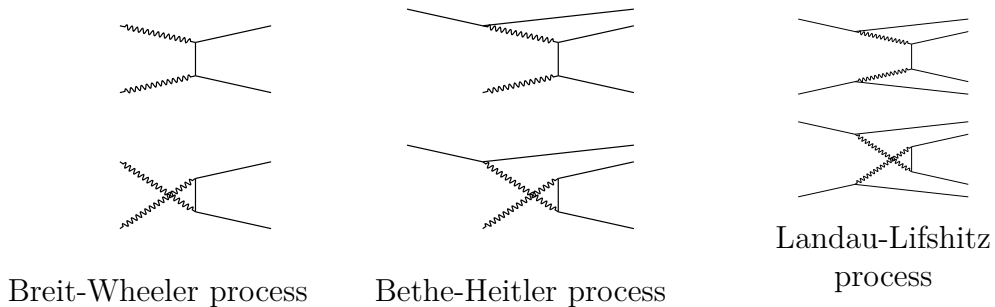


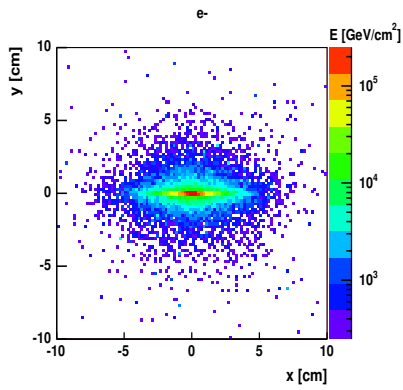
Figure 3.6: The incoherent pair production processes.

nominal TESLA beam parameters for one bunch crossing. The electron beam is assumed to be directed along the z axis of the right-handed coordinate system. If electrons produced from beamstrahlung are directed to the positive z direction, they are focused in the field of the positron bunch (Fig. 3.7 (a)). Correspondingly, positrons emitted in this direction are defocused, as it seen in Fig. 3.7 (b). The resulting energy density distribution, summing up both electrons and positrons, and the energy spectrum are shown in Fig. 3.7 (c) and (d), respectively.

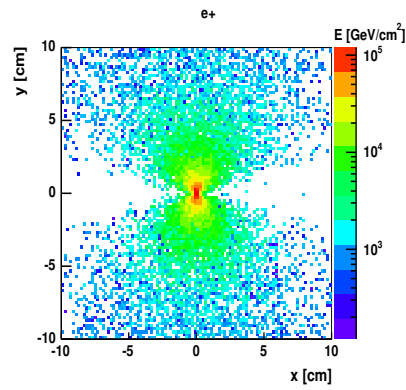
About $1.3 \cdot 10^5$ electrons and positrons per a bunch crossing are emitted in both directions with a total energy of about $3.6 \cdot 10^5$ GeV. The pairs are also collimated in the beam directions, however, the angular distribution is much wider than the one of the beamstrahlung photons.

In the solenoidal detector magnetic field of 4 T the particles move on helical trajectories with a radius depending on their transversal momentum. This distorts the spatial energy density distribution as shown in Fig. 3.8. Here the magnetic field is directed along the z axis. The focused electrons (a) are influenced less than the spread positrons (b). The total energy density distribution is shown in Fig. 3.8 (c), Fig. 3.8 (d) shows the energy density distribution with a cut assuming a 12 mm radius hole which corresponds to the beampipe. The energy deposition outside the beampipe is about 35 TeV per side per bunch crossing. At a distance of 220 cm from the IP, that corresponds to the BeamCal position in the TDR design ($L^* = 3$ m), the energy deposition outside the beampipe is about 22 TeV.

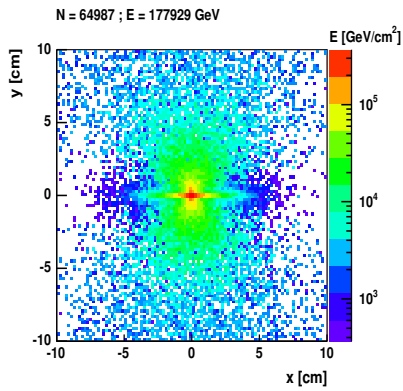
Fig. 3.9 shows the energy density on the BeamCal face plane in the case of a 20 mrad beam crossing angle [46] for $L^* = 4.05$ m. The energy deposition outside the beampipe is 66 TeV.



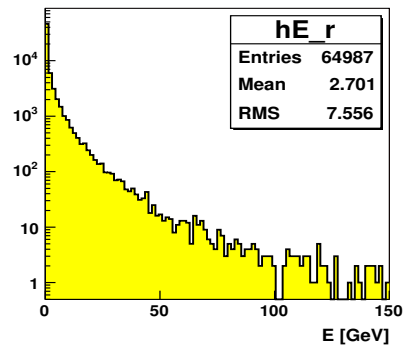
a)



b)

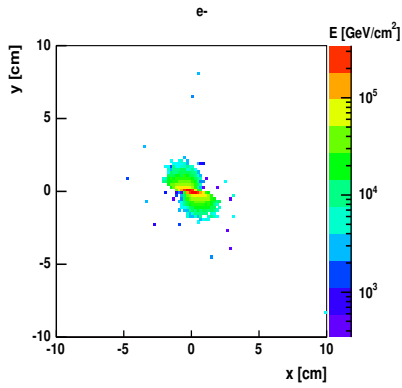


c)

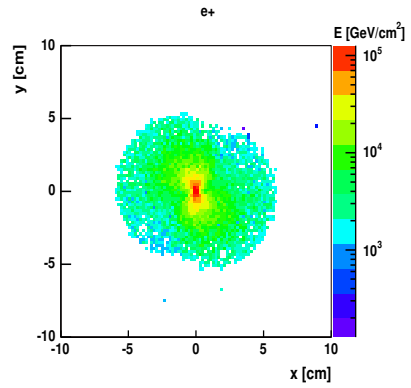


d)

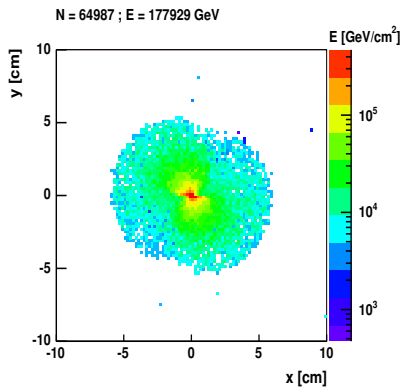
Figure 3.7: The energy density distributions of electrons (a) and positrons (b) produced via the incoherent pair production in the (xy) -plane at $z = 365$ cm. The electron beam is assumed to be directed along the z axis. The total energy density distribution and energy distribution are shown in plots (c) and (d) respectively.



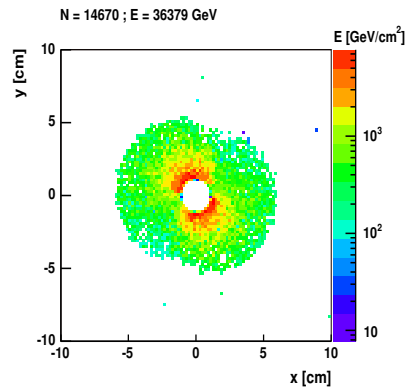
a)



b)



c)



d)

Figure 3.8: The electron (a) and positron (b) energy density distributions in the (xy) -plane at $z = 365$ cm in the case of a 4 T magnetic field. The total energy density distribution without (c) and with (d) the beampipe cut.

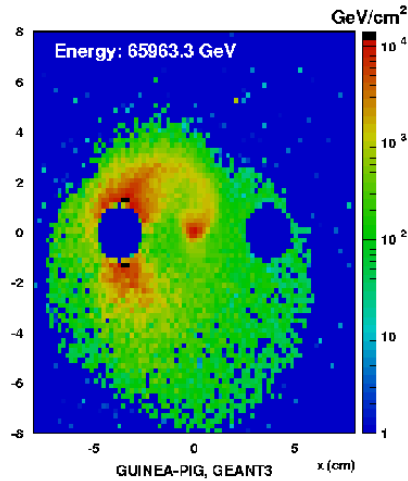


Figure 3.9: The pairs energy density distribution in the BeamCal in the case of a 20 mrad beam crossing angle and $L^* = 4.05$ m detector design (after Reference [46]).

3.2.2 Requirements on the BeamCal and possible technologies

As mentioned above, the beamstrahlung remnants create a huge energy deposition in the BeamCal. The deposited energy depends on the beam parameters and detector design and amounts to about ~ 20 TeV per bunch crossing for the TESLA TDR design. This results in an integrated radiation dose of up to 10 MGy/year for some areas of the calorimeter [35]. For higher center-of-mass energies, for larger distance between the BeamCal and the IP and for a beam crossing angle the energy deposition and the corresponding integrated dose are even higher. This requires radiation hard sensors for the BeamCal.

As shown in Section 3.2.1, the energy density of pairs originating from beamstrahlung varies strongly with azimuthal and polar angles. Moreover, it is sensitive to beam parameters. Thus the distribution of energy deposited in the BeamCal will vary with a deviation of the beam parameters. To perform the fast beam diagnostics based on the BeamCal measurements (Appendix A), a linear calorimeter response over a large dynamic range is needed.

Measurements of high energy electrons or photons on top of the beamstrahlung background require a small transverse size of the shower developing in the calorimeter. This makes the detection of particles more efficient. The

transverse shower size is characterized by the Moliere radius

$$R_M = X_0 \frac{E_s}{E_c},$$

where X_0 is the radiation length, $E_s = m_e c^2 \sqrt{4\pi/\alpha} = 21.2 \text{ MeV}$ and E_c is the critical energy. More than 90% of the shower is contained within a distance of about $2 R_M$ from the longitudinal shower axis.

One of the technology options of the BeamCal is a sandwich calorimeter. Tungsten can be used as the absorber material since it has a small radiation length ($X_0 = 6.76 \text{ g/cm}^2$ or 0.35 cm) and a small Moliere radius ($R_M \approx 0.9 \text{ cm}$). As a radiation hard sensor material CVD (Chemical Vapour Deposition) polycrystalline diamond was proposed [18]. Stability of a CVD diamond response was shown up to the dose of 10 MGy [47]. The irradiation tests were carried out with synchrotron radiation providing 10 keV photons and with a ^{60}Co source, which emits photons and β -electrons in the MeV energy range. The possibility to use silicon as a sensor material of the BeamCal is also considered; however, no information about its radiation resistance to electromagnetic irradiation at such high doses is available.

Fig. 3.10 shows an artistic view of a half-barrel of the sandwich calorimeter. Silicon or diamond sensors (red) are interspersed with tungsten disks (blue). The thickness of a tungsten layer is chosen to be one radiation length. The gaps between the disk are 0.5 mm .

Another option considered for the BeamCal design is a heavy-element crystal calorimeter where scintillator segments are read out with optical fibers. Fig. 3.11 (a) shows the segmented crystal calorimeter. A detailed view of a longitudinal segment with fibers attached is shown in Fig. 3.11 (b). Every piece of the segment is optically isolated from the neighboring ones. A fiber coupled to a segment is routed to the back of the calorimeter through grooves in the adjacent rear pieces. The fibers are optically isolated in these areas to prevent light sharing between different segments of the calorimeter. As a possible material for the calorimeter lead tungstenate (PbWO_4) is considered.

Simulation studies done for the lead tungstenate calorimeter have shown this design to be feasible for the BeamCal [48]. The measurements of light yield reduction due to the fiber read out as well as the measurements of crosstalk between the scintillator segments and the fibers have shown the read out technology to be practicable [49].

Table 3.1 shows the radiation length and Moliere radius of the lead tungstenate crystal and the diamond-tungsten options. Due the dominating weight of the absorber and the low fraction of the sensor material in the

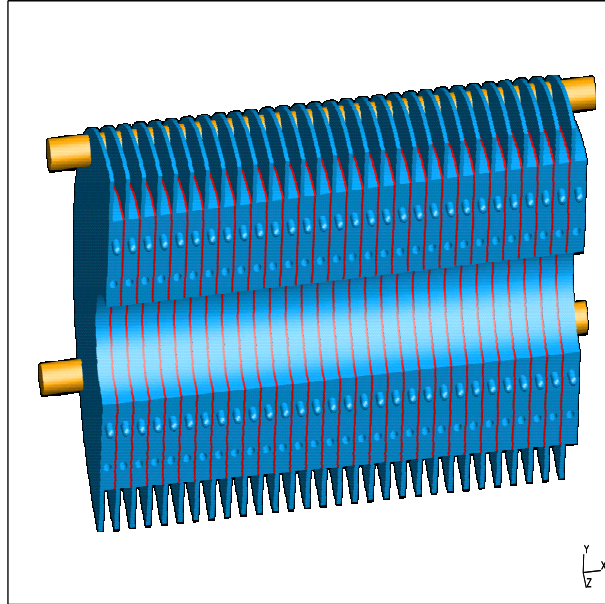
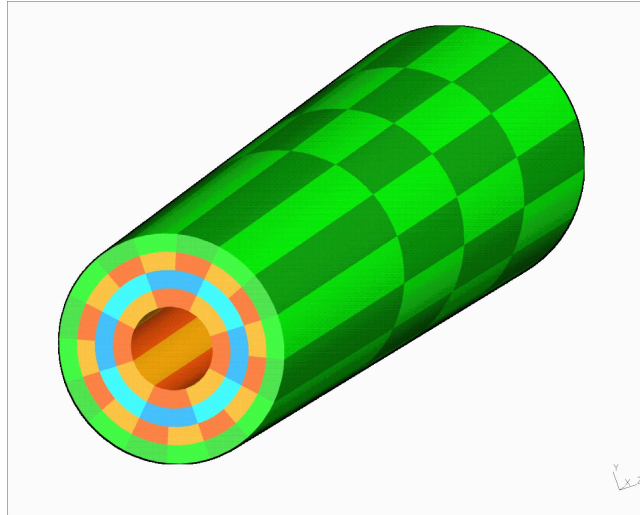


Figure 3.10: An artistic view of a half-barrel of the sandwich calorimeter. Silicon or diamond sensors (red) are interspersed with tungsten disks (blue). The mechanical support is shown in yellow.

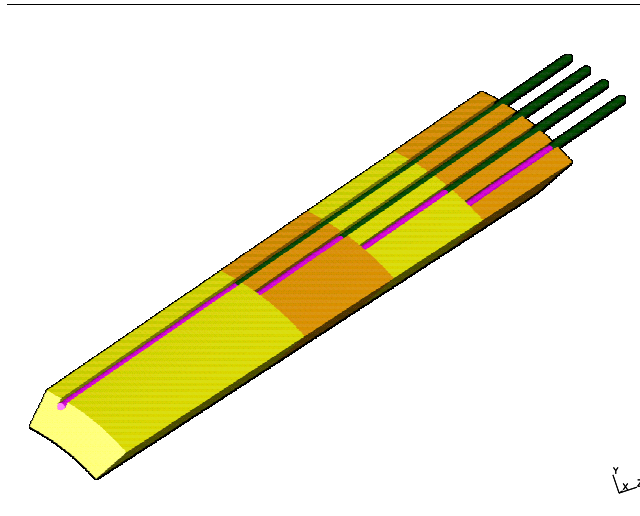
diamond-tungsten calorimeter the radiation length and Moliere radius of the calorimeter are dominated by tungsten.

	ρ , g/cm ³	X_0 , cm	R_M , cm
PbWO ₄	8.28	0.89	2.2
diamond/tungsten	19.3	0.36	1.0

Table 3.1: The radiation length and Moliere radius of lead tungstenate crystal and the diamond-tungsten sandwich.



a)



b)

Figure 3.11: The heavy scintillator calorimeter option. a) An artistic view of the calorimeter. b) A longitudinal segment of the calorimeter with optical fibers attached.

Chapter 4

Simulation studies of the diamond-tungsten Beam Calorimeter

As mentioned in Section 2.2, the detection of high energy electrons in the BeamCal is important for new physics searches. This is a real challenge due to the huge energy deposition caused by low energy electrons and positrons originating from beamstrahlung. A high energy electron signal has to be efficiently reconstructed on top of this large background. To explore the performance of the diamond-tungsten design of the Beam Calorimeter, a full detector simulation is done.

4.1 Simulation

Simulation studies were done using the GEANT3 based simulation package BRAHMS [50]. BRAHMS performs a full detector simulation for the TESLA TDR design of the detector. The diamond-tungsten Beam Calorimeter was included in the detector description of BRAHMS. The distance between the BeamCal and the IP is 220 cm.

The calorimeter consists of 30 tungsten disks alternating with diamond sensor layers. The thickness of the tungsten disks is chosen to be 3.5 mm corresponding to one radiation length. The diamond layers are 0.5 mm thick. The longitudinal segmentation of the calorimeter is shown in Fig. 4.1 (a). Every diamond layer is segmented into pads, as shown in Fig. 4.1 (b). The number of pads per ring increases with the radius keeping pad dimensions of about half a Moliere radius (5 mm). The calorimeter has a projective geometry. The diamond layers are arranged so as to keep the projectivity

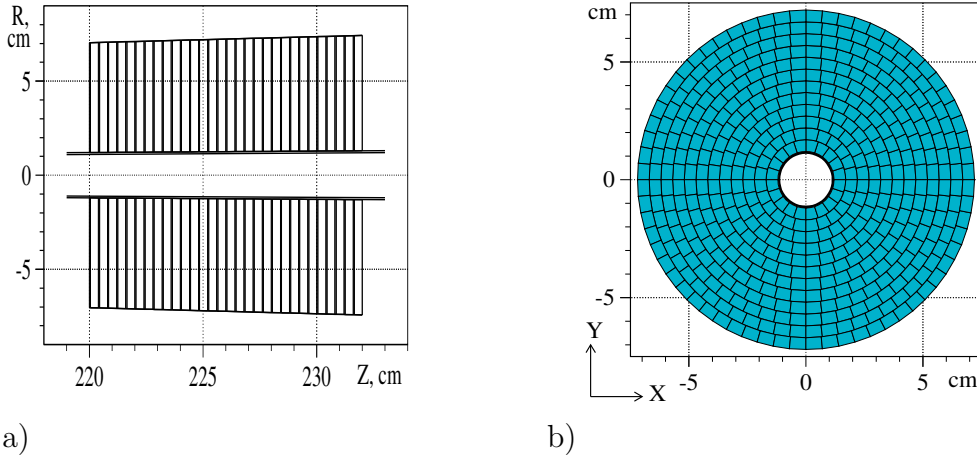


Figure 4.1: a) The longitudinal segmentation of the BeamCal. Every layer consists of a 3.5 mm thick tungsten disk and 0.5 mm thick diamond sensor. b) The transversal segmentation. The plot shows the front side of the calorimeter.

of the corresponding pads of each layer. This provides a common (θ, ϕ) -segmentation of the calorimeter.

As shown in Section 3.2.1, the energy distribution of the e^+e^- pairs originating from beamstrahlung varies significantly with the polar and azimuthal angles (Fig. 3.8 (c)). To check the influence of the background on the reconstruction efficiency, two regions of the calorimeter are studied. The segments at an azimuthal angle around $\phi = 90^\circ$ are considered as a region with a high background level. As a low background region the segments at an azimuthal angle around $\phi = 0^\circ$ were studied.

For every considered (θ, ϕ) -segment 500 single high energy electrons of a certain energy E were generated. The electron tracks originate from the IP. The momentum vector $\vec{p}_e = (|\vec{p}_e|, \theta_e, \phi_e)$ of the electrons is generated so as to provide a uniform hit distribution in the considered segment:

$$|\vec{p}_e| = E/c ,$$

$$\theta_e = \arctan \sqrt{\eta_1 \tan^2 \theta_{max} + (1 - \eta_1) \tan^2 \theta_{min}} ,$$

$$\phi_e = \phi_{min} + \eta_2(\phi_{max} - \phi_{min}) ,$$

for a segment covering $\theta_{min} < \theta < \theta_{max}$ and $\phi_{min} < \phi < \phi_{max}$ polar and azimuthal angles respectively. η_1 and η_2 are random numbers uniformly distributed in the interval $[0, 1]$.

Background events containing electrons and positrons produced by beamstrahlung in one bunch crossing are generated using the Monte Carlo program

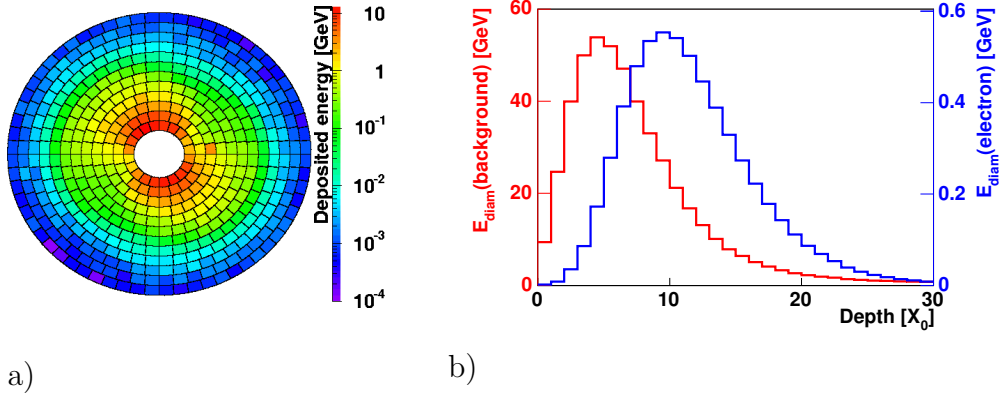


Figure 4.2: a) The transverse distribution of the energy deposited in diamond layers of the calorimeter. The deposition from the beamstrahlung pairs corresponding to one bunch crossing is shown together with the energy deposition caused by a 250 GeV electron. b) Longitudinal distributions of the energy deposited in the calorimeter. The energy deposition in the diamond layers caused by the background (red) and by the 250 GeV (blue) are shown.

Guinea Pig [45]. The nominal TESLA beam parameters are used. A full simulation of shower development caused by a background event is performed.

In order to form a signal event, for every diamond pad the energy deposition caused by a background event is summed with the corresponding energy deposition from a single high energy electron.

Fig. 4.2 (a) shows the transverse distribution of the energy deposited in the diamond layers of the calorimeter for a single event. The deposition caused by background pairs is shown together with the energy deposition caused by a 250 GeV electron. In some areas the background energy deposition is several times higher than the deposition from the electron. However, due to the relatively low energy of beamstrahlung remnants, the background and a high energy electron have different longitudinal distributions of the energy deposited in the calorimeter. The longitudinal distributions for the background and for a 250 GeV electron are shown in Fig. 4.2 (b).

4.2 Reconstruction

To recognize the local energy deposition caused by a high energy electron a reconstruction algorithm is applied [48]. As a first step, the average background energy deposition per bunch crossing and the corresponding root-mean-square (RMS) values are calculated for every diamond pad using ten consecutive bunch crossings. For a signal event, this average background

energy deposition is subtracted from the deposition of each pad.

Then the pads which are located between the 4th and 17th longitudinal layers are considered. If they have a remaining deposition larger than a threshold value, the pads are selected. The threshold is defined as a maximum of two values, either three times the background RMS in the considered pad or the threshold energy $E_{thr} = 5.5 \text{ MeV}$ which corresponds to the energy deposited by 20 minimum ionizing particles in a diamond pad.

Then a search is made for longitudinal chains of pads in the same (θ, ϕ) -segment. If a chain of more than 9 not necessarily consecutive selected diamond pads is found, a shower candidate is defined and its neighbor segments are considered. If more than five pads are selected within a neighbor segment, a cluster is defined. For every segment (θ_i, ϕ_i) in the cluster, the energy deposition E_i is calculated summing the remaining energy of the selected pads.

Polar and azimuthal angles of the reconstructed cluster are calculated as an energy weighted mean using the central and neighbor (θ, ϕ) -segments:

$$\theta = \arctan \frac{\sum_i \tan \theta_i \cdot E_i}{\sum_i E_i},$$

$$\phi = \frac{\sum_i \phi_i \cdot E_i}{\sum_i E_i},$$

where the sum is taken over all segments (θ_i, ϕ_i) of the cluster. The coordinates (θ_i, ϕ_i) are taken for the center of a segment.

The energy of a reconstructed cluster E_{reco} is defined as

$$E_{reco} = \sum_i E_i.$$

Fig. 4.3 (a) shows the energy distribution of the reconstructed clusters obtained for 100 GeV electrons.

The reconstructed energy depends linearly on the energy of the generated electron. Fig. 4.3 (b) shows an example of such a dependence for one of the considered calorimeter segments. Each point is obtained using 500 reconstructed clusters for every value of the electron energy. The reconstructed energy also depends on the background level in the considered calorimeter area, thus this dependence is individual for every considered segment.

4.3 Fake rate and detection efficiency

The number of reconstructed clusters exceeds the number of the generated electrons by about 5%. These 5% here and further are referred to as "fake"

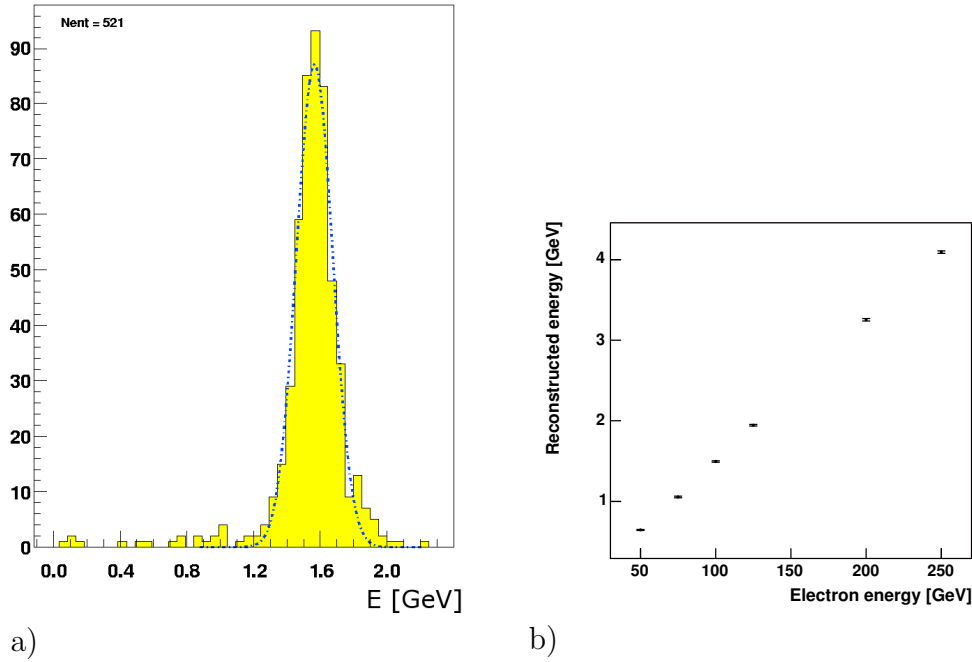


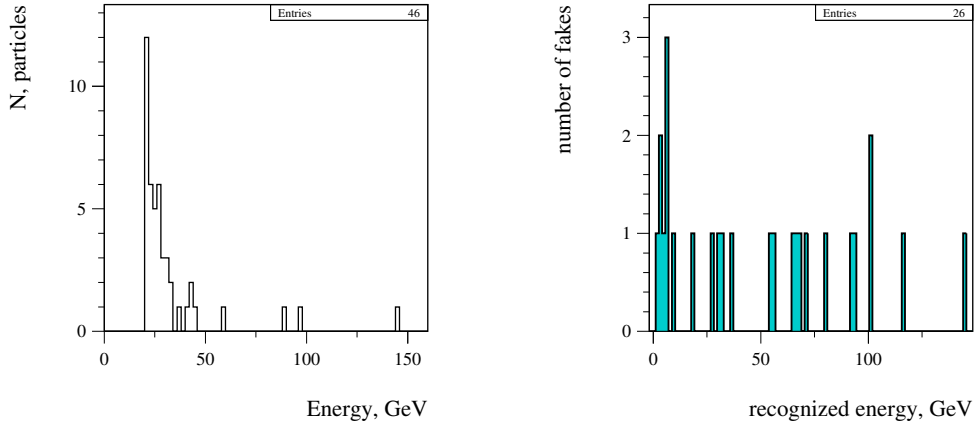
Figure 4.3: a) The energy distribution of reconstructed clusters. The distribution is obtained using 500 electrons generated at 100 GeV energy which hit a certain calorimeter segment. b) The energy of reconstructed clusters as a function of the energy of generated electrons. The calibration is done for a certain calorimeter segment using 500 electrons for every value of the electron energy.

electrons. They have a relatively low energy and provide the low energy tail of the reconstructed energy distribution, which is seen in Fig. 4.3 (a).

The fake electrons originate either from an energetic background electron or positron or from background fluctuations. The former source of fake electrons can be seen from Fig. 4.4 (a), which shows the energy distribution of electrons or positrons from beamstrahlung at the generator level. Only energetic particles with energy larger than 20 GeV are shown. The statistics corresponds to 500 bunch crossings. For one bunch crossing about 1% of the particles have energy larger than 50 GeV.

Fake electrons were studied by applying the reconstruction algorithm to pure background events. The energy distribution of clusters reconstructed from pure background events is shown in Fig. 4.4 (b). For one bunch crossing about 2% of the fake electrons have energy larger than 50 GeV.

To estimate the detection efficiency the polar and azimuthal angles of the reconstructed clusters were compared with the ones of the corresponding generated electrons. If their (θ, ϕ) coordinates on the calorimeter face plane



a)

b)

Figure 4.4: Fake electrons caused by pure background events. The statistics corresponds to 500 bunch crossings. a) The energy distribution of the generated background electrons and positrons with energy larger than 20 GeV. b) The energy distribution of clusters reconstructed from pure background events.

differ not more than by one Moliere radius, the reconstructed clusters are selected. The distribution of the reconstructed energy was fitted with a Gaussian. The number of events with an energy within a 3σ interval of the Gaussian, $N_{3\sigma}$, was calculated. The efficiency ε was determined as $\varepsilon = N_{3\sigma}/N_{gen}$, where $N_{gen} = 500$ is the number of generated single electrons.

The efficiency to identify an electron of 50, 100 and 250 GeV energy as a function of the polar angle is shown in Fig. 4.5 for the low and high background regions. An electron of 250 GeV is detected even in the high background region with almost 100% efficiency. Electrons with an energy of 100 GeV can be efficiently detected in most polar angle coverage of the calorimeter, except for the segments strongly affected by the pair background. Electrons with an energy of 50 GeV can be detected only at polar angles larger than $\theta \sim 15$ mrad.

The efficiency drop at the first two radial segments ($\theta < 10$ mrad) is a result of two effects. Near the beampipe the background level is very high even for the selected "low background" region. Besides this, for high energy electrons hitting the first two rings a shower leakage occurs that diminishes the deposited energy and makes the reconstruction less efficient.

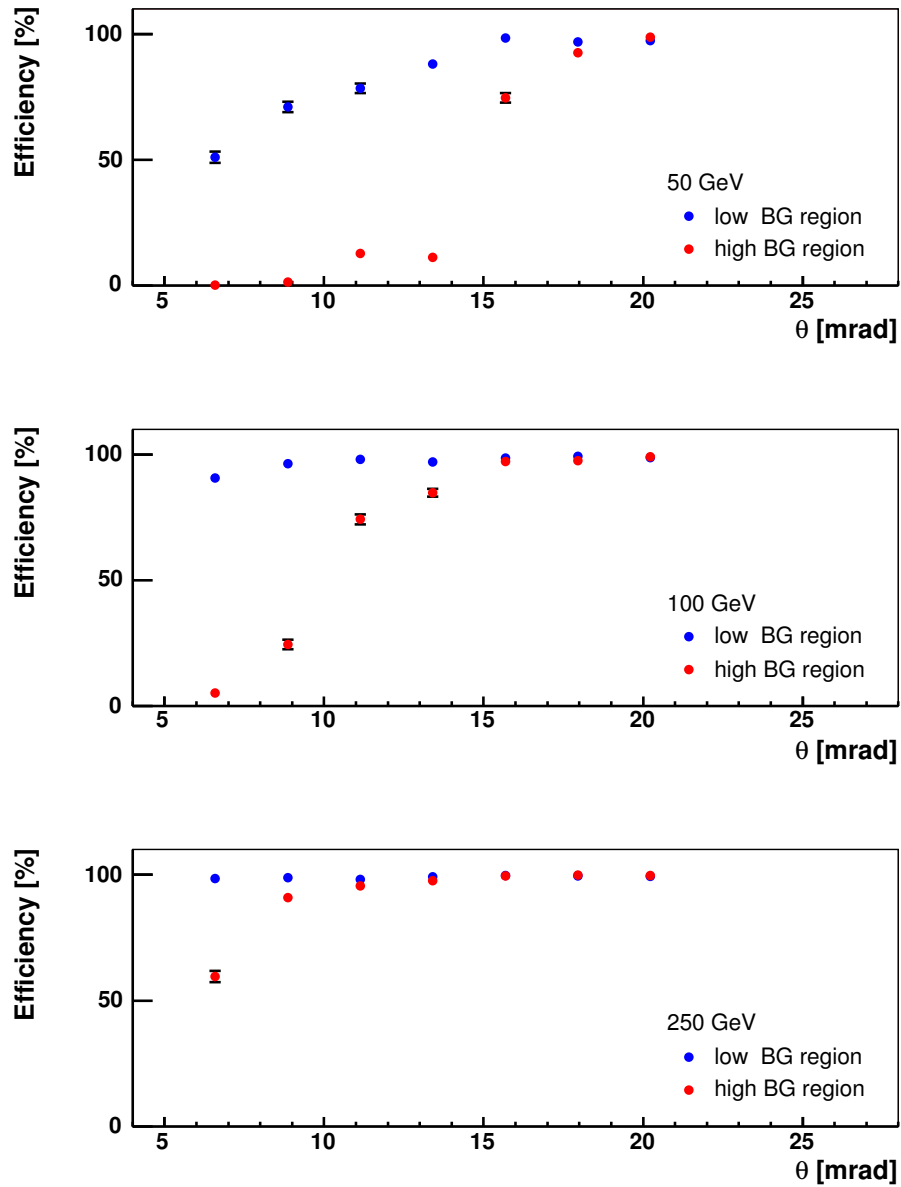


Figure 4.5: The efficiency to identify an electron of 50, 100 and 250 GeV energy in the high and low background regions.. The efficiency is shown as a function of the polar angle.

4.4 Energy resolution

The relative energy resolution of a calorimeter, σ_E/E , can be parameterized as

$$\frac{\sigma_E}{E} = \frac{p_0}{\sqrt{E}} \oplus \frac{p_1}{E} \oplus p_2 ,$$

where the right hand side is the square root of the quadratic sum of the three terms. The stochastic term p_0/\sqrt{E} represents the statistical nature of a shower development. The second term p_1/E includes effects which do not depend on the particle energy. Usually this term represents instrumental effects like electronics noise and pedestal fluctuation. The systematic term p_2 may appear due to detector non-uniformity or calibration uncertainty [51].

4.4.1 Intrinsic energy resolution

If no shower leakage occurs, the intrinsic resolution of a sampling calorimeter is defined by sampling fluctuations. The energy deposited in active layers of the calorimeter or visible energy, E_{vis} , is just a small fraction of the total deposited energy E . The visible energy is proportional to the total energy E and depends on the thickness of the absorber layers. If the sampling frequency τ is defined as the number of radiation lengths of the absorber material interspaced between two consecutive active layers¹ and the absorber layers are relatively thick ($\tau > 0.8$) [52], then

$$E_{vis} \propto \frac{E}{\tau} .$$

The intrinsic energy resolution is defined by fluctuations of the visible energy:

$$\frac{\sigma_E}{E} = \frac{\sigma_{E_{vis}}}{E_{vis}} .$$

On the other hand, the visible energy is proportional to the mean collision energy loss $\overline{E_{loss}}$ of shower particles (electrons and positrons) in the active layers: $E_{vis} = \overline{N_{act}} \cdot \overline{E_{loss}}$, where $\overline{N_{act}}$ is the average number of shower particles traversing the active layers.

Fluctuations in the visible energy are dominated by fluctuations in the number of particles in a shower N_{act} . Thus

$$\frac{\sigma_{E_{vis}}}{E_{vis}} \approx \frac{\sigma_{N_{act}}}{\overline{N_{act}}} .$$

¹Absorber layers of the calorimeter are assumed to be of the same thickness.

The number of shower particles has a Poisson distribution. However, since $N_{act} \gg 1$ the distribution approaches the Gaussian limit. Thus

$$\frac{\sigma_{N_{act}}}{N_{act}} \approx \frac{1}{\sqrt{N_{act}}} \propto \sqrt{\frac{\tau}{E}}$$

and the intrinsic energy resolution can be parameterized as

$$\frac{\sigma_E}{E} = \frac{p_0}{\sqrt{E}}.$$

Fluctuations of the collision energy loss due to different track lengths and Landau fluctuations of the lost energy can also be taken into account; however, this does not change the parameterization of σ_E/E .

Fig. 4.6 shows the intrinsic energy resolution of the BeamCal as a function of the electron energy obtained as a simulation result for areas where no shower leakage occurs. For every value of the electron energy the resolution is estimated as visible energy resolution $\sigma_E/E = \sigma_{E_{vis}}/E_{vis}$. The distribution of energy deposited in diamond pads was fitted to a Gaussian in order to obtain the mean value, E_{vis} , and standard deviation, $\sigma_{E_{vis}}$. The intrinsic resolution is parameterized to be

$$\frac{\sigma_E}{E} = \frac{(22 \pm 1)\%}{\sqrt{E}},$$

as shown in Fig. 4.6. The energy E is expressed in GeV.

4.4.2 Energy resolution in the presence of background

Under real conditions the energy resolution of the BeamCal will be influenced by background fluctuations.

The energy of a reconstructed electron is defined by the difference between the energy deposited in the pads of the reconstructed cluster and the average background deposition in these pads (Section 4.2). This causes energy independent fluctuations of the reconstructed energy and provides the p_1/E term in the relative energy resolution.

The same time, the reconstruction algorithm excludes sensor pads with low energy deposition compared to the background RMS. This reduces the number of shower particles contributing to the visible energy, $\overline{N_{act}}$, and makes the stochastic term of the energy resolution

$$\frac{p_0}{\sqrt{E}} \propto \frac{1}{\sqrt{\overline{N_{act}}}}$$

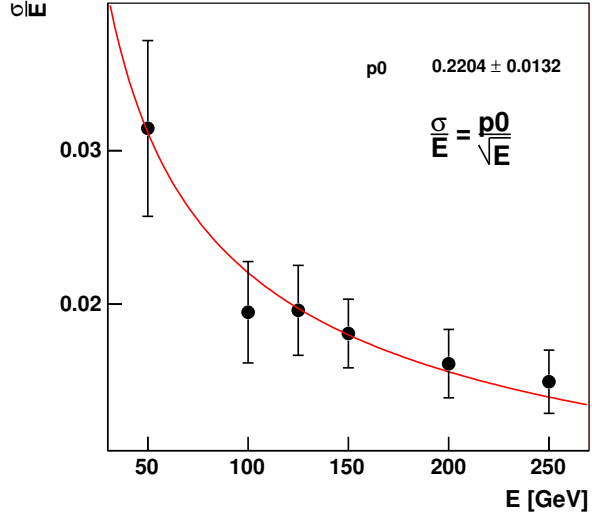


Figure 4.6: The intrinsic resolution of the BeamCal as a function of the electron energy. The parameterization is shown in the red line.

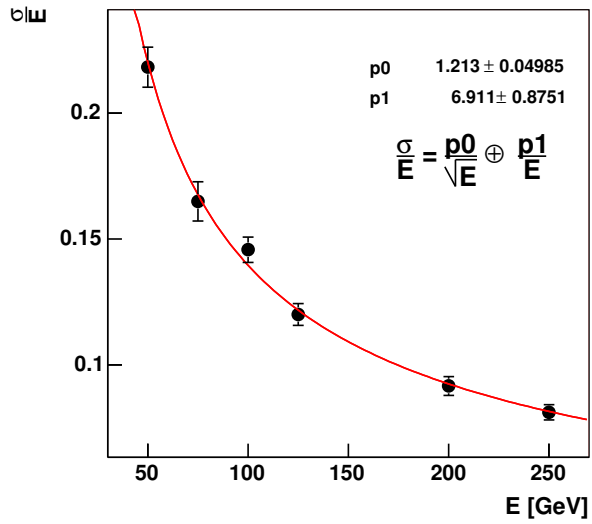


Figure 4.7: The energy resolution obtained for an individual segment ($\theta \approx 16$ mrad, $\phi \approx 0^\circ$) of the BeamCal as a function of the electron energy. The electrons are reconstructed on top of the background events. The parameterization of the energy resolution is shown in the red line.

larger in comparison to the intrinsic resolution.

Fig. 4.7 shows the energy resolution obtained for an individual segment of the BeamCal as a function of energy. It can be parameterized as

$$\frac{\sigma_E}{E} = \frac{p_0}{\sqrt{E}} \oplus \frac{p_1}{E},$$

where $p_0 = 120\%$ and $p_1 = 690\%$ for the considered segment and E is expressed in GeV. Compared to the intrinsic resolution, the stochastic term is more than 5 times larger. However, the main resolution deterioration is caused by the background fluctuation which provides the constant term p_1/E .

Due to this dominating background influence, the energy resolution of the BeamCal varies significantly over the polar and azimuthal angles, depending on the background energy density.

The energy resolution as a function of the polar angle is shown in Fig. 4.8 for 100 GeV and 250 GeV electrons in the low and high background regions. For every considered segment and for every value of the electron energy the energy distribution of the reconstructed clusters was fitted to a Gaussian in order to obtain mean value E_{vis} and standard deviation $\sigma_{E_{vis}}$.

The large values of the energy resolution in the first two radial segments ($\theta < 10$ mrad) seen in Fig. 4.8 are caused by both the high background energy density and the shower leakage. The difference between the high and low background regions is clearly seen for the first five rings ($\theta < 16$ mrad).

For larger polar angles the definition of the considered areas of the calorimeter as "high" ($\phi = 90^\circ$) and "low" ($\phi = 0^\circ$) background regions is not valid any more. The background is relatively low for both region and formed from beamstrahlung remnants of higher transverse momentum. These electrons and positrons are more deflected in the magnetic field and hit the calorimeter at larger azimuthal angles. Fig. 4.9 shows the background energy deposition in the considered regions as functions of the polar angle. The energy deposition in the "low" background regions is almost equal to the one in the "high" background regions for $\theta \approx 16$ mrad. For larger polar angles the energy deposition at $\phi = 0^\circ$ is larger than at $\phi = 90^\circ$. Thus the energy resolution in the selected "low" background region becomes worse than in the "high" background region, as seen from Fig. 4.8.

4.4.3 Influence of read-out electronics

The energy resolution of a real detector is also influenced by read-out electronics. A signal from a diamond pad of the BeamCal in terms of electrical

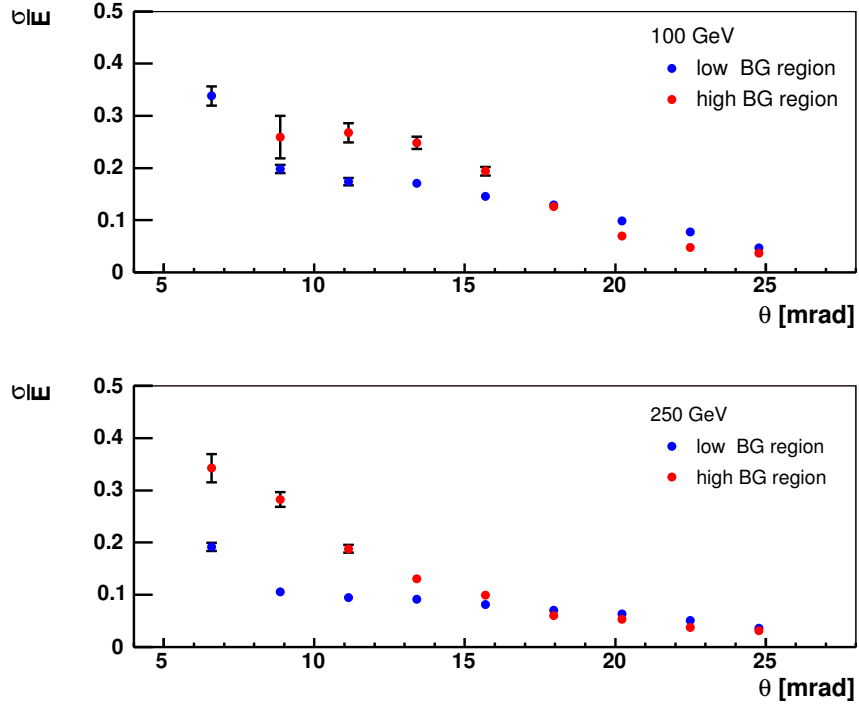


Figure 4.8: The energy resolution of the BeamCal as a function of the polar angle. The resolution is shown for the high and low background regions for 100 (top) and 250 GeV (bottom) electrons.

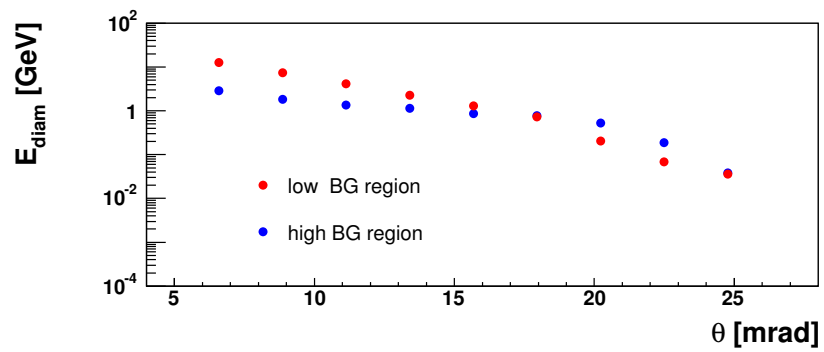


Figure 4.9: The background energy deposition in the high and low background regions as functions of the polar angle. The energy deposited in the diamond pads of the considered segments is shown.

charge is proportional to the energy deposition². The analog signal from the diamond pad is amplified and digitized. The electronic noise as well as the digitization can influence the energy resolution.

Electronic noise

To estimate the influence of electronic noise, the equivalent noise charge³ can be compared with a diamond signal (so-called "signal-to-noise ratio"). The lowest energy deposition considered in the simulation is $E_{thr} = 5.5$ MeV which corresponds to the energy deposition from 20 minimum ionizing particles (Section 4.2). Thus as the lower limit of the signal from a diamond pad, a diamond response to 20 minimum ionizing particles (MIP) was taken.

One minimum ionizing particle penetrating a diamond sensor creates about 36 electron-hole pairs per $1\ \mu\text{m}$ [53]. Thus the threshold energy corresponds to the electric charge of $Q = 20 \cdot 36\ e^- / \mu\text{m} \cdot 500\ \mu\text{m} = 3.6 \cdot 10^5\ e^-$. Even for an extremely poor charge collection efficiency of 10%, when the measured charge is just 10% of the charge created in the diamond, the signal will be $Q_{signal} = 3.6 \cdot 10^4\ e^-$.

As a practicable level of the electronic noise, $2000\ e^-$ equivalent noise charge was chosen⁴. This gives the signal-to-noise ratio of 18:1. Thus the influence of the electronic noise on the energy resolution will be negligible.

Dynamic range and digitization

The needed dynamic range of the calorimeter response is defined by the threshold energy E_{thr} and the maximal energy deposition E_{max} in a diamond pad. As mentioned, the threshold energy was chosen to correspond to 20 MIPs. The shower reconstruction done also with lower thresholds did not show any improvement of the efficiency and energy resolution.

The value of E_{max} was derived from the simulation as the maximal energy deposition which occurs in a single diamond pad. For the considered detector design $E_{max} = 2\ \text{GeV}$ that corresponds to about 7300 MIPs. Thus for the TESLA conditions the dynamic range was found to be between 10 and 10^4 MIPs.

To study the digitization influence on the energy resolution, the digitization of signals from sensor pads was included in the shower reconstruction.

²The signal formation in diamond will be discussed in details in Chapter 5.

³The equivalent noise charge is defined as the amount of charge that would be needed to be delivered to the preamplifier input to produce a signal equal to the RMS of the noise.

⁴For instance, this level of equivalent noise was reached for the luminosity calorimeter electronics of OPAL detector [36]

The area of low background density was considered. Before the reconstruction procedure, the energy deposition in every pad E_{pad} is digitized as:

$$E_{pad}^{digit} = \left\lfloor \frac{E_{pad} - E_{thr}}{E_{ch}} \right\rfloor \cdot E_{ch} + E_{thr} + E_{ch}/2 ,$$

where the floor function $\lfloor x \rfloor$ gives the largest integer less than or equal to x . The channel width E_{ch} depends on the number of channels N_{ch} :

$$E_{ch} = \frac{E_{max}}{N_{ch}} .$$

The number of channels is defined by the digitization resolution⁵ n : $N_{ch} = 2^n$.

Fig. 4.10 compares the efficiency and energy resolution for 6, 8, 10 and 12 bit digitization to the results obtained for analog values of the energy deposition. For a digitization resolution below 8 bit the efficiency to reconstruct a 50 GeV electron is 90%. For higher electron energies the efficiency is about 100% for all the considered N_{ch} .

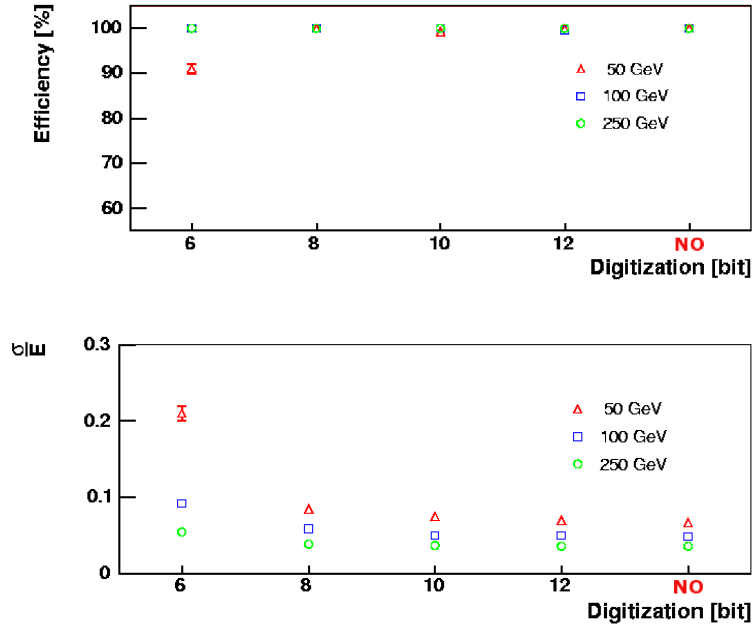


Figure 4.10: The detection efficiency and energy resolution as functions of the digitization resolution. The results for 6, 8, 10 and 12 bit digitization are compared to the results obtained for analog values of the energy deposition.

⁵Here the digitization resolution is defined as the number of bits of the analog-to-digital convertor.

The energy resolution obtained with a 6 bit digitization degrades with respect to the one obtained with analog values even for 250 GeV electrons. With a resolution above 8 bit the digitization has no visible influence on the energy resolution. Thus a 10 bit digitization is considered to be reasonably precise.

4.5 Angular resolution

As described in Section 4.1, the direction of the generated single electrons are randomly chosen to produce a homogeneous distribution of impact points within each considered segment. Polar and azimuthal angles of a reconstructed electron are calculated as an energy weighted mean using a cluster of calorimeter segments as described in Section 4.2.

The reconstructed coordinates are shifted with respect to the generated ones to the center of the segment where the shower develops, as illustrated in Fig. 4.11. Fig. 4.11 (a) shows the polar angle distribution of a sample of electrons generated in a segment $\theta_{min} < \theta_{gen} < \theta_{max}$. Fig. 4.11 (b) shows the polar angle distribution of the same sample after reconstruction.

In order to unbias the distribution of reconstructed polar angles θ_{reco} , the corrected values, θ_{reco}^{corr} , are calculated within every segment covering the polar angles $\theta_{min} < \theta < \theta_{max}$ as

$$\theta_{reco}^{corr}(\theta_{reco}) = \theta_{min} + (\theta_{max} - \theta_{min}) \cdot P(\theta_{reco}) ,$$

where the mapping function $P(\theta_{reco})$ is defined as the cumulative distribution of the reconstructed polar angle θ_{reco} :

$$P(\theta_{reco}) = \frac{1}{N_{reco}} \int_{\theta_{min}}^{\theta_{reco}} \frac{dN_{reco}}{d\theta} d\theta .$$

Fig. 4.11 shows an example of the mapping function (c) and the distribution of the corrected values θ_{reco}^{corr} (d).

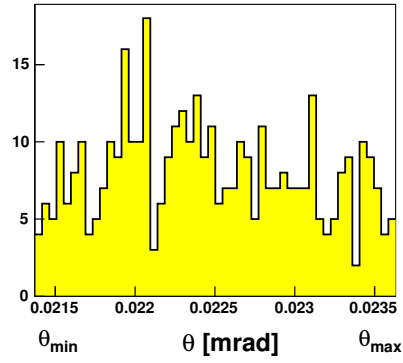
For the corrected values of the reconstructed polar angle the deviation from the corresponding generated polar angle is calculated:

$$\delta\theta = \theta_{gen} - \theta_{reco}^{corr} .$$

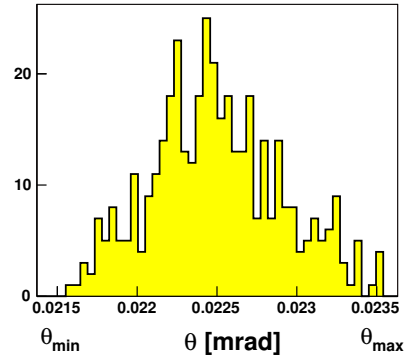
The distribution of the deviations $\delta\theta$ has a Gaussian shape. The polar angle resolutions is taken as the standard deviation of the Gaussian fit.

The azimuthal angle resolution is obtained the same way.

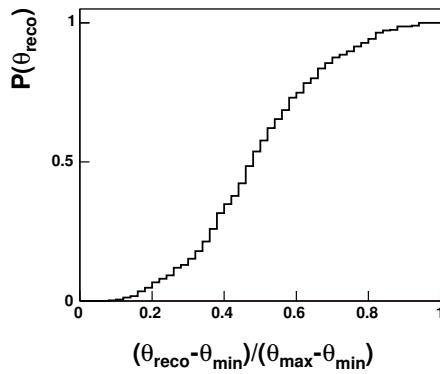
The obtained polar and azimuthal angle resolutions are shown in Fig. 4.12 and Fig. 4.13 respectively. The results are shown for segments where the



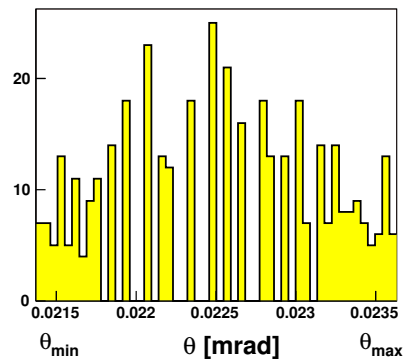
a)



b)



c)



d)

Figure 4.11: An example of polar angle distributions of electrons generated to hit uniformly a calorimeter segment (a), the corresponding distribution of the reconstructed electrons (b), the mapping function (c) and the obtained distribution of corrected values (d). The considered calorimeter segment covers the polar angles $\theta_{min} < \theta < \theta_{max}$.

detection efficiency is higher than 25%. For areas near the beampipe, where the background energy deposition is very high and shower leakage occurs, the angular resolution is defined by the segment size.

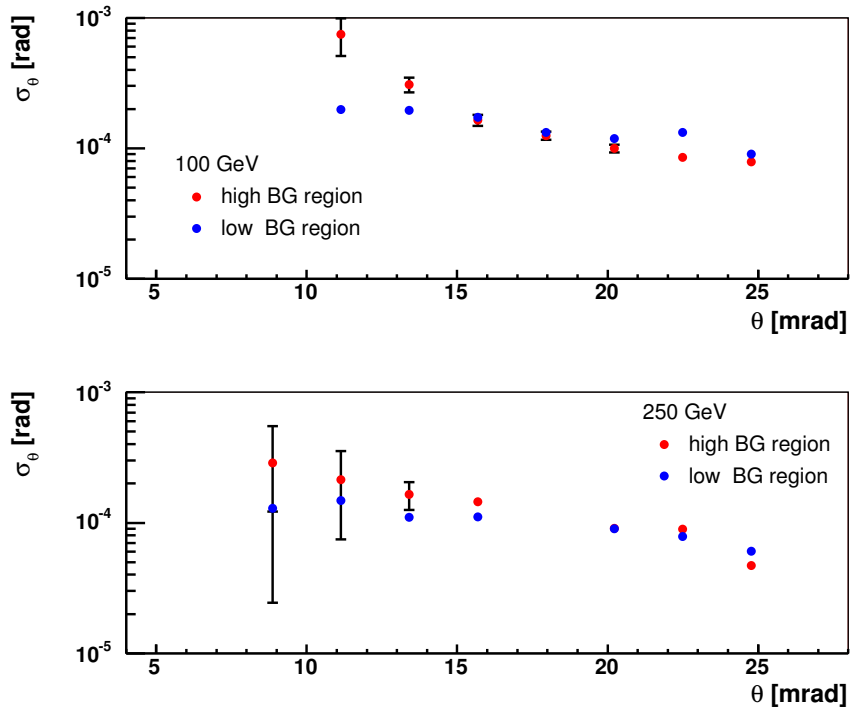


Figure 4.12: The polar angle resolution of the BeamCal as a function of the polar angle. The resolution is plot for the high and low background regions for 100 (top) and 250 GeV (bottom) electrons. At the larger polar angles, $\theta > 20$ mrad, the errors of the polar angle resolution are less than 10^{-5} mrad.

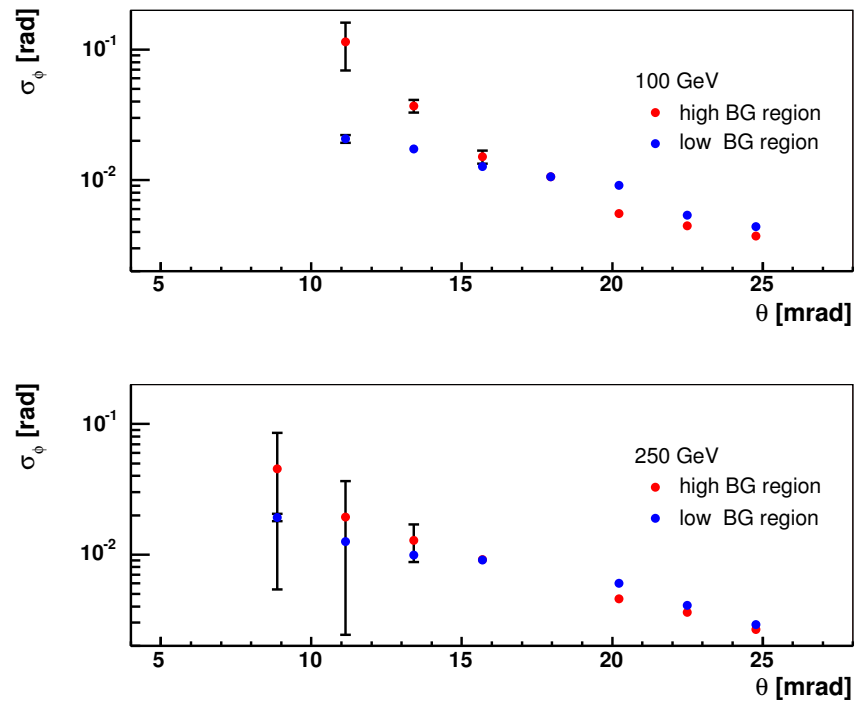


Figure 4.13: The azimuthal angle resolution of the BeamCal as a function of the polar angle. The resolution is plot for the high and low background regions for 100 (top) and 250 GeV (bottom) electrons. At the larger polar angles, $\theta > 20$ mrad, the errors of the azimuthal angle resolution in this area are less than $5 \cdot 10^{-4}$ mrad.

Chapter 5

CVD diamond

During the last 10 years chemical vapour deposition (CVD) diamonds were intensively studied as a particle detector material. Requirements on detectors for high energy and heavy ion experiments induced searches for radiation hard or/and fast sensors. The same time the fast development and improvement of the CVD technologies led to the production of polycrystalline diamonds of relatively high quality and large area. Since 1994 very intense studies of CVD diamonds for detector applications are being carried on by the RD42 collaboration at CERN¹.

Table 5.1 shows basic properties of diamond in comparison to silicon. However, one should notice that the properties are given for an intrinsic single crystalline diamond while for detector application mostly polycrystalline CVD (pCVD) diamonds are used. In this case the properties might be different and depend on the growth conditions.

The high resistivity of diamond (for polycrystalline CVD usually higher than $10^{11} \Omega \text{ cm}$) provides a small leakage current of a detector. The dielectric constant is almost twice lower than the one of silicon and leads to a lower capacitance of the detector and to the correspondingly lower noise. For a single crystalline diamond charge carrier mobilities depend on purity and might be up to 4500 (electrons) and $3800 \text{ cm}^2 \text{ V}^{-1} \text{ s}^{-1}$ (holes) [56]. For polycrystalline diamonds the effective mobilities might be in the range of $1 - 1000 \text{ cm}^2 \text{ V}^{-1} \text{ s}^{-1}$ [57, 58]. Also attractive properties of diamond are the high thermal conductivity (five times higher than the one of copper) and chemical inertness.

Radiation hardness of pCVD diamond was studied for hadrons as well as for electromagnetic radiation. Less than 15% of signal reduction was reported for a 24 GeV proton fluence of $\sim 2 \cdot 10^{15} \text{ cm}^{-2}$ and for pions of

¹<http://greybook.cern.ch/programmes/experiments/RD42.html>

	Diamond	Silicon
density [g/cm ³]	3.52	2.32
dielectric constant	5.7	11.9
resistivity [Ω cm]	$\sim 10^{16}$	$2.3 \cdot 10^5$
breakdown field [V μm^{-1}]	1000 [54]	30 [53]
thermal conductivity [W cm ⁻¹ K ⁻¹]	20 [55]	1.3 [55]
thermal expansion coefficient [K ⁻¹]	$0.8 \cdot 10^{-6}$ [55]	$2.6 \cdot 10^{-6}$ [55]
crystal structure	diamond	diamond
lattice constant [\AA]	3.57	5.43
band gap [eV]	5.47	1.12
ionization energy [eV]	13 [53]	3.6 [53]
energy to remove an atom from the lattice [eV]	80 [55]	28 [55]
saturated carrier velocity [cm s ⁻¹]	$2.7 \cdot 10^{10}$ [54]	$8.2 \cdot 10^9$ [53]
electron mobility [cm ² V ⁻¹ s ⁻¹]	4500 [56]	1350
hole mobility [cm ² V ⁻¹ s ⁻¹]	3800 [56]	480
ionization density (MIP) [eh/ μm]	36 [53]	92 [53]
radiation length [cm]	12 [53]	9.4 [53]

Table 5.1: Properties of intrinsic single crystalline diamond and silicon at normal conditions.

$\sim 1 \cdot 10^{15}$ cm⁻² [59]. Almost no changes in detection properties was observed for 10 MGy collected dose of electromagnetic radiation [47].

A variety of different pCVD diamond detectors have been designed and tested. Pixel detectors have been developed and tested by the RD42 collaboration as prototypes of ATLAS and CMS vertex detectors [60]. In the BaBar Beam Monitoring system two pCVD diamond detectors are successfully operated since 2002 [61].

There are a lot of activities on diamond sensor applications in heavy ion physics at GSI. In the High-Acceptance Di-Electron Spectrometer (HADES) two diamond strip detectors are used for Time-of-Flight measurements providing an intrinsic resolution of a Start-Veto device of 29 ps [62, 63]. A large area (60×40 mm²) diamond detector is used for beam-foil spectroscopy since 2000 [63]. In a medical application of ¹²C beams a pad pCVD diamond detector is used as a beam-profile monitor. In this case the similarity of carbon with human tissue is an important advantage for the dose estimation [63].

The only reported study on diamonds for calorimetry is a test of a diamond - tungsten sampling calorimeter [64]. The energy resolution measured

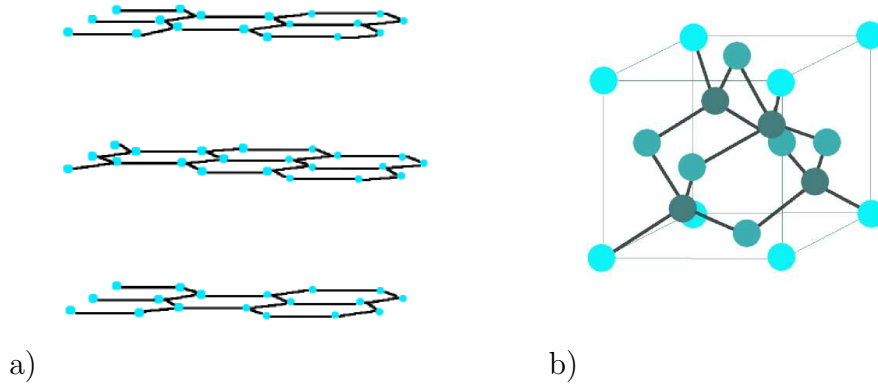


Figure 5.1: Graphite (a) and diamond (b) crystal structures.

with 0.5 – 5.0 GeV electron beams was found to be compatible with the resolution of a similar silicon-tungsten calorimeter.

5.1 CVD diamond growth

5.1.1 Carbon allotropes

There are several allotropes of carbon - graphite, diamond, fullerenes, lonsdaleite and other exotic forms. In all the forms carbon atoms bond to each other covalently. The most common and thermodynamically stable allotropes of carbon are graphite and diamond.

In graphite the sp^2 hybridization of carbon atoms provides three strong coplanar σ bonds with neighbor atoms composing planar layers of hexagonal structures. The unhybridized 2p electron of each carbon atom creates π bonding between the neighboring carbon atoms of the layer providing electrical conductivity. The layers are weakly bound to each other by the van der Waals force. The graphite crystal structure is shown in Fig. 5.1 (a).

Carbon atoms in diamond have four valence electrons equally distributed among sp^3 orbitals and form very strong tetrahedral σ bonding to four neighbor atoms. Fig. 5.1 (b) shows the diamond crystal structure.

Also amorphous carbon is often selected as an allotropic form of carbon. Amorphous carbon does not have a long-range crystalline order and usually consists of both sp^2 and sp^3 hybridized carbon. Depending on the ratio of the hybridizations, the amorphous carbon is classified as carbon-like or diamond-like.

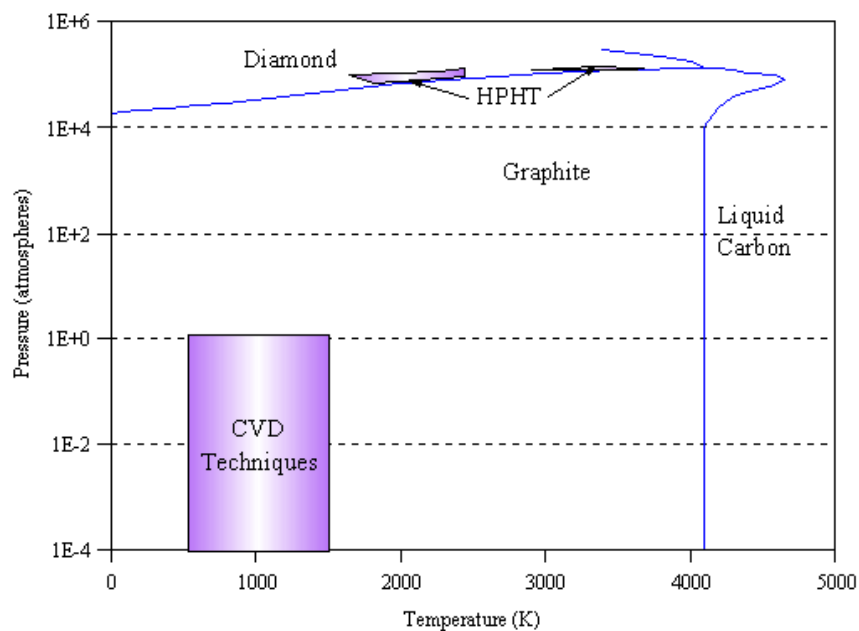


Figure 5.2: Phase diagram of carbon (after Reference [65]). Diamond is metastable at room temperature and pressure, however it does not convert to graphite because of the very high activation barrier. The CVD technique is based on chemistry and kinetics of the gas phase and surface reactions that allows the deposition of diamond at low pressures.

Fig. 5.2 shows a phase diagram of carbon. Graphite is the only thermodynamically stable form of carbon at normal conditions. Diamond, being metastable at room temperature and pressure, does not convert to graphite because of the very high activation barrier (728 kJ/mol) for the interconversion.

Since 1955 the High-Pressure High-Temperature (HPHT) technique is used for diamond production. The synthetic ("industrial") diamonds are crystallized from metal solvated carbon at a pressure of 50 – 100 kbar and a temperature of 1800 – 2300 K [66]. HPHT grown diamond usually are single crystals of a size up to several millimeters.

5.1.2 Chemical Vapour Deposition

The growth of CVD diamond is based on chemistry and kinetics of the gas phase and surface reactions. The kinetic theory of diamond nucleation and

growth was proposed by Deryagin [67] in the 1950s. Independent experiments were done by Eversole [68]. They announced a chemical vapour deposition of diamond from carbon-containing precursor gases on a heated surface of natural diamond under reduced pressure. Since the CVD growth is controlled by kinetics, the deposition of diamond (sp^3) form of carbon is possible in spite the fact that at low pressures diamond is thermodynamically metastable.

However, the deposition rate was low and the deposited films contained also the graphite phase. Later, at the end of 1960s, the role of hydrogen presence during the deposition process was discovered by Angus [69]. Since hydrogen bonds sp^2 hybridized carbon rather than sp^3 , the presence of atomic hydrogen suppresses the deposition of the graphite phase.

The CVD process involves gas-phase chemical reactions above a solid surface where the deposition occurs. A precursor carbon-containing gas (often methane) is activated in plasma, discharges or under temperatures higher than 2000 °C [70, 71].

In general the CVD diamond growth can be described as



The grown diamonds have usually polycrystalline structure except for very special cases when a single crystalline growth occurs. Facets on crystals are perpendicular to the slowest-growth crystallographic direction and seen on the growth surface as hexagonal, triangular or square structures. The first two correspond to a crystal growth in the [111] direction, the latter corresponds to the [100] direction.

The quality of a deposited diamond is determined by the ratio of graphite and diamond carbon atoms, by impurities, crystallite sizes and homoepitaxy. The latter is defined by relative rates of a new crystallographic direction generation (twinning or re-nucleation) versus a continued growth in a given direction [72].

There are three processes involved in the CVD diamond production. Activation of the gas phase, nucleation and diamond growth.

Activation

Activation provides reactive radicals for further chemical reactions. Different techniques of the CVD diamond production differ only in the activation procedures. The most common approaches are the hot filament (HFCVD), microwave plasma (MWCVD) and direct current (DC) arc jet activations. Fig 5.3 shows sketches of the corresponding CVD reactors.

The hot filament method is relatively cheap and easy to operate. A mixture of the precursor gas and hydrogen (usually about 1% of methane in

hydrogen) is fed into a reactor chamber at a low (20 – 30 Torr) pressure. A coiled metallic filament is electrically heated to a temperature above 2000 °C. A substrate maintained at 700 – 900 °C is several millimeters beneath the filament. The growth rate is usually 1 – 10 $\mu\text{m}/\text{h}$. The main disadvantage of the method is high contamination of the filament material in a deposited diamond.

In the arc jet reactor a higher gas flow is used. The gas passes through a high power electrical discharge. The produced plasma goes to a secondary chamber where the diamond deposition occurs. The most commonly used plasma jet is the DC arc jet where a direct current is driven through the gas. The main feature of the plasma jet technique is the high growth rate, usually greater than 100 $\mu\text{m}/\text{h}$. The main disadvantage of the reactor is a small area struck by the jet (usually $\sim 1 \text{ cm}^2$), limiting the size of deposited diamonds. Substrate cooling is also a problem, since maintaining uniform substrate temperatures in such a rapidly varying high power system is difficult [70].

Despite being the most expensive, the microwave activation technique is the most common since the produced diamonds are of high purity. For the gas activation a microwave power is coupled into a reactor. The plasma is induced by free electrons produced in the gas by a cosmic muon or intentionally by a spark. The electrons gain significant energy ($\geq 10^4 \text{ K}$) from the microwave electric field and transfer it to the gas via collisions, creating the plasma.

In the NIRIM-type reactor the plasma is activated in a quartz tube. The microwave power is coupled to the tube via a waveguide. The substrate is heated by the plasma that limits the control of a substrate temperature. The quartz walls of the reactor might cause oxygen and silicon contaminations in the deposited diamond [73].

In the ASTEX-type reactor microwaves are coupled into a stainless steel chamber through a quartz window via an antenna. The plasma can be generated above the substrate what allows almost independent control of the substrate temperature. Stainless steel walls of the reactor volume serve higher purity of the deposited diamonds and allow also higher microwave power providing a growth rate larger than 10 $\mu\text{m}/\text{h}$.

A novel ellipsoidal design of a microwave plasma reactor developed by the Diamond Group of Fraunhofer Institute für Angewandte Festkörperphysik (Fraunhofer IAF) [74] in cooperation with the AIXTRON AG [75] is optimized for large area deposition of diamond wafers. The reactor is based on the ASTEX-type, however the ellipsoidal cavity improves the quality of the large area deposition due to the optimal focusing of the microwave energy into an intense and extended plasma [76].

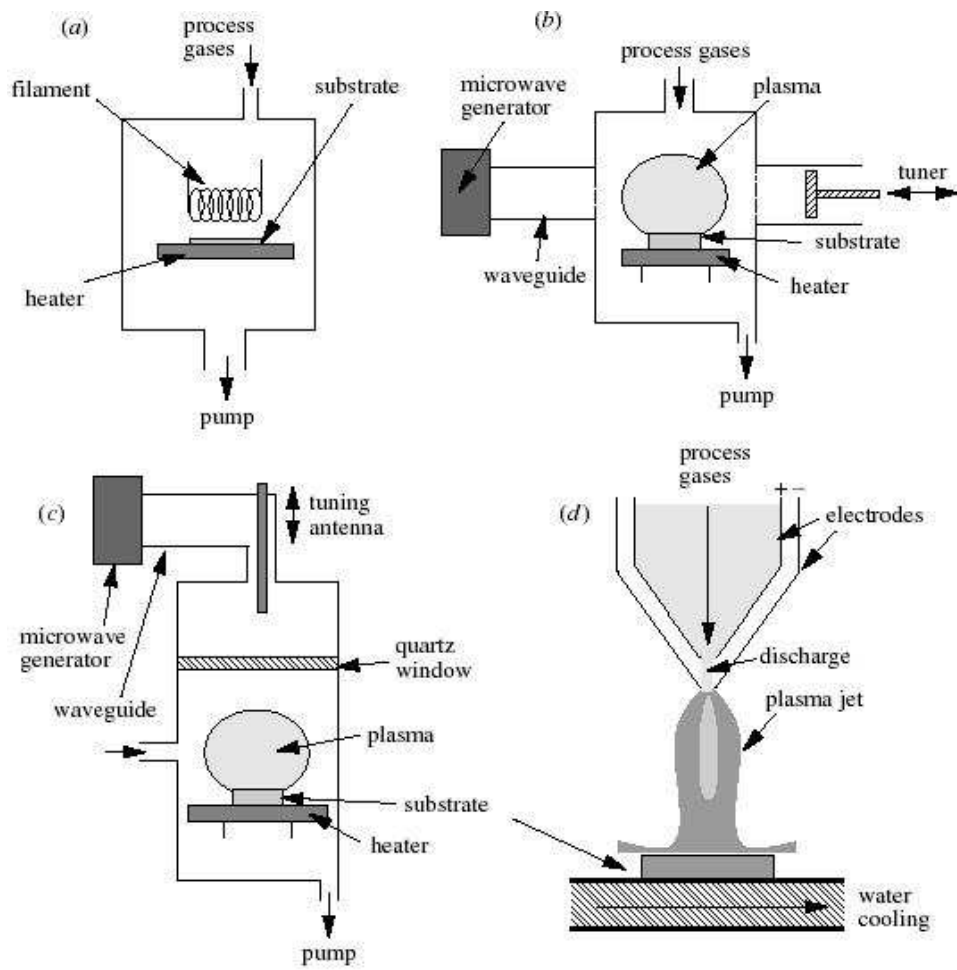


Figure 5.3: Hot filament (a), microwave NIRIM (b) and ASTEX (c) and DC arc jet (d) CVD reactors (after Reference [70]).

Nucleation

To start a diamond growth individual carbon atoms should be nucleated onto a substrate surface forming an initial sp^3 tetrahedral lattice. The surface nucleation includes the following stages [77]:

- Atoms from the gas collide with the substrate surface and are adsorbed. The carbon adatoms may desorb back into the gas phase, diffuse along or into the substrate surface or react with the substrate material (depending on the substrate material).
- When some critical concentration of surface carbon is reached, the carbon adatoms start to bond with each other forming clusters.
- The clusters grow or decay in size depending upon their thermodynamic stability, rate of atom addition from the gas phase and surface diffusion from the surrounding substrate.
- Once the clusters reach a critical size, they become thermodynamically stable and will continue to grow as new atoms are adsorbed.

Some of the processes strongly depend on the the substrate material so the choice of the substrate plays a crucial role in the diamond nucleation and consequently in the quality of the final grown film.

Obviously, the best substrate material is diamond (natural or HPHT) which provides the exact template for the diamond lattice. During the growth procedure the lattice is just extended atom-by-atom as deposition proceeds [70] forming a homoepitaxial diamond. Cubic boron nitride (cBN) has a crystal structure identical to the diamond one and similar thermal expansivity so it can also provide a highly oriented diamond growth. The main problem of the homoepitaxial growth is a limitation in the substrate size.

The growth process on non-diamond substrates usually gives heteroepitaxial diamonds.

There are two important conditions which must be satisfied to start the non-epitaxial nucleation on a substrate surface layer [77]:

- the surface must have high-energy surface sites (unsatisfied valences);
- the carbon saturation of the surface layer must be reached.

The best non-diamond substrates are materials capable of a carbide formation. At the first stage a carbide layer formation occurs. Diamond nucleation starts on the carbide layer only when the carbon concentration on the surface reaches its saturation value. Some metals, like Ti, W, Mo, Al and

Cr, non-metals, such as B, Si and Si-containing compounds, form carbide layers. In some metals, such as Ti, the carbide layer continues to grow even during diamond deposition and can become hundreds of micrometers thick what might influence the properties of the deposited diamond [70]. Materials with high carbon diffusivities had the longest incubation period since they required much longer time to achieve saturation concentration of the surface carbon [77].

In practice, different carbon forms of initial deposition may occur. For instance, for silicon, which is one of the most often used substrate materials, diamond nucleation occurs on the SiC intermediate layer and no further carbide layer growth occurs after the surface is covered with diamond. However, a diamond-like carbon and graphite formation has also been observed.

As an important step in the diamond deposition a surface pretreatment should be mentioned. Since the nucleation occurs primarily on substrate defects (scratches, grain boundaries, dislocations), the substrate surface is often treated mechanically by polishing with diamond grit. There are also a variety of other approaches, like chemical etching, ion implantation, pulsed-laser irradiation or precoating with various carbon films. All of them are purposed to increase the nucleation density.

Growth

When the nucleated cluster have reached the critical size and the nucleation process is finished, the diamond growth continues in three dimensions till the cluster coalesces with neighbor ones. Since this stage the growth occurs only in one direction upward from the substrate providing a columnar structure of the diamond. Such columns of single crystals provide a large number of defects and grain boundaries in the bulk of the diamond. Depending on the growth conditions the single crystalline columns can have some degree of preferred orientation of the crystal planes.

As the film becomes thicker, the crystal size increases also in the plane perpendicular to the growth direction and the number of grain boundaries decreases. Thus the outer layers of the grown diamond (so-called "growth side") are usually of much better quality than the initial nucleated layers ("substrate side").

As mentioned above, atomic hydrogen plays a crucial role in the assistance of the diamond growth.

- sp^3 carbon just deposited on the surface of a growing diamond has a non-terminated bond (since the next "upper" layer of the lattice is still missing). The bond can be terminated by a hydrogen radical that

prevents graphitization:

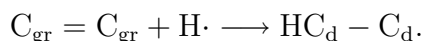


Although in fact the reaction is reversible, the reverse reaction rate is negligible [70].

- Hydrogen radicals serve for so-called H-abstraction, bonding a hydrogen atom from the H-terminated surface carbon:



- Hydrogen etches both sp^3 and sp^2 carbon from the diamond surface, but reacts much faster with sp^2 atoms removing graphite from the film surface back to the gas phase.
- Atomic hydrogen may saturate unsaturated (sp^2) clusters:



where C_{gr} denotes sp^2 surface carbon and C_{d} denotes the sp^3 one. However, the reverse reaction (thermal decomposition of the diamond structure) also takes place and the resulting process depends on the surface temperature [71, 78].

- Hydrogen prevents polymerization in the gas phase.

The chemistry of the diamond growth is not fully understood, there are different approaches being discussed. However, it is more or less commonly admitted that under typical growth conditions most of the carbon atoms originate from methyl radicals $\text{CH}_3 \cdot$ [72].

Fig 5.4 shows an example of diamond growth by methyl addition. At first stage, one of the surface carbon radical formed by the H-abstraction (a) combines with a gaseous methyl radical (b). At the next stage, when the H-abstraction of an adjacent terminated carbon occurs (c), the two radicals form C – C bonds, completing the surface carbon ring (d).

5.2 Electrical properties of pCVD diamond

5.2.1 Conductivity

The electrical properties of CVD diamond are mainly defined by defects and charge traps, which originate from impurities and grain boundaries in case of polycrystalline CVD diamonds and thus strongly depend on growth conditions.

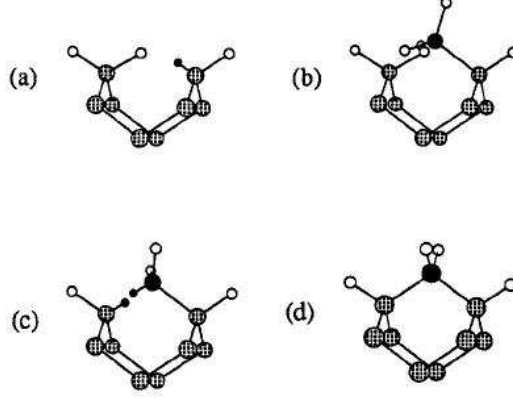


Figure 5.4: An example of diamond growth by methyl addition (after Reference [71]). At the first stage, one of the surface carbon radical formed by the H-abstraction (a) combines with a gaseous methyl radical (b). At the next stage, when the H-abstraction of an adjacent terminated carbon occurs (c), the two radicals form C – C bonds, completing the surface carbon ring (d).

Conductivity of ideal intrinsic diamond

As mentioned above, a pure and defect-less single crystal diamond is an insulator with a very high band gap energy ($E_g = 5.48$ eV). The free charge carrier concentrations can be estimated using Boltzmann statistics as

$$n_{c,v} = N_{c,v} \exp \left\{ -\frac{|E_{c,v} - E_F|}{kT} \right\},$$

where n_c is the electron and n_v is the hole concentration, E_c is the energy at the bottom of the conduction band, E_v is the energy at the top of the valence band, E_F is the Fermi level, k is the Boltzmann constant and T is the temperature. The effective densities of states in the conduction and valence bands, N_c and N_v , are given by

$$N_{c,v} = 2 \left(\frac{m_{c,v}^* kT}{2\pi\hbar^2} \right)^{3/2},$$

where m_c^* is the effective mass of an electron in the conduction band and m_v^* is the effective mass of a hole in the valence band. The steady state concentration of holes in the valence band equals the concentration of electrons in the conduction band:

$$n_c = n_v = \sqrt{N_c(T)N_v(T)} \exp \left\{ -\frac{E_g}{2kT} \right\}$$

where $E_g = E_c - E_v$ is the forbidden band width. Taking $N_c \sim N_v \sim 10^{19} \text{ cm}^{-3}$ [79] at room temperature and the diamond band gap of 5.48 eV one gets 10^{-29} cm^{-3} . Thus the conduction by means of intrinsic charge carriers is negligible.

Intra-grain defects

The following defects may occur and play a role in the conductivity of undoped CVD diamonds:

- Vacancies. Vacancies are believed to be a characteristic feature of CVD diamonds, in natural and HPHT diamonds the vacancies are present only after irradiation [80].
- Nitrogen presence in a gas mixture during CVD growth causes a variety of defects. Single substitutional nitrogen atoms give a deep donor level with an ionization energy of 1.7 – 2.0 eV [80]. However, the fraction of single nitrogen was reported to be at a level of 1 – 5% of the total nitrogen concentration in diamonds [54]. Since the binding energy of N_2 is rather large, the complete dissociation of N_2 in the microwave plasma is very unlikely and most of the nitrogen might be contained in diamond in an aggregated state [54].

The simplest aggregated state (A-aggregate) consists of a pair of neighboring substitutional nitrogen atoms. The A-aggregate is believed to be a donor with an ionization energy of 3.8 – 4.0 eV [80, 81].

The complex of nitrogen-vacancy [N-V] produces a deep acceptor level with ionization energy of $\sim 2.6 \text{ eV}$ [81].

- Silicon-vacancy complex [Si-V] also occurs only in CVD diamond and gives a deep acceptor level [81].
- A hydrogen presence is often observed in the vicinity of grain boundaries of CVD diamond and supposed to be a deep acceptor level [81, 54].

Grain boundaries

The grain boundaries play a crucial role in the electrical properties of polycrystalline CVD diamond. Since carbon atoms at the grain boundary are disordered and may have dangling bonds, the lattice structure has a lot of defects there what results in formation of trapping states.

In Seto's model for polycrystalline semiconducting films [82] the grain boundary traps capture and immobilize free carriers what finally creates

potential barriers. The traps are assumed to be neutral when empty and charged when filled. Fig. 5.5 shows the energy band structure of polycrystalline material in the presence of electron traps. The height of the potential barrier depends on the grain size and the trap density. In general traps can be charged when empty and neutralized when filled. Such a picture was observed in [83, 84] for polycrystalline CVD diamond.

The presence of the amorphous carbon phase in pCVD diamonds was reported in [85, 86, 87]. Amorphous carbon was observed even in a case of highly transparent pCVD diamonds [85]. The most probable location of the amorphous carbon are grain boundaries. Fig. 5.6 shows a model of the density of states of amorphous carbon. Obviously, the presence of amorphous carbon in a pCVD diamond provides much higher conductivity via band-tail sites of sp^3 disordered carbon and via graphite $\pi^{(*)}$ band states.

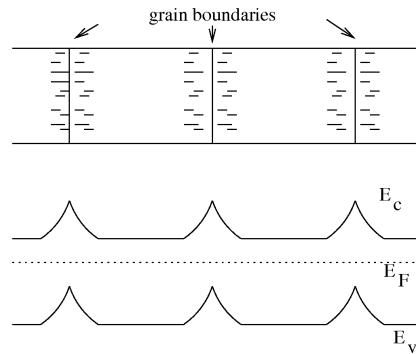


Figure 5.5: An example of potential barriers caused by negative charge carriers trapped at grain boundaries. The top sketch shows the space charges in a polycrystalline material and the bottom one shows the corresponding changes in the energy band structure.

Models of bulk-limited conduction in pCVD diamond

Since there are a variety of different and sometimes contradicting observations and models of conductivity in a polycrystalline CVD diamond, it seems to be very likely that the conductivity in pCVD diamonds strongly depends on their growth conditions and can be very different for different samples.

Several different models of bulk conductivity in diamonds are often considered.

- Poole-Frenkel models consider a steady-state current limited by the rate of emission from the charged traps. Depending on trap concentration

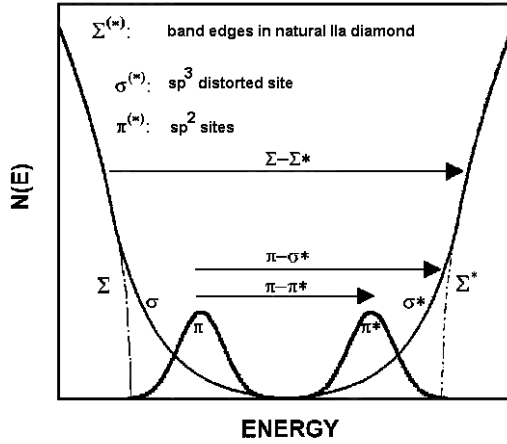


Figure 5.6: Density of states in amorphous carbon. $\Sigma^{(*)}$ bands correspond to sp^3 carbon in an ideal diamond lattice. Disordered sp^3 carbon gives the exponentially broadened tails $\sigma^{(*)}$ and sp^2 disordered carbon gives $\pi^{(*)}$ bands. (After Reference [85]).

and grain size, the Coulomb potentials surrounding the ionized traps can be considered as non-overlapping (**Poole-Frenkel conduction**) or overlapping (Poole-Frenkel conduction with overlap of Coulombic potentials or **Hill's law**). In the latter case the charge carriers hop from one trapping site to the other overcoming the potential barrier E_p and the current density can be expressed as

$$J_{Hill} \sim T^2 \exp \left\{ -\frac{E_p}{kT} \right\} \sinh \left(\frac{esF}{2kT} \right),$$

where F is an electric field applied to the sample, s is the mean separation distance between two trapping sites and e is the electron charge [88]. For low electric fields the Hill's law approaches an ohmic behavior:

$$\sinh \left(\frac{esF}{2kT} \right) \approx \frac{esF}{2kT}, \quad esF \ll kT$$

The Hill's law is very often used to explain a conductivity of pCVD diamonds [89, 90, 91, 92].

- Another conductivity type sometimes being used to describe pCVD diamond conductivity is **variable range hopping (VRH)** [89, 93]. In general VRH is often used to describe disordered insulators or semiconductors at low temperatures. The carrier transport occurs via single

localized sites of various energy. The probability of hopping to the localized site is defined by the activation energy and by the distance to the site. The competition between sites of low activation energy at big distances and sites with high activation energy localized close to the present position of the charge carrier gives the variable range of hopping. When the temperature decreases the charge carriers make longer hops. The temperature dependence of the current density (Mott's law) is the following:

$$J \sim \exp \left\{ - \left(\frac{T_0}{T} \right)^{\frac{1}{d+1}} \right\},$$

where d is the dimension size of the disordered structure. The current density of the system is also proportional to the electric field strength.

- At low temperatures or in case of high barriers the conductivity might be dominated by **tunneling** [89].
- If the density of charge carriers is high enough to cause a field gradient, this will limit the current, causing **space charge limited current (SCLC)**. In the case of a high electric field in a pCVD diamond ($F \gtrsim 2 \cdot 10^4$ V/cm), the conduction via highly disordered grain boundaries may give SCL current behavior [89], where $J \sim F^n$, $n > 1$. Often for diamond a **SCLC enhanced by Poole-Frenkel effect** is considered to take into account a presence of charged traps [94]. This gives

$$J \sim F^2 \exp \left\{ \frac{a\sqrt{F}}{kT} \right\},$$

where a is positive and depends on the dielectric constant of the material [95].

5.2.2 Electrical contacts on CVD diamonds

An ohmic contact is defined as the metal-semiconductor contact that has negligible contact resistance relative to the bulk resistance of the semiconductor (bulk limited conductivity) [96]. This requirement is satisfied if the Schottky barrier at the metal-semiconductor interface is low enough not to limit the current. Otherwise electrical properties of the device are partly or entirely defined by the contact. Such kind of contacts are called rectifying.

To characterize a contact, the specific contact resistance R_c can be used:

$$R_c \equiv \left(\frac{\partial J}{\partial V} \right)_{V=0}^{-1},$$

where J is the current density and V is the applied voltage. Thus ohmic contacts should satisfy the condition $R_c \ll R_{bulk}$, where R_{bulk} is the specific bulk resistance of the semiconductor.

The Schottky barrier arises as a consequence of a mismatch between the semiconductor and metal Fermi levels and depends on the metal work function, the electron affinity and surface state density of the semiconductor.

Since diamond is inert and has a wide band gap, there are not so many techniques and metals which provide a good ohmic contact. Titanium and chromium are widely used for ohmic contact formation on diamond [53, 55, 79, 97]. As mentioned in Section 5.1.2, these metals are able to form carbide. Studies of titanium metalization show the role of carbidization. In Reference [98] it was shown that simple evaporation of titanium on a non-treated diamond surface gives a rectifying contact with the Schottky barrier height of 1.3 eV. This corresponds to the specific contact resistance $R_c \sim 10^{13} \Omega/\text{cm}^2$. However the subsequent annealing at a temperature higher than 430°C lowers the barrier down to 0.8 eV ($R_c \sim 100 \text{ k}\Omega/\text{cm}^2$). In Reference [99] it is shown that titanium films evaporated on diamond consist of a mixed metallic and carbidic phases of titanium (Ti and $\text{TiC}_{0.56}$) up to the temperature of 430°C when the full carbidization of the titanium film (150 Å) was obtained.

The same time a pretreatment of the diamond surface plays a crucial role. Argon sputtering of a diamond surface before metalization gives ohmic contacts for titanium as well as for gold which does not form carbide [100]. In this case the subsequent annealing does not change resistance of a titanium contact [98]. However, the gold ohmic contacts become rectifying upon annealing, that makes them not reliable for practical use.

Assuming that the argon sputtering damages the surface, one can conclude that the procedure increases the concentration of surface states and lowers the Schottky barrier.

The carbidization of titanium might be interpreted in the same way as a formation of additional defects on the diamond surface.

Usually a two or three layer metalization is used. Ti/Au and Ti/Pt/Au contacts are widely used and proved to be reliable. The gold top layer prevents titanium from oxidation. In the case of three layer contacts platinum prevents the interdiffusion between the titanium and gold layers during the annealing step [101].

5.3 Signals from ionizing particles in a CVD diamond detector

5.3.1 Energy loss of particles in matter

A charged particle passing through a medium interacts with atomic electrons and nuclei. Most of the interactions are electromagnetic. The elastic scattering on nuclei does not change the energy of the particle but changes its incident direction. Inelastic collisions of a particle with atomic electrons cause energy loss. At low particle energy most of the energy losses are due to the ionization process. At high energy radiative processes contribute.

Energy loss of electrons in diamond

Electrons lose energy due to both the ionization and radiative processes. Due to the low electron mass the radiative process contribute already at relatively low energies. In a Coulomb field of a medium nucleus the electron can emit a real photon. This photon emission is called bremsstrahlung. Thus the total energy loss is the sum of the ionization and the radiative energy losses:

$$\frac{dE}{dx} = \left(\frac{dE}{dx} \right)_{ion} + \left(\frac{dE}{dx} \right)_{rad} .$$

The mean energy loss due to ionization is given by the Bethe-Bloch formula. For electrons the ionization energy loss is

$$- \left(\frac{dE}{dx} \right)_{ion} = 2\pi N_A r_e^2 m_e c^2 \rho \frac{Z}{A} \frac{1}{\beta^2} \left[\ln \left(\frac{\tau^2(\tau+2)}{2(I/m_e)^2} \right) - F(\tau) - \delta - 2\frac{C_s}{Z} \right] ,$$

where τ is the electron kinetic energy in units of $m_e c^2$, N_A is Avogadro's number, r_e is the classical electron radius, m_e is the electron mass, ρ is the density of the material, A and Z are its atomic weight and atomic number, I is the mean excitation potential, β is the velocity of the electron in units of speed of light c , δ is the density effect correction term, C_s is the shell correction parameter and

$$F(\tau) = 1 - \beta^2 + \frac{\tau^2/8 - (2\tau + 1) \ln(2)}{(\tau + 1)^2} .$$

At non-relativistic energies the ionization energy loss has a $1/\beta^2$ energy dependence, at relativistic energies the energy loss is slightly growing. Thus the ionization energy loss has a minimum at a certain energy. A particle of

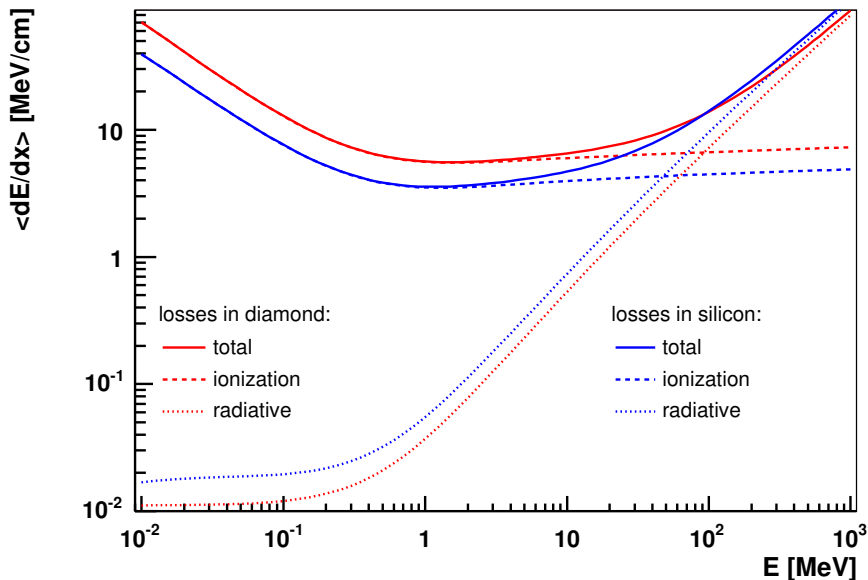


Figure 5.7: The mean energy losses of an electron in diamond (red curves) and silicon (blue curves). The solid curves show the total energy loss, the dashed ones correspond to the ionization loss and the dotted correspond to the radiative energy loss. The plot is done using the ESTAR database provided by US National Institute of Standards and Technology (www.nist.gov).

this energy is called **minimum ionizing particle (MIP)**. The MIP energy of an electron is about 1.6 MeV in diamond and about 1.3 MeV in silicon.

The energy loss due to bremsstrahlung is

$$-\left(\frac{dE}{dx}\right)_{rad} = \frac{4}{137} r_e^2 N_A \frac{Z^2}{A} m_e c^2 \tau (\ln(2(\tau + 1)) - 1/3).$$

The energy loss dE/dx for electrons in diamond and in silicon as a function of the electron energy are shown in Fig. 5.7. The radiative energy loss plays a role for electron energies larger than several MeV. The critical energy is defined as the energy at which the radiative and ionization losses of a particle are equal. The critical energies are about 90 MeV and 50 MeV in diamond and in silicon, respectively.

Fluctuations of energy losses

Since the number of inelastic collisions which initially monochromatic electrons undergo passing through a medium is a statistical value as well as the

energy loss per collision, the total energy loss fluctuates around the mean value. The energy loss distribution function is called the straggling function. In the case of a thick absorber, where the number of collisions is very high, it approaches a Gaussian. If the absorber is thin, the Central Limit Theorem does not work and the distribution can not be described with a Gaussian. The possibility of a high energy loss in a single collision plays a role and provides a tail towards large losses. Using the Landau description of the energy loss [102], the probability of the energy loss Δ for a particle passing an absorber of the thickness x can be defined as

$$f(x, \Delta) = \frac{1}{\bar{E}} \omega(\lambda) ,$$

where \bar{E} is the mean energy loss and

$$\omega(\lambda) = \frac{1}{\pi} \int_0^\infty e^{-u \ln u - \lambda u} \sin \pi u du \approx \frac{1}{\sqrt{2\pi}} \exp \left\{ -\frac{1}{2}(\lambda + e^{-\lambda}) \right\} .$$

The quantity λ is the normalized deviation from the most probable energy loss $\Delta^{m.p.}$:

$$\lambda = \frac{\Delta - \Delta^{m.p.}}{\bar{E}} .$$

5.3.2 Generation of charge carriers and Charge Collection Distance

The energy lost by a charged particle in a semiconductor excites electrons from the valence to the conduction band. The electron-hole pair creation is followed by lattice excitation (phonon excitation) and collective excitation of electrons (plasmon excitation). Thus the energy per one electron-hole creation, or ionization energy, is always higher than the band gap energy. The ionization energy for diamond is 13 eV [53].

The mean charge generated by a particle penetrating a diamond of the thickness d is

$$Q_{gen} = \frac{e\bar{E}}{W} = \frac{ed}{W} \cdot \overline{\left(\frac{dE}{dx} \right)} ,$$

where

$$\bar{E} = \int_0^d \frac{dE}{dx} dx = d \cdot \overline{\left(\frac{dE}{dx} \right)}$$

is the mean energy lost in the diamond, W is the ionization energy and e is the electron charge. The mean charge created by a MIP in diamond is 3600 electron-hole pairs per 100 μm .

If a voltage is applied to the diamond sample, the charge carriers created by an ionizing particle will drift toward the corresponding electrodes, as illustrated in Fig. 5.8.

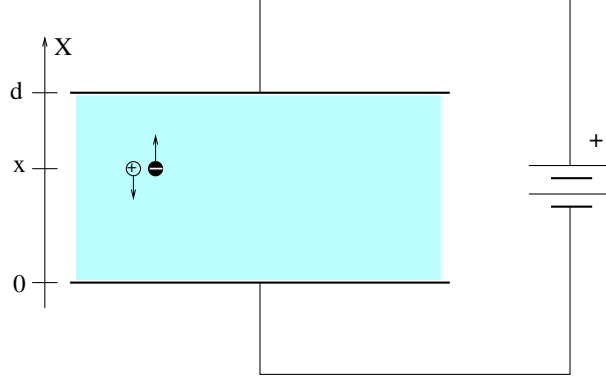


Figure 5.8: An electron-hole pair created in a diamond detector of the thickness d .

Charge Collection Distance

While a charge carrier (electron or hole) is drifting toward an electrode, a current in the circuit is induced. For parallel electrodes the current can be estimated according Ramo's theorem [103] as

$$I(t) = eF_Q v(t) = \frac{e}{d} v(t) ,$$

where $v(t)$ is the carrier drift velocity, $F_Q = 1/d$ is the weighting electric field and e is the carrier charge.

If the charge carriers can drift up to the electrode, the full charge can be measured. Assuming that carrier velocities have constant values v_e and v_h over the diamond thickness, the charge induced by one electron-hole pair (Fig. 5.8) is

$$\begin{aligned} Q_{measured} = Q_{induced} &= \frac{e}{d} \int_0^{t_e} v_e dt + \frac{-e}{d} \int_0^{t_h} v_h dt \\ &= \frac{e}{d} \left(\int_x^d dx - \int_x^0 dx \right) = e . \end{aligned}$$

The charge induced on the opposite electrode is of the same value and of opposite sign.

However, for a pCVD diamond the charge carriers have a certain probability to be trapped. If τ_e is a characteristic lifetime of an electron in the diamond, the corresponding drift length is $\delta_e = v_e \tau_e = F \mu_e \tau_e$, where F is the electric field and μ_e is the electron mobility.

If n_0 electrons are created at the moment $t = 0$ at the distance l from the positive electrode, the average number of electrons at the time t is

$$n(t) = n_0 \exp \left\{ -\frac{t}{\tau_e} \right\} .$$

Taking $x = v_e t$ the previous expression can be rewritten as

$$n(x) = n_0 \exp \left\{ -\frac{x}{\delta_e} \right\} .$$

The charge induced by the electrons is

$$Q_{e,induced} = \frac{e}{d} \int_0^{l/v_e} n(t) v_e dt = \frac{e}{d} \int_0^l n(x) dx = \frac{e}{d} n_0 \delta_e \left(1 - \exp \left\{ -\frac{l}{\delta_e} \right\} \right) .$$

If these n_0 electrons are created not at the same point but distributed over the diamond thickness d with the density $\rho_e(x)$:

$$\int_0^d \rho_e(x) dx = n_0 ,$$

the induced charge is an integral over all the electron paths $l(x) = d - x$ [97]:

$$\begin{aligned} Q_{e,induced} &= \frac{e}{d} \int_0^d \frac{\rho_e(x)}{n_0} \int_0^{l(x)/v_e} n(t) v_e dt dx \\ &= \frac{e}{d} \int_0^d \rho_e(x) \delta_e \left(1 - \exp \left\{ -\frac{d-x}{\delta_e} \right\} \right) dx . \end{aligned}$$

For small values $\delta_e \ll d$ the exponential term can be neglected. In general traps in a diamond sample might be distributed not equally and the drift length might depend on the coordinate: $\delta_e = \delta_e(x)$. The induced charge can be expressed then as

$$Q_{e,induced} \approx \frac{e}{d} \int_0^d \rho_e(x) \delta_e(x) dx .$$

If the electrons are created with a constant density $\rho_e(x) = n_0/d$, the induced charge can be written as

$$Q_{e,induced} \approx \frac{e}{d} \frac{n_0}{d} \int_0^d \delta_e(x) dx = Q_{created} \frac{\overline{\delta_e}}{d} ,$$

where $Q_{created} = n_0e$ is the total initially created charge and

$$\bar{\delta}_e = \frac{\int_0^d \delta_e dx}{d}$$

is the average electron drift length.

Under the same assumptions the charge induced by holes $Q_{h,induced}$ can be estimated. Since the density of created holes is the same as the electron density $\rho_h(x) = \rho_e(x) = n_0/d$, the total charge induced on an electrode is

$$Q_{induced} = Q_{e,induced} + Q_{h,induced} \approx Q_{created} \frac{\bar{\delta}_e + \bar{\delta}_h}{d} \equiv Q_{created} \frac{\delta_Q}{d}.$$

The value δ_Q is usually referred to as **Charge Collection Distance (CCD)** and represents the averaged drift distance between an electron and a hole before they are trapped. The CCD can also be expressed as

$$\delta_Q = F(\mu_e \bar{\tau}_e + \mu_h \bar{\tau}_h),$$

where $\bar{\tau}_e$ and $\bar{\tau}_h$ are the averaged lifetimes of electrons and holes, respectively.

Since the CCD is independent on the sample thickness it is commonly used as a diamond characteristic.

A more simple quantity, the charge collection efficiency, can be introduced as a ratio between the measured (induced on the electrode) and the created charges:

$$\varepsilon = \frac{Q_{induced}}{Q_{created}} \approx \frac{\delta_Q}{d}.$$

Chapter 6

CVD diamond measurements

As mentioned in Chapter 3, the sensors of the BeamCal will be operated under harsh radiation conditions. The response must be stable up to an absorbed dose of about 10 MGy. Diamond sensors are expected to be sufficiently radiation hard. For the diamond-tungsten option of the BeamCal relatively large area (several inch wafers) and homogeneous pCVD diamonds with a linear response are needed as sensor material.

In spite of a variety of companies and laboratories producing pCVD diamonds, only a few of them are known to produce sensors for particle detectors. Element SixTM (former De Beers)¹ is almost the only producer of detector quality pCVD diamonds in Europe. Studies of pCVD diamonds produced by Element Six are carried on by the RD42 collaboration [53] since mid of the nineties. The diamonds have an area of few cm² range and a CCD up to 300 μ m and were tested for several experiments (ATLAS, CMS at CERN, HADES at GSI). Another known manufacturer of detector quality diamonds is Norton² (a part of Saint-Gobain Abrasives, inc. since 1990). pCVD diamonds produced by Norton were also successfully tested by the RD42 collaboration [53].

Since the CVD technique was improved during the last decade, the quality of pCVD diamonds produced by other manufacturers for electronics and optics applications became comparable with the required detector quality.

The majority of diamond sensors tested within these studies were produced by the Diamond Group of Fraunhofer Institute für Angewandte Festkörperphysik (Fraunhofer IAF), Freiburg³.

The Diamond Group of the Fraunhofer IAF produces diamond wafers up to 6" diameters and several hundred micrometers of thickness for applications

¹<http://www.e6.com>

²<http://www.ind.nortonabrasives.com>

³<http://www.cvd-diamond.com>

in optics, electronics and mechanics. The special design of the microwave plasma reactors operated in the Fraunhofer IAF, mentioned in Section 5.1.2, provides a homogeneous deposition of pCVD diamond on 3" and 6" substrates. Various methods of material analysis including photoluminescence and Raman spectroscopy are used for the quality control [76].

At first stage of these studies the main goals were to check if the quality of pCVD diamonds produced by Fraunhofer IAF corresponds to the detector sensor material requirements in general and to the BeamCal requirements (Section 3.2.2) in particular.

The samples studied first have been deposited on silicon substrates and cut from 300 μm thick wafers to a size of $12 \times 12 \text{ mm}^2$. The delivered 12 samples can be divided into 4 groups, 3 samples in each. Samples of the first three groups were cut from three wafers, one for each group. The three samples of group #4 have been cut from different wafers.

Due to the differences in the pCVD diamond structure at the substrate and growth sides (Section 5.1.2), the quality of the material was expected to be much worse at the substrate side. To study the influence of the surface treatment on the diamond sensor quality, the groups of samples were treated in different ways:

Group #1:

only the substrate side was polished;

Group #2:

about 100 μm of the substrate side was removed, the growth side was polished;

Group #3:

only the growth side was polished;

Group #4:

both the substrate and growth sides were polished.

The polishing has been done with diamond nanocrystalline powder. After a following surface cleaning, the samples were metalized.

The area of the two-layer Ti/Au metalization is $10 \times 10 \text{ mm}^2$. The metal layers (10 nm of titanium and 400 nm of gold) have been evaporated on the surface without a subsequent annealing. Both the surface polishing and the metalization have been done in the Fraunhofer IAF.

The samples were put in a G10¹ frame and bonded to metal contacts. A photo of an assembled diamond sample is shown in Fig. 6.1.

¹glass fiber reinforced plastic

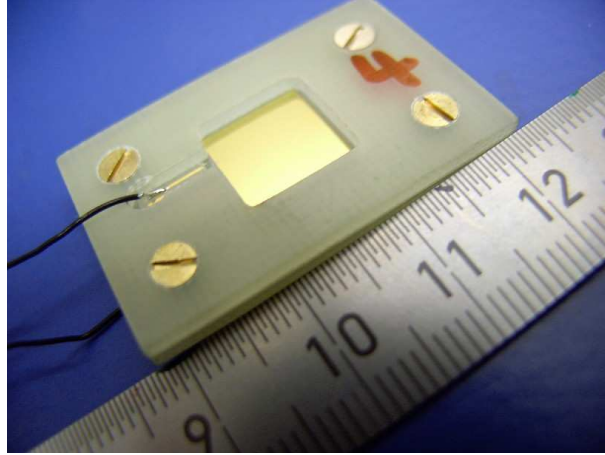


Figure 6.1: A diamond sample assembled for the test measurements.

Since for all the diamonds (except group #1) the substrate and growth sides were not distinguishable, for every sample an arbitrary side has been chosen to be a reference for a voltage polarity. For diamonds of group #1 a "normal polarity" has been defined to correspond to a positive voltage applied to the growth side.

6.1 Capacitance measurements

To check the metalization quality, a capacitance-voltage (CV) dependence was measured for every sample. Fig. 6.2 shows the principle scheme of the setup. A Hewlett-Packard LCR-meter 4263A [104] feeds the alternating current $i = i_a \cdot \sin(\omega t + \phi_i)$ through a sample (C_D, R_D) measuring the amplitude u_a and the phase shift $\delta\phi$ of the voltage drop $u = u_a(R_C, C_D, \omega) \cdot \sin(\omega t + \phi_i - \delta\phi(R_C, C_D, \omega))$ over the sample. A direct current (DC) voltage supply (a voltage source integrated to Keithley 487 picoammeter [105]) allows to apply a DC voltage to the sample. The resistors $R_C \gg (\omega C_D)^{-1}$ decouple the influence of the voltage supply from the measurement circuit. The capacitors $C_C \gg C_D$ decouple the direct current component from the LCR-meter.

The measurements were done for both polarities for voltages up to 200 V with a step of 5 V. The AC frequency was 1 kHz. The estimated accuracy of the measurements is about 10%.

For all the samples no voltage dependence has been observed within the accuracy of the measurements. The measurements results are summed in Tab. 6.1.

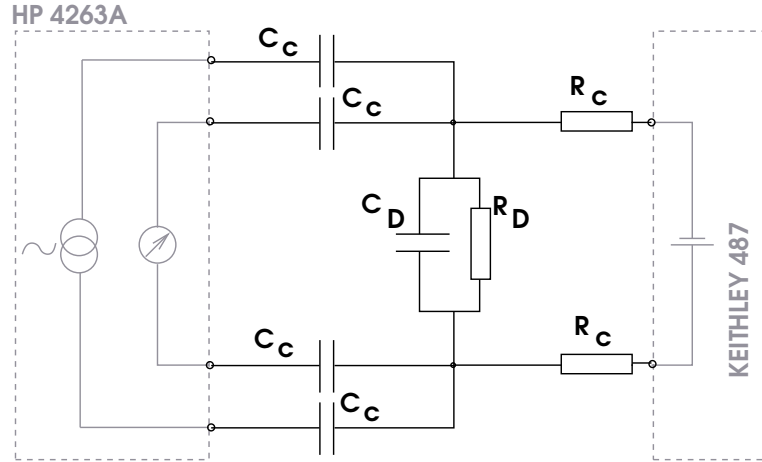


Figure 6.2: The principle scheme of the setup for the capacitance-voltage measurements. The LCR-meter feeds an alternating current through a diamond (C_D , R_D) and measures the voltage drop over the sample. A DC voltage is applied with the Keithley 487 voltage supply.

group #	1			2			3			4		
sample #	1	2	3	1	2	3	1	2	3	1	2	3
C [pF]	22	26	24	18	18	22	25	24	24	26	26	24

Table 6.1: The measured capacitance of the diamond samples.

The measured values differ from the estimated capacitance of an ideal diamond. For a sample of $300 \mu\text{m}$ thickness and the dielectric constant $\epsilon \approx 5.7$ (Table 5.1), the estimated capacitance is

$$C = \epsilon\epsilon_0 \frac{S}{d} \approx 17 \text{ pF} .$$

The difference between the measured and the estimated values of the capacitance may be caused by material properties of the diamond samples which have the non-ideal polycrystalline structure and may also have contaminations of graphite and other impurities. This also can explain the difference between diamonds of group #2 and the rest of the samples. The average dielectric constant calculated from the capacitance measurements is about 4.3 for the group #2 diamonds, whereas for the other samples the average dielectric constant is about 8.5.

6.2 Current-voltage characteristics

Measurements of the current through a diamond sample as a function of the applied voltage, here and afterwards referred to as current-voltage (IV) measurements, were done using a Keithley 487 picoammeter with an integrated voltage supply. The device has a resolution of 10 fA and supplies voltages up to 505 V. Fig. 6.3 shows the scheme of the setup. A diamond sample under the test (C_D , R_D) was placed into a light-insulating box. Since the very high diamond resistance, the current was expected to be very low, so a dry nitrogen atmosphere was kept in the box in order to minimize the leakage current over the diamond and frame surfaces. Cabling as well as the box were screened to minimize noise coupled via cabling capacitance.

The resistor r represents the cabling resistance and the internal resistance of the picoammeter. Due to the low currents, these resistances can be neglected. The capacitance of the cabling is represented by $C_{||}$. The leakage current over the G10 holding frame corresponds to a current through the resistor $R_{||}$.

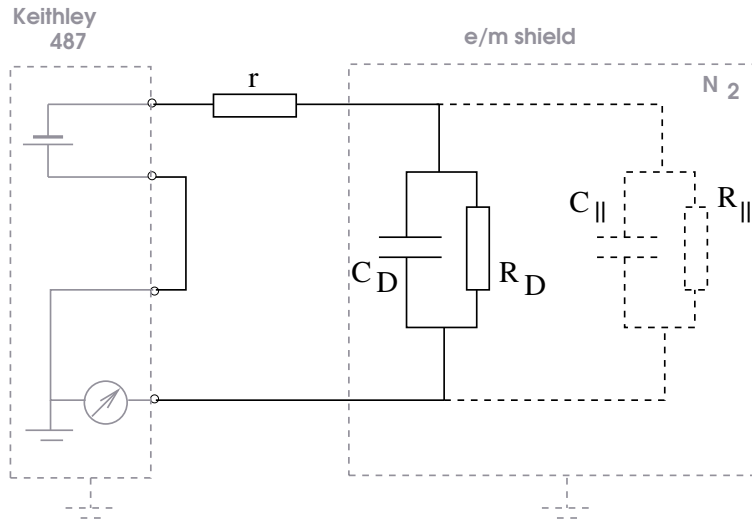


Figure 6.3: The scheme of the setup for the current-voltage measurements. A diamond sample (C_D , R_D) is placed in a light-insulating box with electromagnetic shielding and nitrogen atmosphere. The resistor r represents the cabling resistance and the internal resistances of the picoammeter. Due to the low currents, these resistances can be neglected. The capacitance of the cabling is represented by $C_{||}$. The leakage current over the G10 holding frame corresponds to a current through the resistor $R_{||}$.

The GPIB (IEEE 488) interface of the Keithley 487 picoammeter allows to perform automatic measurements. A LabView program for automatic IV-measurements has been developed. During the measurements the voltage applied can be changed by a given value and kept for a period t_{step} . The period t_{step} as well as the voltage step can be varied. For every value of the applied voltage the current is measured once per second during the full period t_{step} .

6.2.1 Open circuit measurements

Before every IV-measurement with a diamond sample, an open-circuit measurement was done to estimate the influence of the cabling and the holding frame. The measurements were done with the G10 frame, but without a diamond sample. This corresponds to the disconnected (C_D, R_D) in Fig. 6.3 and gives values for a leakage current over $R_{||}$ during the IV-measurements with a diamond.

Fig. 6.4 shows an example of the IV-dependence obtained for the open circuit. During the measurement the voltage was changed with the period $t_{step} = 300$ s from 0 V to 500 V and down to 0 V with steps of 50 V. The average values of the current measured after the voltage stabilization are shown. The leakage current and the zero drift of the picoammeter did not exceed 50 fA.

6.2.2 Settling current

To choose a proper time regime for the current-voltage measurements, the settling current caused by a voltage turn was studied. The measurements of the settling current were done during $6 \cdot 10^3$ s after the voltage of 300 V was applied. From a simple consideration of the circuit shown in Fig. 6.3, the expected time constant $\tau \approx rC_D$ is in the nanosecond range. However, the current measured as a function of the time has a different behavior. Fig. 6.5 shows the settling current for several samples. The measured current does not depend on the time exponentially. It has a very pronounced tail up to several thousands of seconds and varies for different samples.

The obtained dependence can be fitted with a power-law function

$$i(t) = I_0 + const \cdot t^{-(1-\alpha)},$$

where $0 < \alpha < 1$. Fig. 6.6 shows the current of one of the samples measured as a function of the time after the voltage of 300 V has been applied. The current is fitted to the power-law function for $t > 300$ s.

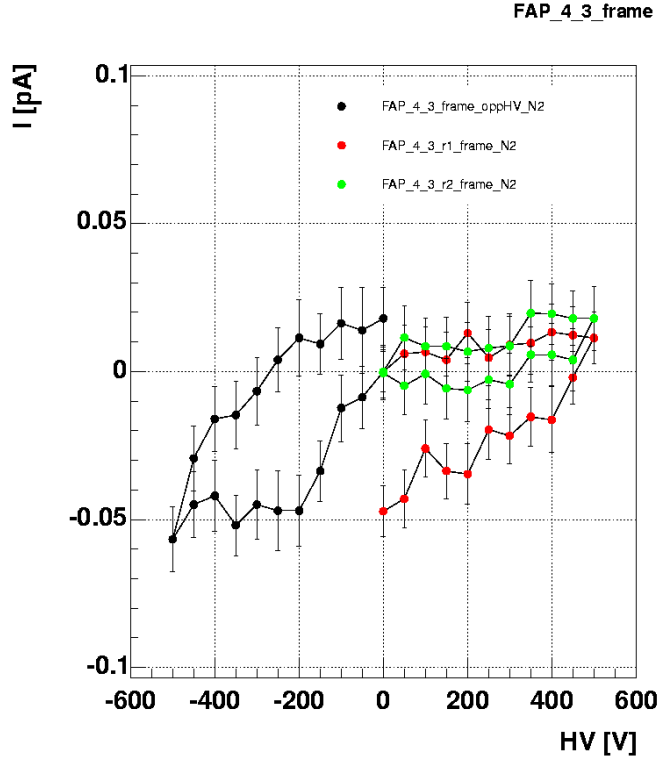


Figure 6.4: Open circuit current-voltage dependences. The measurements are done with the G10 frame, but without a diamond sample. Different colors represent different measurements. For every measurement the voltage was changed from 0 V to ± 500 V and back to 0 V.

The power-law function is often used to describe a photoinduced current in amorphous semiconductors [106, 107, 108], when the carrier transport is defined by variable range hopping² over localized states.

The model proposed in [106] considers a propagation of a packet of charge carriers generated near the electrode of a planar capacitor through the bulk of thickness L . During the drift, the carriers undergo trapping and de-trapping with certain probabilities. Thus the width of the packet σ increases with time. The mean position of a carrier in the packet is shown to be

$$\langle l \rangle \propto t^\alpha, 0 < \alpha < 1,$$

while $\langle l \rangle / \sigma = \text{const.}$ The current associated with such a moving packet

²The variable range hopping is discussed in Section 5.2.1

is

$$i(t) \propto \begin{cases} t^{-(1-\alpha)}, & \langle l \rangle \ll L \\ t^{-(1+\alpha)}, & \langle l \rangle \approx L. \end{cases}$$

However, the model can not be entirely applied to the settling current of the diamond samples because it considers the charge carriers to be initially liberated due to photoexcitation. The transition from $i(t) \propto t^{-(1-\alpha)}$ to $i(t) \propto t^{-(1+\alpha)}$ was not observed for the measured diamond. However, the long settling time may point to the presence of shallow states or band tails.

As another reason for the long settling process, a non-uniform distribution of charge traps can be considered. The probability of detrapping $f_{DT} \propto \exp\{-\Delta E/kT\}$ decreases exponentially with the ionization energy ΔE . Thus, if the traps are deep enough, the detrapping probability is very low. If the traps are distributed non-equally in the diamond bulk, what is likely the case for polycrystalline material, a local space charge might be created as described in Section 5.2.1. The time needed for the stabilization of the resulting electric field in the diamond bulk will depend on a ratio of the trapping and detrapping frequencies.

6.2.3 Current-voltage measurements

Because of the long tail of the settling current, measurements of a stabilized current as a function of the voltage applied can not be performed in a reasonable time. To obtain IV-characteristics for the comparison of sensors, the following time regime was chosen. During the IV-measurements the voltage was changed every 300 s with a step of 50 V. The current was monitored all the time, however, only the values measured during the last 60 s were averaged. After the measurements at 500 V, the voltage was decreased down to zero with the same step and timing. As seen from Fig. 6.6, the chosen regime was a compromise between a reasonable time of the measurements and reliable estimated values. The obtained values give an upper limit of the current.

An example of the obtained dependences is shown in Fig. 6.7. For both polarities, the higher in absolute value current corresponds to the rising voltage; the curves of lower current were obtained for the decreasing voltage. Such a behavior results from the measurements of a not completely settled current.

The results are reproducible if the measurement regime is kept. Four different measurements, two for every polarity, shown in Fig. 6.7 are done on different days.

The IV-dependences obtained for all sensors can be divided into two groups. The first group has symmetric currents for positive and negative

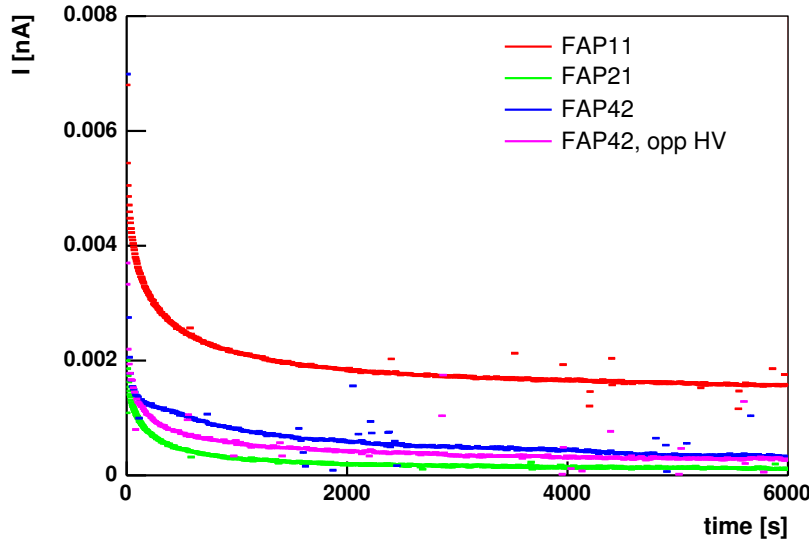


Figure 6.5: Settling currents after the voltage of 300 V is applied. The blue and magenta curves show the current for the same diamond but opposite polarities of the applied voltage.

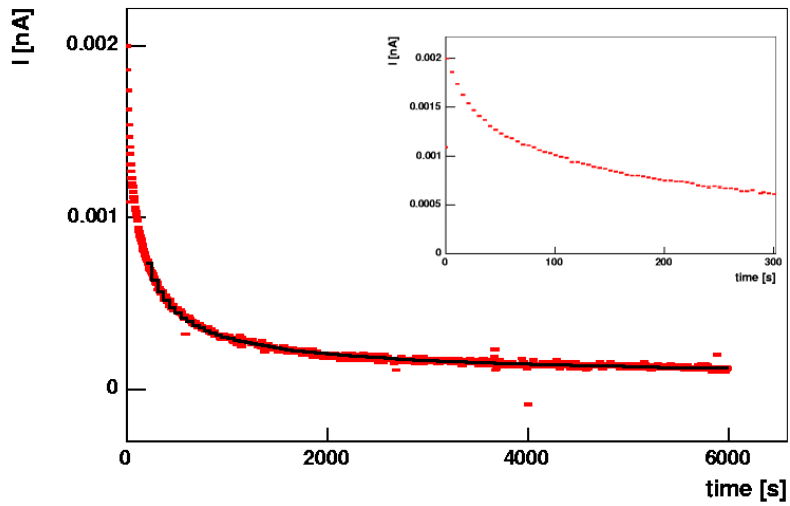


Figure 6.6: The settling current as a function of the time measured for one of the samples. The current is fitted to $i(t) = I_0 + const \cdot t^{-(1-\alpha)}$ for time $t > 300$ s (black curve). The zoomed plot in the top right corner shows the current measured during the first 300 s.

polarities. Within the operated voltages, corresponding to an electric field up to $1.7 \text{ V}/\mu\text{m}$, the IV-dependences are close to linear. This corresponds to ohmic behavior. Fig. 6.7 shows an example of such IV-dependence.

Another kind of the IV-dependence is shown in Fig. 6.8. The current increases nonlinearly with the voltage at the explored voltage range and an asymmetry of the current for different polarities is seen. A much higher current is measured above a certain voltage, however, the current is still in a nanoampere range.

Table 6.2 summarizes the measurement results for all samples of groups #1-4. Most of the sensors show a low current linearly rising with the voltage. Diamond samples which have a non-linear or/and asymmetric current-voltage dependence are marked with a red bold font. It is seen, that such diamonds are present in all groups.

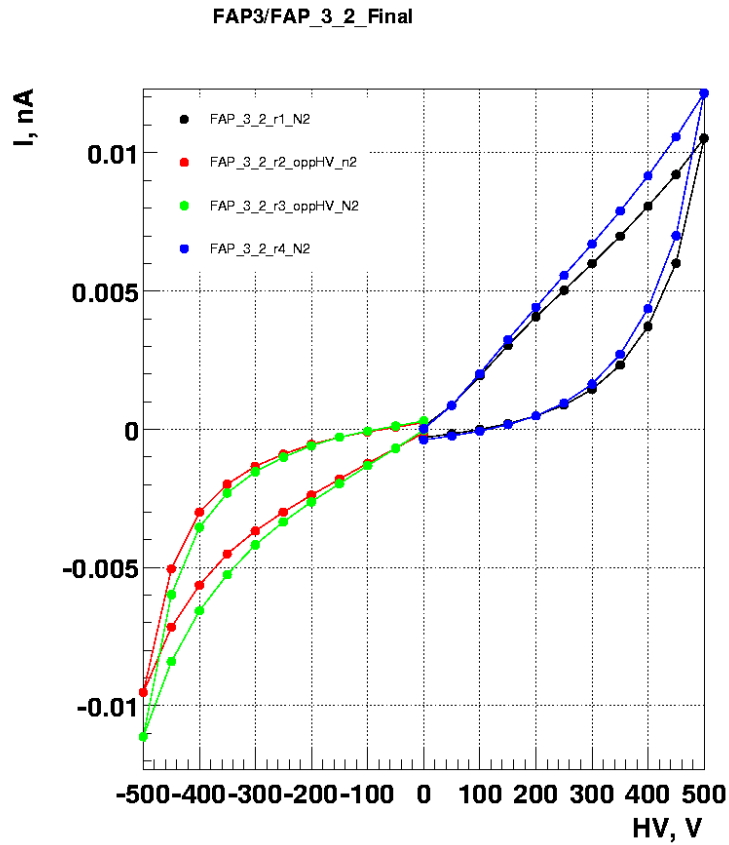


Figure 6.7: An example of the IV-dependence. Each color represents one measurement. The values of current at a certain voltage are obtained by averaging the current measured in 220s after the voltage was applied. The hysteresis corresponds to the different values of current measured for the rising and decreasing voltages. Such a behavior is caused by the long settling process.

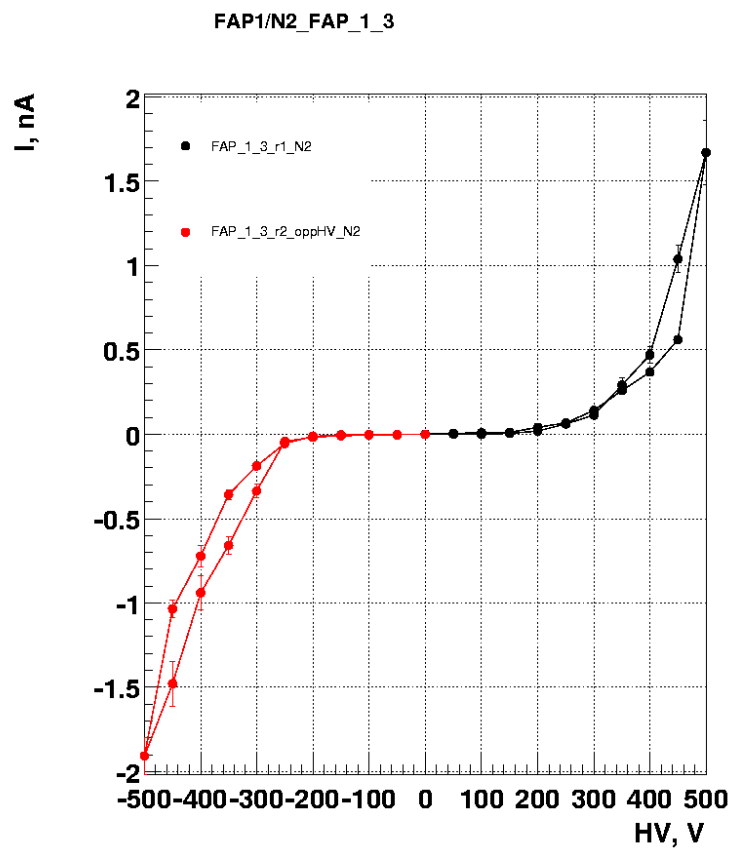


Figure 6.8: An example of the non-ohmic IV-dependence.

sample #	$\mathbf{R} [\Omega]$			$F \approx -1.7 \text{ V} / \mu\text{m}$
	$F = +1 \text{ V} / \mu\text{m}$	$F = -1 \text{ V} / \mu\text{m}$	$F \approx +1.7 \text{ V} / \mu\text{m}$	
1.1	$(3.15 \pm 0.05) \cdot 10^{13}$	$(6.34 \pm 0.06) \cdot 10^{13}$	$(3.71 \pm 0.14) \cdot 10^{13}$	$(6.01 \pm 0.09) \cdot 10^{13}$
1.2	$(3.63 \pm 0.07) \cdot 10^{14}$	$(3.73 \pm 0.07) \cdot 10^{14}$	$(3.59 \pm 0.05) \cdot 10^{14}$	$(3.59 \pm 0.50) \cdot 10^{14}$
1.3	$(2.13 \pm 0.18) \cdot 10^{12}$	$(8.94 \pm 1.04) \cdot 10^{11}$	$(2.99 \pm 0.35) \cdot 10^{11}$	$(2.62 \pm 0.15) \cdot 10^{11}$
2.1	$(5.08 \pm 0.18) \cdot 10^{14}$	$(8.17 \pm 0.38) \cdot 10^{14}$	$(6.12 \pm 0.16) \cdot 10^{14}$	$(9.59 \pm 1.49) \cdot 10^{14}$
2.2	$(1.04 \pm 0.06) \cdot 10^{15}$	$(1.18 \pm 0.09) \cdot 10^{15}$	$(1.25 \pm 0.05) \cdot 10^{15}$	$(1.28 \pm 0.07) \cdot 10^{15}$
2.3	$(1.08 \pm 0.08) \cdot 10^{15}$	$(1.02 \pm 0.57) \cdot 10^{15}$	$(7.40 \pm 0.21) \cdot 10^{14}$	$(1.81 \pm 0.64) \cdot 10^{14}$
3.1	$(3.25 \pm 0.22) \cdot 10^{12}$	$(8.92 \pm 0.24) \cdot 10^{10}$	$(2.04 \pm 0.18) \cdot 10^{10}$	$(4.10 \pm 0.12) \cdot 10^8$
3.2	$(4.49 \pm 0.07) \cdot 10^{13}$	$(7.21 \pm 0.11) \cdot 10^{13}$	$(4.12 \pm 0.06) \cdot 10^{13}$	$(4.51 \pm 0.07) \cdot 10^{13}$
3.3	$(1.26 \pm 0.03) \cdot 10^{14}$	$(9.42 \pm 0.20) \cdot 10^{13}$	$(3.71 \pm 0.19) \cdot 10^{12}$	$(3.58 \pm 0.12) \cdot 10^{13}$
4.1	$(3.31 \pm 0.13) \cdot 10^{12}$	$(1.93 \pm 0.03) \cdot 10^{12}$	$(4.31 \pm 0.17) \cdot 10^{10}$	$(6.63 \pm 0.21) \cdot 10^8$
4.2	$(5.79 \pm 0.18) \cdot 10^{14}$	$(3.28 \pm 0.08) \cdot 10^{14}$	$(4.42 \pm 0.47) \cdot 10^{14}$	$(3.16 \pm 0.04) \cdot 10^{14}$
4.3	$(4.86 \pm 0.09) \cdot 10^{13}$	$(6.90 \pm 0.12) \cdot 10^{13}$	$(4.27 \pm 0.07) \cdot 10^{13}$	$(5.22 \pm 0.08) \cdot 10^{13}$

Table 6.2: Diamond resistance calculated from the measured current. The values are given for the electric fields strength of $F = \pm 1 \text{ V} / \mu\text{m}$ and $F \approx \pm 1.7 \text{ V} / \mu\text{m}$ for the $300 \mu\text{m}$ thick diamonds and $\pm 1.75 \text{ V} / \mu\text{m}$ in the case of the $200 \mu\text{m}$ diamonds). Diamond samples which have a non-ohmic current-voltage dependence are marked with a red bold font.

6.3 Measurements of the Charge Collection Distance

As mentioned in Section 5.3.2, the charge collection efficiency of a pCVD diamond ε is usually less than 100% due to a certain amount of charge traps. The averaged drift distance between an electron and a hole before they are trapped, the charge collection distance $\delta_Q \approx \varepsilon \cdot d$, is commonly used as a characteristic of the diamond charge collection efficiency since it does not depend on the thickness d of a diamond sample. As shown in Section 5.3.2, this simple interpretation of the CCD is derived for $\delta_Q \ll d$. However, in most practical cases this condition is satisfied.

Measurements of the CCD are done with minimum ionizing particles (MIPs). The charge created by a MIP in diamond is $Q_{created} = 36 e^-h/\mu\text{m}$ (Table 5.1). The CCD can be determined from the charge induced on the electrodes:

$$\delta_Q \approx \frac{Q_{induced}}{Q_{created}} \cdot d.$$

For a MIP traversing a diamond the CCD is calculated as

$$\delta_Q = \frac{Q_{induced}}{36 e^-/\mu\text{m}}.$$

6.3.1 Set Up for the CCD measurements

The set up for the CCD measurements is shown in Fig. 6.9. The signal created in the diamond sample by an electron from a ^{90}Sr source is read out with a charge-sensitive preamplifier. The digitization of the amplified signal is done with an integrating ADC. A $5 \times 5 \text{ mm}^2$ plastic scintillator is used to provide a trigger. The scintillator is read out with two photomultiplier tubes (PMTs) via wavelength shifting fibers. A coincidence of discriminated PMT signals provides a gate signal for the ADC.

During the measurements a diamond sample together with the preamplifier is placed in a shielded light-tight box. The box has windows made from thin metalized mylar to reduce the material density for the penetrating electrons. The ^{90}Sr source is collimated by means of a 4 mm long brass collimator with a diameter of 5 mm. The distance between the source and the diamond is 25 mm and between the diamond and the scintillator is 12 mm.

An ISEG SHQ 222M high voltage source [109] is used to apply the voltage to the diamond sample.

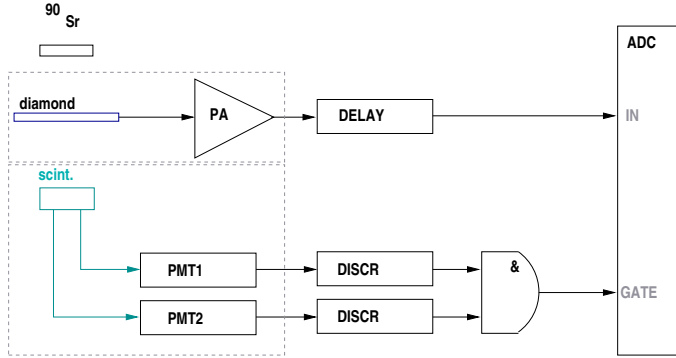
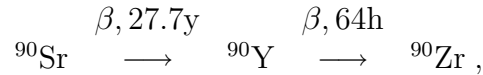


Figure 6.9: The set up for the CCD measurements. The signal from the diamond generated due the crossing of an electron from the ^{90}Sr source is read out with a charge-sensitive preamplifier (PA). The triggering scintillator is read out with two photomultiplier tubes (PMTs) via wavelength shifting fibers. The discriminated signals from the PMTs are fed into a coincidence unit. In the case of the coincidence, a gate signal for the ADC is generated.

Simulation of energy deposition in a diamond sample

Simulation studies were done in order to optimize the set up. Energy deposition in the diamond and scintillator caused by electrons from a ^{90}Sr source were simulated using GEANT4. The collimator and the mylar windows below and above the diamond were taken into account. The ^{90}Sr and the diamond are centered in the (x, y) plane, the diamond area has a square shape $-5 \text{ mm} < x < 5 \text{ mm}$, $-5 \text{ mm} < y < 5 \text{ mm}$.

Electrons from a ^{90}Sr source have a continuous spectrum originated from two successive beta-decays [110],

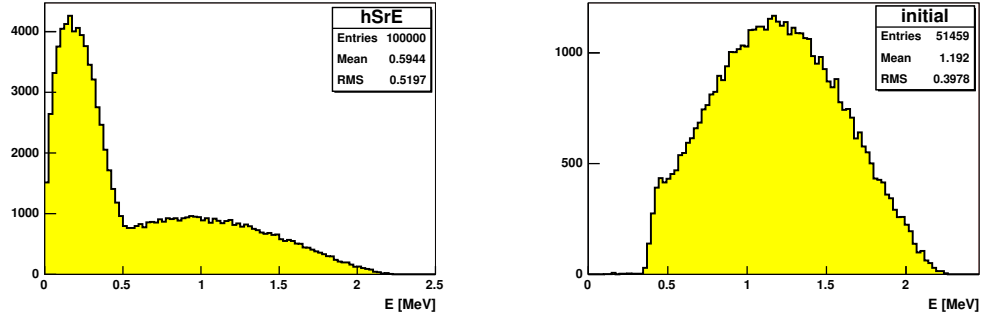


with the maximum energy of 0.55 and 2.27 MeV of ^{90}Sr and ^{90}Y electrons, respectively. The beta spectra were generated using the probability density, which can be derived from kinematics:

$$\frac{dN(\epsilon)}{d\epsilon} \propto \epsilon \sqrt{\epsilon^2 - 1} (\epsilon_{max} - \epsilon)^2 ,$$

where ϵ and ϵ_{max} are the electron energy and the maximum energy of the spectrum in units of $m_e c^2$. The generated spectrum of electrons emitted from a ^{90}Sr source is shown in Fig. 6.10 (a).

However, most of the electrons do not reach the scintillator due to absorption and scattering in the diamond and the mylar foils. Only electrons



a)

b)

Figure 6.10: The generated spectrum of electrons emitted from a ^{90}Sr source (a). The initial energy distribution of the electrons from the ^{90}Sr source which produce a triggered signal in a $300\ \mu\text{m}$ thick diamond (b). The scintillator efficiency is assumed to be 100%. No discriminator threshold for a scintillator signal was considered.

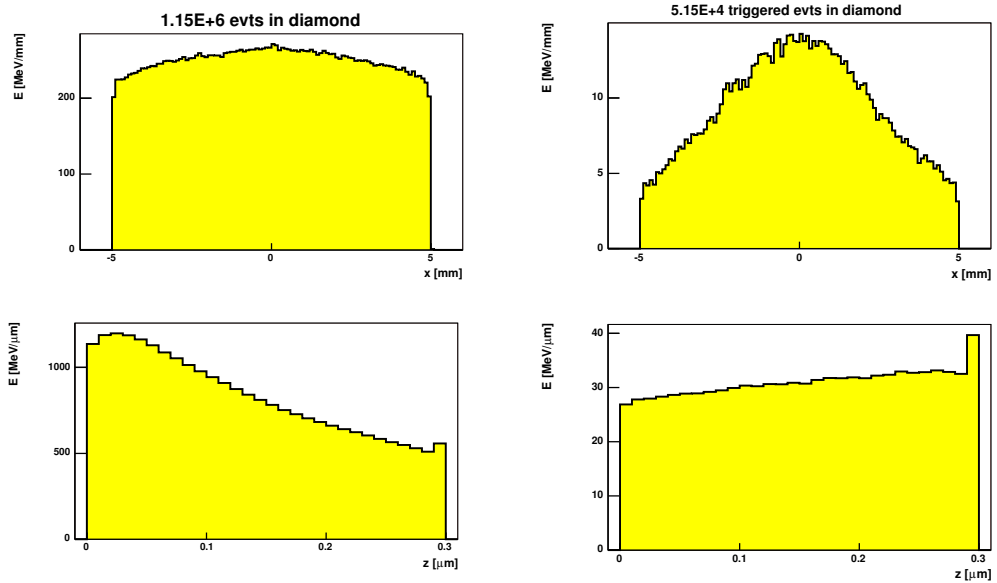


Figure 6.11: The simulated energy deposition in a $300\ \mu\text{m}$ thick diamond. The deposition distribution over the diamond area (x, y) , projected onto the x -axis (top) and depth (bottom *) are shown for all electrons (left) and for the triggered electrons only (right). The scintillator efficiency is assumed to be 100%; no discrimination of the scintillator signal was considered.

*: The high energy deposition in the last micrometers of the diamond depth is caused by GENT4 features of ionization process in very thin material layers.

with a relatively high energy are able to produce a triggering signal in the scintillator. The energy distribution of the electrons which deposit energy in both a $300\ \mu\text{m}$ thick diamond and in the scintillator is shown in Fig. 6.10 (b). The mean value of $1.2\ \text{MeV}$ is close to the MIP energy.

Fig. 6.11 shows spatial distributions of the energy deposited in the diamond for all electrons from the ^{90}Sr source (left) and for the triggered electrons (right). As seen from the left top histogram of the figure, the irradiation is almost homogeneous over the diamond area (x, y) . Due to the small size of the scintillator the triggered signals are produced mostly in the central part of the diamond (right top histogram).

The bottom histograms show the depth distribution of the deposited energy. The energy deposition is almost homogeneous for the triggered signals, and hence the CCD measured with such a set up is averaged over the depth.

Fig. 6.12 shows the spectrum of the energy deposited in the diamond in the case of triggered events. The Landau distribution (Section 5.3.1) describes well the shape of the spectrum.

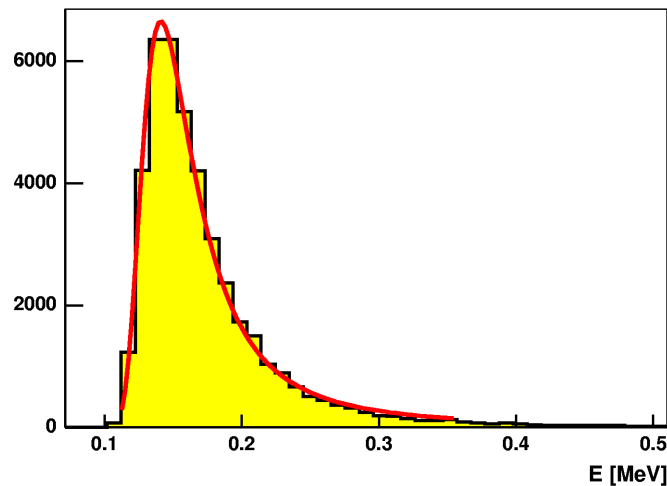


Figure 6.12: The spectrum of energy deposited in the diamond in the case of triggered events fitted to the Landau distribution.

Preamplifier

The CCD of the diamond samples was expected to be in the order of $100\ \mu\text{m}$. Thus the signal produced by a MIP was estimated to be very small, $Q_{\text{induced}} \approx 3600\ e^-$.

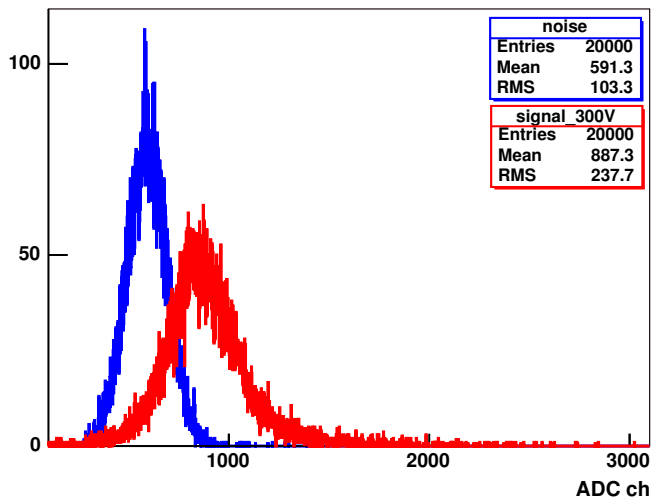


Figure 6.13: A signal spectrum (red) in comparison to a noise one (blue).

A low-noise charge-sensitive preamplifier VV50-3 [111] was used for the measurements. Later it was replaced with an AMPTEK A250 [112] low-noise charge-sensitive preamplifier. In both cases a shaping time of 20 ns gave the equivalent noise charge (ENC) of about $700 e^-$ for 20 pF of load capacitance.

The amplified signals were digitized with a CAEN V265 charge-integrating ADC [113]. Fig. 6.13 shows a signal spectrum (red) in comparison to a noise one (blue). The signal spectrum is obtained with the applied voltage U corresponding to an electric field of $F = U/d = 1 \text{ V}/\mu\text{m}$, where d is the diamond thickness. The mean value of the spectrum corresponds to an integrated charge of about $2000 e^-$ or to a CCD of $60 \mu\text{m}$. The fluctuations of energy loss in the diamond estimated from the simulation results, Fig. 6.12, correspond to about $200 e^-$.

The width, σ , of the signal spectrum, estimated from Fig. 6.13, is about $1200 e^-$. The width is defined by the fluctuations of the energy loss, $\sigma_{dE/dx} \approx 200 e^-$, by the fluctuations of the carrier drift length, σ_{drift} , and by the electronic noise, $ENC \approx 700 e^-$:

$$\sigma^2 = \sigma_{dE/dx}^2 + \sigma_{drift}^2 + ENC^2 .$$

The value of σ_{drift} , estimated from the above equation, is about $950 e^-$. Thus the width of the signal spectrum is given mostly by the fluctuations of the carrier drift length and by the relatively high electronics noise. Hence, the signal spectrum can be well described with a Gaussian distribution.

6.3.2 Measurement results

The CCD as a function of the electric field in a diamond sensor was measured for each sample.

Since the current-voltage measurements have shown the long settling processes after the voltage change (Section 6.2.2), all CCD measurements were also done in the same time regime to provide comparable results.

The voltage was applied to a sample with steps of 50 V. The spectrum measurements were started in 2 min after the voltage has been set. The total time needed for one measurement was about 15 min.

Fig. 6.14 shows the measurement results for one of the diamonds. The CCD grows with the electric field. The slope becomes smaller with the field strength, but no plateau was observed up to 1.5 V/ μm .

Table 6.3 sums up the results of the CCD measurements. Diamonds with a non-ohmic current-voltage dependence are marked with a red bold font (as in Table 6.2). No correlation between the CCD values and the current-voltage characteristics has been observed.

6.4 Measurements of the Charge Collection Distance as a function of the absorbed dose.

The stability of the pCVD diamond response under electromagnetic radiation is especially important for the calorimeter application. To explore the stability of the diamond response, the CCD was measured under sustained irradiation as a function of the absorbed dose.

The irradiation studies were carried out using the set up described in Section 6.3. The high activity of the ^{90}Sr (about 100 MBq at the time of the studies) allowed to use the source for irradiation as well as for the spectrum measurements. During the irradiation the voltage applied corresponded to an electric field of 1 V/ μm . The current in the high voltage circuit was monitored using the ISEG voltage source.

6.4.1 Estimation of the absorbed dose rate

The rate of the absorbed dose, dD/dt , is proportional to the mean energy \bar{E} deposited in the detector by an electron:

$$\frac{dD}{dt} = \frac{\bar{E}A}{m},$$

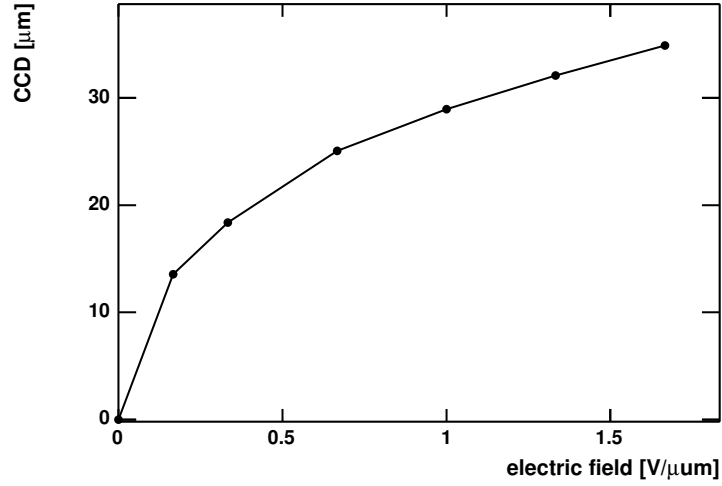


Figure 6.14: An example of the CCD measured as a function of the electric field.

sample #	CCD [μm]	
	$F = +1 \text{ V}/\mu\text{m}$	$F = -1 \text{ V}/\mu\text{m}$
1.1	31	29
1.2	21	29
1.3	16	20
2.1	12	18
2.2	5	6
2.3	6	6
3.1	29	27
3.2	49	46
3.3	47	45
4.1	41	41
4.2		
4.3	60	52

Table 6.3: The CCD measured for the diamond samples. The values measured at the applied voltage corresponding to the electric field $F = \pm 1 \text{ V}/\mu\text{m}$ are shown. Diamond samples with a non-ohmic current-voltage dependence are marked with a red bold font (as in Table 6.2).

where A is the electron flux through the detector surface and m is the mass of the detector. If the charge collection efficiency is 100%, the dose rate can be estimated from the current I_i caused by the irradiation:

$$I_i = \frac{\bar{E}A}{E_{eh}} e,$$

where E_{eh} is the energy to create one electron-hole pair and e is the electron charge. However, for pCVD diamond sensors the charge collection efficiency is less than 100% and may depend on the absorbed dose. Thus a reference detector for the dose rate estimation was used. The dose rate was measured using a $5 \times 5 \text{ mm}^2$ silicon pad detector. The thickness of the detector was $280 \mu\text{m}$. The energy to create one electron-hole pair in silicon is 3.6 eV , the charge collection efficiency is 100%. Measurements of the current caused in the silicon sensor by the irradiation were done for different distances r between the source and the detector. The dose rate was estimated from the measured current as

$$\frac{dD(r)}{dt} = \frac{E_{eh}}{em} I_i(r).$$

To derive the dose rate for a diamond sensor from the dose rate measured for the silicon pad, the assumption of a homogeneous irradiation was made. Then the electron flux at a fixed distance d between the source and the detector is proportional to the detector area and

$$\left(\frac{dD}{dt}\right)_{diam} = \frac{\bar{E}_{diam} A_{diam}}{m_{diam}} = \left(\frac{dD}{dt}\right)_{Si} \frac{\bar{E}_{diam}}{\bar{E}_{Si}} \frac{\rho_{Si}}{\rho_{diam}} \frac{d_{Si}}{d_{diam}},$$

where ρ is the mass density and d is the detector thickness. The ratio of the mean deposited energy for diamond and silicon is taken from the simulations,

$$\frac{\bar{E}_{diam}}{\bar{E}_{Si}} = 1.54.$$

The resulting calibration curve is shown in Fig. 6.15. The dose rate estimated for a $300 \mu\text{m}$ thick diamond is shown as a function of the distance between the source and the diamond. A $1/r^2$ dependence of the electron flux A is expected, so the estimated absorbed dose rate is fitted as

$$\frac{dD(d)}{dt} \propto \frac{p_0}{r^2}.$$

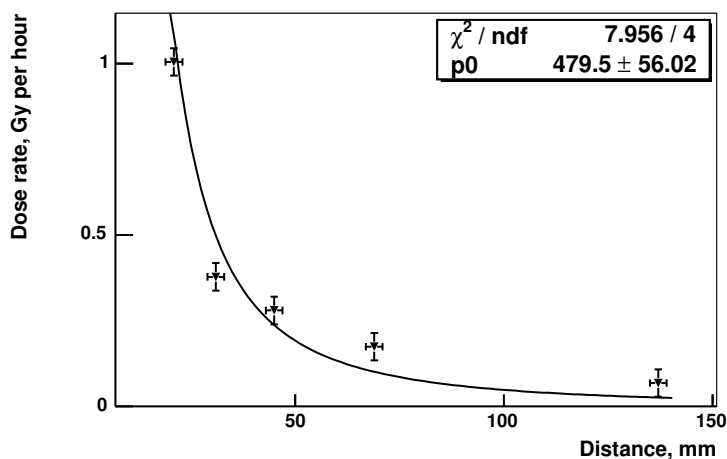


Figure 6.15: The dose rate estimated for a 300 μm thick diamond as a function of the distance between the source and the diamond.

6.4.2 Measurement results

The dependence of the CCD as a function of the absorbed dose was measured for all diamond samples. During the measurements the signal width and the current in the high voltage circuit were monitored.

Fig. 6.16 and 6.17 show the results for all four groups of diamonds. Groups #1 and #2 are shown, respectively, in Fig. 6.16 (a) and Fig. 6.16 (b), groups #3 and #4 - in Fig. 6.17 (a) and Fig. 6.17 (b). For every group the CCD (top), the width of the signal peak (mid) and the current (bottom) are shown as functions of the absorbed dose. All diamonds within a group show similar behavior, except the diamonds of group #4.

For diamond samples of groups #1 and #2 the CCD was growing with the dose up to a stable value. The increased CCD results in a larger mean value and larger width of the signal peak. The current is stable in the case of group #2, a slight growth of the current has been observed for group #1.

A CCD increase at low irradiation doses has been reported by many authors [59, 79, 97]. The observed CCD growth under low dose irradiation is explained in the following way. Due to carrier traps in a pCVD diamond the charge carriers created by a transversing ionizing particle have a high probability to be trapped. If some of traps are deep, i.e. have a high ionization

energy ΔE , than the probability of detrapping is very low:

$$f_{DT} \propto \exp\{-\Delta E/kT\}$$

and a passivation of the deep traps will occur. Due to the lower concentration of the active charge traps, the CCD increases. The effect is referred to as "priming" or "pumping".

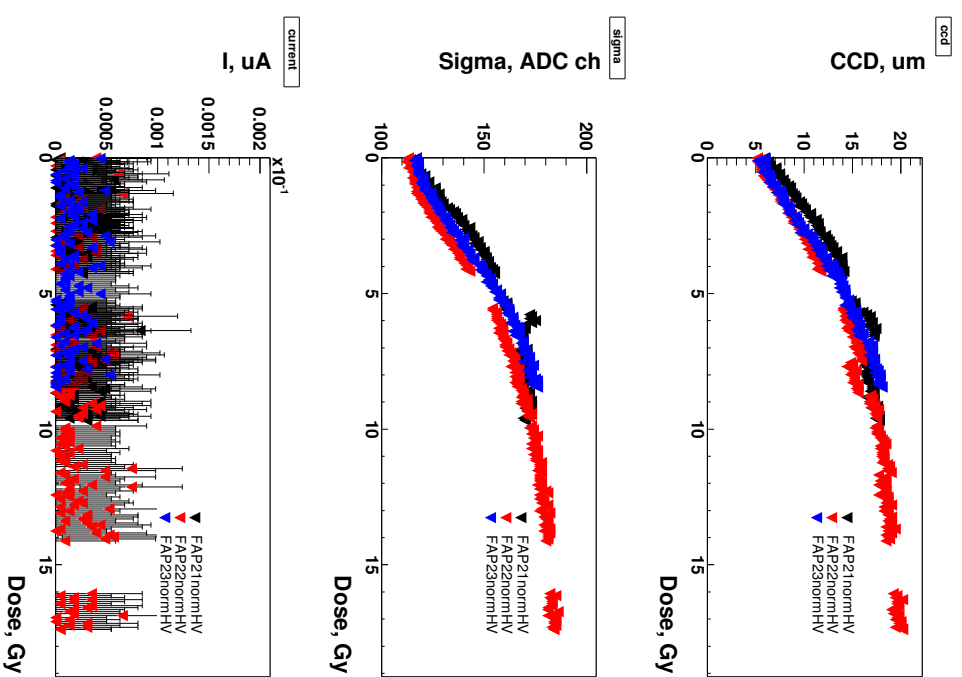
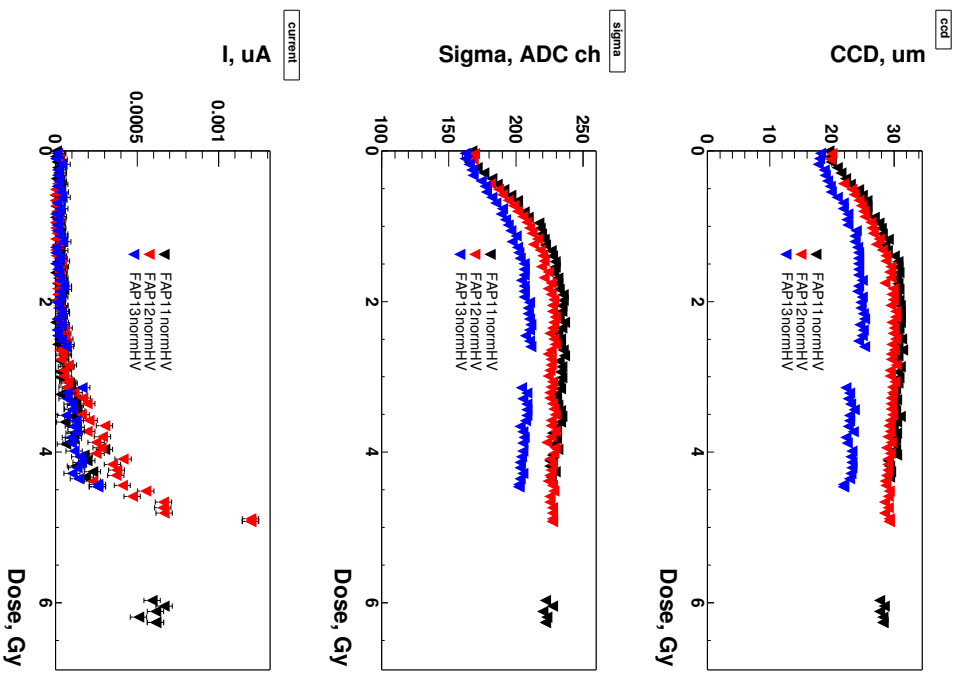
Group #3 showed different behavior. The CCD was decreasing with the absorbed dose. In addition, the current in the high voltage circuit increased strongly causing noise and the corresponding broadening of the signal peak. Already after about 7 Gy of the absorbed dose the measurements of the CCD became impossible due to the extremely high noise level.

Group #4 obviously consisted of diamonds of different quality. Both types of behavior have been observed. One of the samples has the CCD increasing with the absorbed dose, another one loses the detection capability already at the dose of about 3 Gy. The third sample (4.3) showed a slight decrease in the CCD without the dramatical current growth.

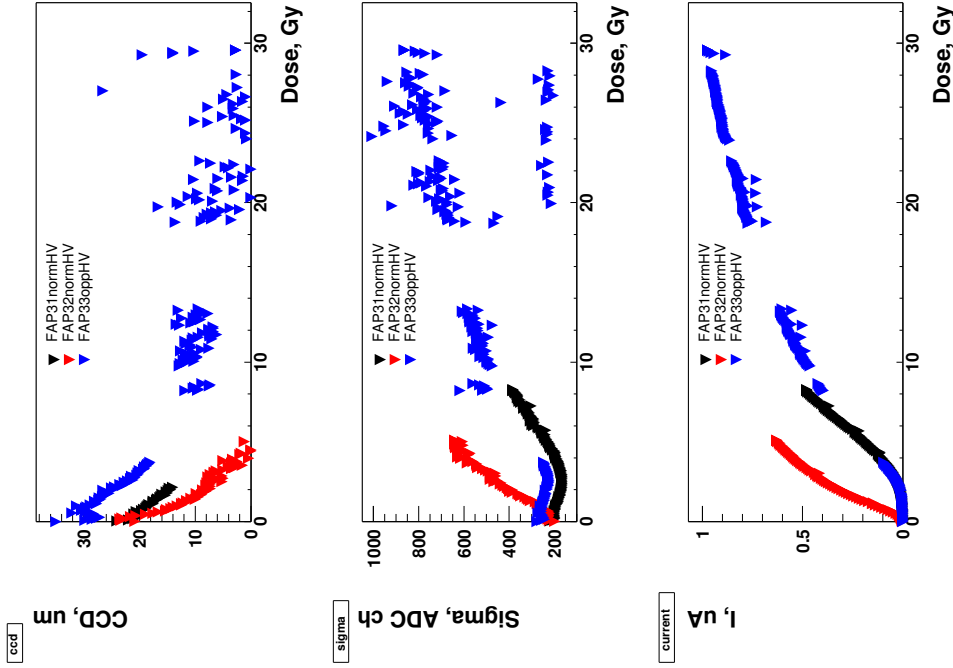
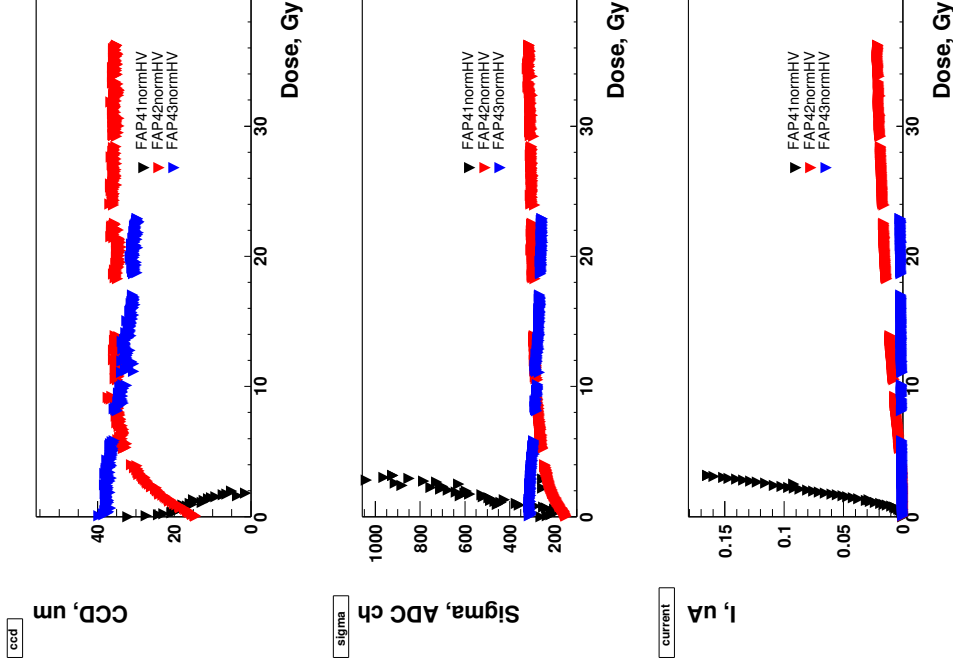
Fig. 6.18 shows that the broadening of the signal peak obtained during the irradiation of diamonds from groups #1 and 2 is of different nature than the corresponding effect obtained with diamonds from group #3. The width of the signal peak is plot together with the width of a testpulse peak measured during the irradiation. For the testpulse measurements the irradiation was interrupted and a charge of a certain value was injected to the preamplifier via a capacitor. The testpulse measurements were done with a connected diamond.

Fig. 6.18 (a) shows the broadening of the signal peak monitored during irradiation of diamond 1.2. Since the testpulse peak was stable, this broadening can be explained as increased fluctuations of the induced charge.

Group #3 has the opposite behavior (Fig. 6.18 (b)). The width of the testpulse peak was not stable during the irradiation, it increases together with the width of the signal peak. Thus, the broadening of the signal peak corresponds to the increased noise. A combination of these two effects has been observed for two diamonds of group #4 as shown in Fig. 6.18 (c).



a) Figure 6.16: The CCD (top), the width of a signal peak (mid) and the current (bottom) as functions of the absorbed dose are shown for diamonds of group #1 (a) and #2 (b).



a) b)

Figure 6.17: The CCD (top), the width of a signal peak (mid) and the current (bottom) as functions of the absorbed dose are shown for diamonds of group #3 (a) and #4 (b).

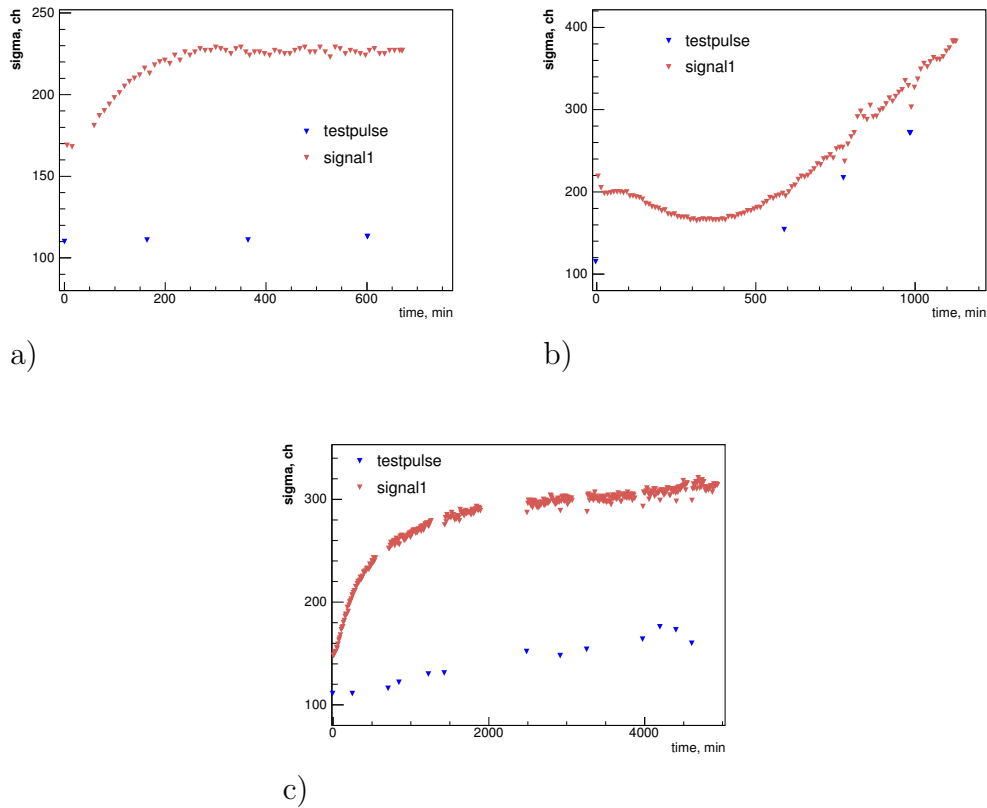


Figure 6.18: The width of signal and testpulse peaks as a function of the irradiation time observed for sample 1.2 (a), 3.1 (b) and 4.2 (c).

6.5 Further studies

6.5.1 Group #3 - influence of the substrate side treatment

The unstable behavior of group #3 samples under the irradiation might be caused either by the unpolished substrate side, where the material quality is known to be low, or by a poor quality of the whole wafer.

To distinguish between the influence of the substrate side material and general quality of the wafer, one of the diamonds from group #3 was sent back to the manufacturer for a further treatment. About $60\ \mu\text{m}$ of the sample has been polished away from the substrate side of the sample.

The measurements of the CCD as a function of the absorbed dose were repeated with the modified sample under the standard condition. Fig. 6.19

shows the CCD and the current in the high voltage circuit as functions of the absorbed dose measured for the diamond sample before and after the treatment of the substrate side. As can be seen, the polishing did not improve the quality of the sensor. Thus, the properties of group #3 are defined by the material quality of the initial wafer. The deterioration of the sample properties after the polishing points to a possible influence of the surface treatment procedure on the sensor quality.

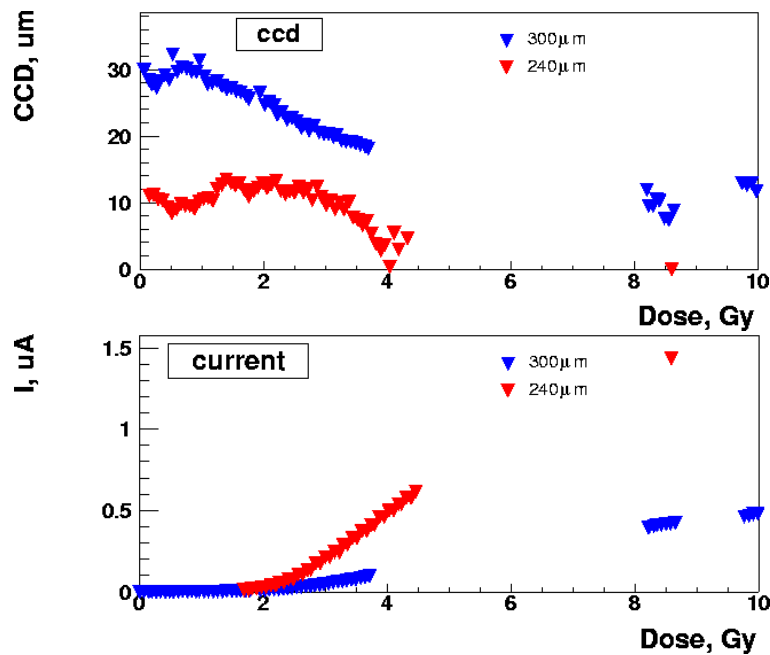


Figure 6.19: The charge collection distance (top) and the current (bottom) as functions of the absorbed dose measured for a group #3 sample before and after the treatment of the substrate side.

6.5.2 Detailed studies of additional diamond samples

After the measurement procedures had been established at the first stage of the work, more detailed studies of new diamond samples were carried out. Diamond sample FAP#6 produced by Fraunhofer IAF was studied together with pCVD diamond samples E6#1 and GPI#1 produced by Element Six and by the General Physics Institute (GPI) of the Russian Academy of Science³, respectively. Samples FAP#6 and E6#1 have 500 μm thickness,

³<http://www.gpi.ru>

$1 \times 1 \text{ cm}^2$ metalized area and substrate sides polished away. The samples have a capacitance of about 10 pF and ohmic current-voltage dependences at voltages up to 500 V. The average resistance is $0.4 \cdot 10^{14} \Omega$ for FAP#6 sample and $0.8 \cdot 10^{13} \Omega$ for E6#1 diamond.

Sample GPI#1 has 380 μm thickness. The metalized area is about 0.5 cm^2 . The sample has an ohmic current-voltage dependence and resistance of $0.3 \cdot 10^{15} \Omega$ at voltages up to 500 V. At the level of measurement accuracy, no response to ionizing particles was observed for this sample.

For samples FAP#6 and E6#1 the measurements of the charge collection distance as a function of the applied voltage were done before and after irradiation. Fig. 6.20 (a) shows the results obtained with the non-irradiated FAP#6 diamond sample. During the measurements the voltage was applied with steps of 100 V and four measurements of the CCD were done for every voltage values with 10 min intervals. To avoid accumulation of dose, the ^{90}Sr source was removed after every data taking. The CCD has been found to be stable in time.

After irradiation, when the absorbed dose was about 60 Gy, the measurements were repeated. The results are shown in Fig. 6.20 (b). For every value of the applied voltage a time dependence of the CCD was obtained. During the first 30 min after changing the applied voltage, the CCD is decreasing by about 20%. This effect is reproducible within several days.

Fig. 6.21 (top) shows the CCD measured for the diamond sample during the irradiation as a function of the absorbed dose. The irradiation was carried out with different intensities. The first 10 Gy were accumulated at 0.15 Gy/h dose rate, the rest of time the dose rate was 0.60 Gy/h. In both cases the measurements of the CCD were done at the same irradiation intensities which corresponds to 0.15 Gy/h dose rate. The stabilization of the CCD occurred at about 20 Gy of absorbed dose.

The bottom part of Fig. 6.21 shows the current in the high voltage circuit monitored during the irradiation. The increased irradiation intensity caused a current growth by about one order of magnitude, however, the current stabilized simultaneously with the CCD at the level of 20 nA.

The same set of measurements was done for diamond sample E6#1. Fig. 6.22 shows the CCD measured for increasing voltage at different time after a certain voltage is set. Almost no time dependence was observed before the irradiation, as seen from Fig. 6.22 (a). After the irradiation, as seen from Fig. 6.22 (b), the time dependence was very pronounced. The measurements were repeated in several days after the irradiation with the same result.

The CCD measured for the diamond sample during the irradiation as a function of the absorbed dose is shown in Fig. 6.23. The measurements done at different dose rates show a dependence of the CCD on the irradiation in-

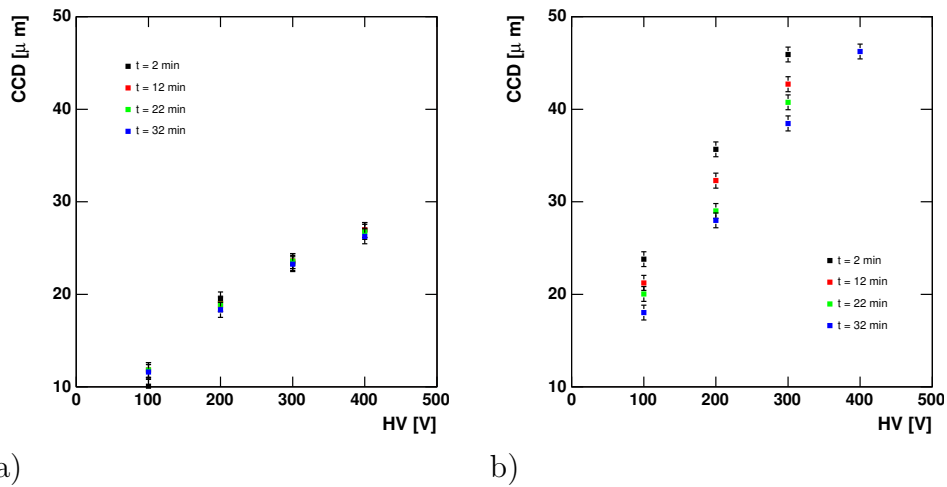


Figure 6.20: The charge collection distance as a function of the applied voltage. The measurements are done in 2, 12, 22 and 32 minutes after the voltage was changed. The results are shown for diamond sample FAP#6 before (a) and after (b) the irradiation.

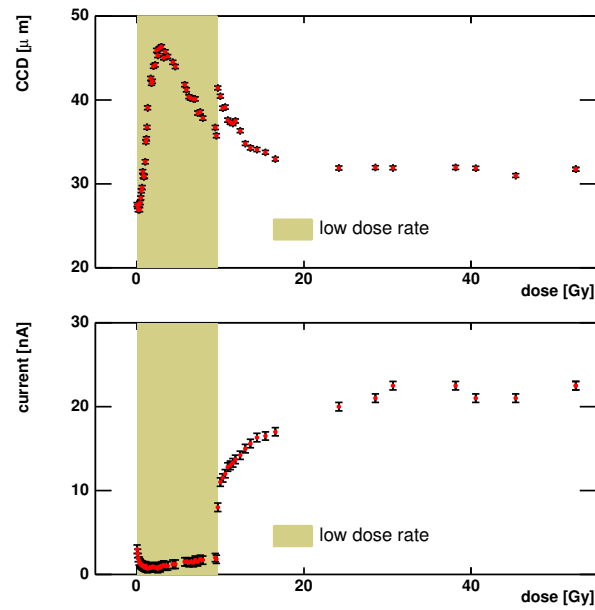


Figure 6.21: The CCD (top) and the current in the high voltage circuit (bottom) as functions of the absorbed dose measured for diamond sample FAP#6. The low dose rate corresponds to 0.15 Gy/h, the rest of measurements are done during irradiation with four times larger intensity. The voltage applied during the irradiation is 400 V.

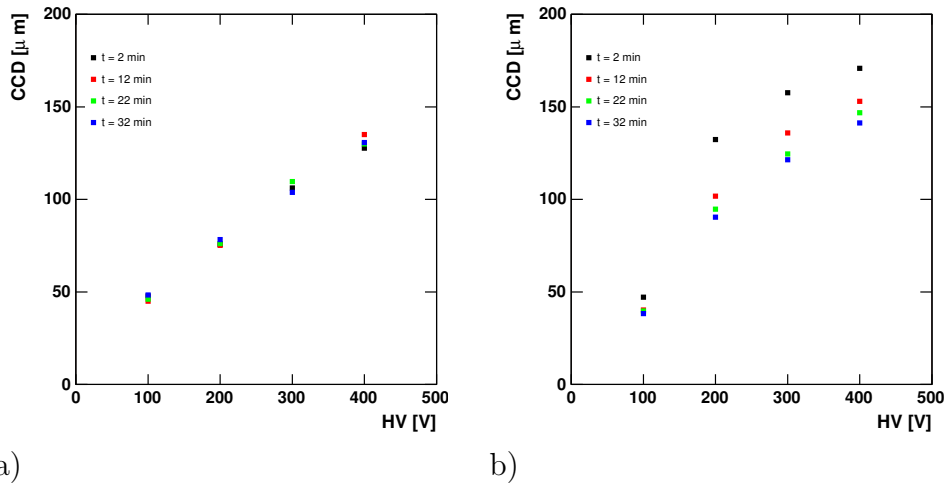


Figure 6.22: The charge collection distance as a function of the applied voltage. The measurements are done in 2, 12, 22 and 32 minutes after the voltage was changed. The results are shown for diamond sample E6#1 before (a) and after (b) the irradiation.

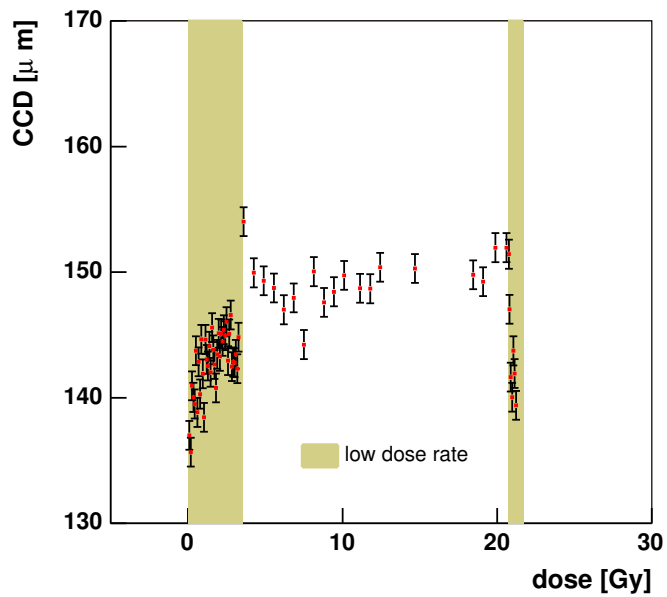


Figure 6.23: The CCD as a function of the absorbed dose measured for diamond sample E6#1. The low dose rate corresponds to 0.15 Gy/h, the rest of measurements are done during irradiation with four times larger intensity. The voltage applied during the irradiation is 400 V.

tensity. The measurements done during irradiation with 0.60 Gy/h dose rate show a CCD increase of about 5% in comparison with the CCD measured under the four times lower irradiation intensity. The current monitored during the irradiation has the stable value of ~ 0.3 nA and does not depend on the dose rate.

6.5.3 Results of Raman spectroscopy and photo - induced luminescence analysis

In order to compare the measurement results and the material properties of the studied diamond samples, Raman spectroscopy (Appendix B.1) and photo-induced luminescence (Appendix B.2) analysis of several samples were done by the Diamond Group of Fraunhofer IAF.

Raman spectroscopy

The Raman spectroscopy was done using an Nd³⁺-YAG laser with 1064 nm wavelength [114] as a source of photons.

Fig. 6.24 shows the Raman spectrum of a group #3 diamond. The broad peak under the diamond line at 1333 cm⁻¹ shows the graphite presence. For a comparison the Raman spectrum of Element Six sample E6#1 is shown in Fig. 6.25.

A quality factor is defined as the ratio of the diamond peak area to the area of the graphite peak. Table 6.4 shows the quality factor determined from the Raman spectra for the investigated samples. The comparison with Table 6.3 and the measurement results for diamonds FAP#6 and E6#1 shows a correlation of the quality factor and the CCD value measured before irradiation. However, the more important characteristic - the stability of sample properties under irradiation - has no correlation with the quality factor. For instance, despite the fact that diamonds of group #2 have the lowest value of the quality factor, they can be operated as detector sensors, whereas group #3 can not stand the irradiation at all.

group #	2		3			4				
sample #	1	3	1	2	3	1	2	3	FAP#6	E6#1
Q.F.	117.7	102.0	329.3	182.4	265.3	508.8	335.6	491.7	705.8	1010

Table 6.4: The quality factor determined from the Raman spectra.

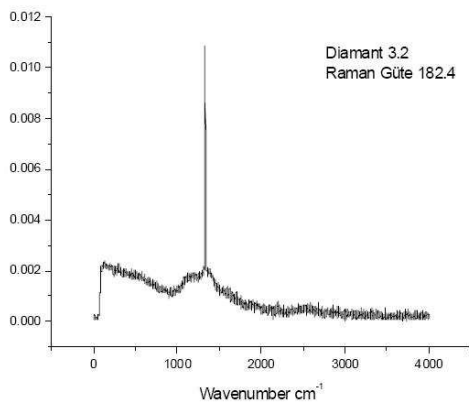


Figure 6.24: The Raman spectrum of a group #3 diamond.

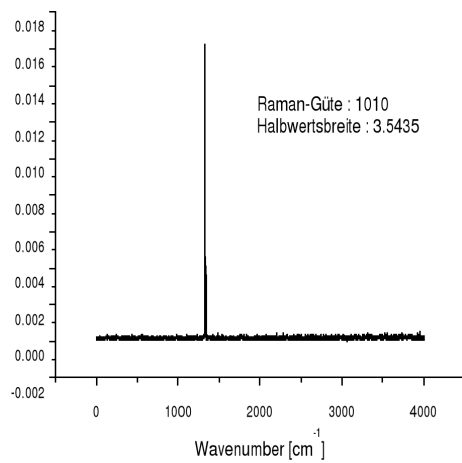


Figure 6.25: The Raman spectrum of E6#1 sample.

Photo-induced luminescence

For the photo-induced luminescence analysis the photoexcitation was done with an argon laser. Fig. 6.26 shows the photoluminescence (PL) spectra of several diamond samples. Diamond sample E6#1 is compared with a reference diamond produced by Fraunhofer IAF. The other two samples are also produced by Fraunhofer IAF and have similar behavior under irradiation as diamonds of group #3.

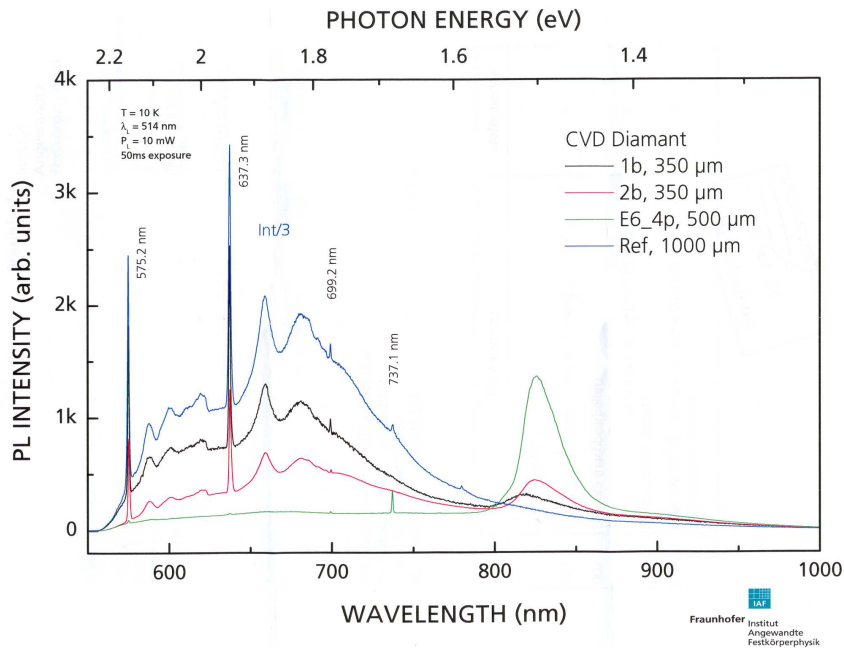


Figure 6.26: The PL spectrum of diamond samples similar to the studied group #3. As a comparison the spectrum of a reference sample is shown along with the PL spectrum of E6#1 diamond sample.

All the samples have a silicon line at 737 nm, that is often obtained for CVD diamonds grown on a silicon substrate. A contamination of nitrogen is seen only for the samples produced by Fraunhofer IAF. The line at 637 nm (1.945 eV) originates from a negative state of a nitrogen-vacancy complex vacancy $[N-V]^-$ [115, 116].

The line at 575 nm (2.155 eV) is considered to represent a nitrogen atom coupled to a double vacancy $[N-V-V]$ [117], or a neutral state of nitrogen-vacancy complex $[N-V]^0$ [116]. No information was found in the literature about the sharp line at 699 nm.

The PL spectra gives information about the states inside the band gap. The broad peak between 550 and 800 nm seen for the Fraunhofer IAF diamonds corresponds to a rich spectrum of such states; this broad peak was not observed for E6#1 sample.

Comparing the PL results for sample E6#1 and the other diamonds to the CCD measurement results, the nitrogen contamination and the states inside the band gap might be considered as possible reasons for a poor signal from diamond sensors.

6.6 Linearity of diamond response

6.6.1 Test set up

As mentioned in Section 3.2.2, the linearity of the Beam Calorimeter response over a wide dynamic range is necessary. Simulation studies have shown that for the TESLA TDR conditions the dynamic range must be approximately between 10 and 10^4 MIPs.

The linearity of the diamond response was tested with a hadron beam of about 4 GeV energy at the T7 beamline of the CERN Proton Synchrotron (PS). The PS was operated in the fast extraction mode delivering bunches of up to 10^7 particles. The bunch length corresponded to about 10 ns of duration.

The testbeam measurements were carried out with a setup similar to the one used for the CCD measurements (Fig. 6.9). Fig. 6.27 shows a photo of the setup at the testbeam area. A shielded box with a diamond sample as well as a trigger box with the scintillator are aligned to the beam axis by means of xy-tables. A plastic scintillator inside the trigger box has a $5 \times 5 \text{ mm}^2$ area and is read out with two PHOTONIS XP1911 photomultiplier tubes [118] via wavelength-shifting fibers. A coincidence of discriminated signals from the photomultipliers produces the trigger signal.

Due to the high intensity of the beam, signals from the diamond samples were fed into the ADC directly, without preamplification. Fig. 6.28 shows an oscilloscope screen-shot taken during a high intensity run. The diamond signal is shown together with the signals from the photomultipliers (PMT 1 and PMT 2). The peak of the diamond signal corresponds to about 2.5 V of voltage drop over 50Ω of the oscilloscope input. To match the ADC range the signals were attenuated during the high intensity runs.

The scintillator response was used as a reference for the linearity measurements. Analog signals from both photomultipliers were digitized with the ADC and gave a relative value of the particle fluence through the scintillator

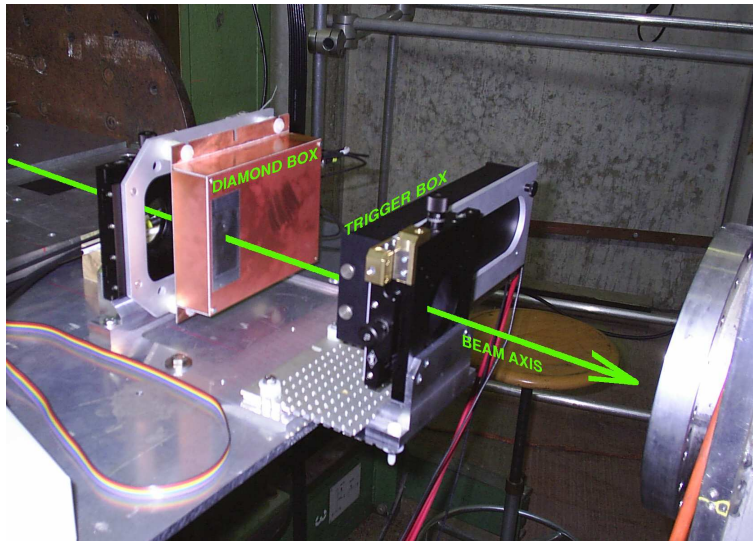


Figure 6.27: A photo of the testbeam setup. A diamond sample is placed in a shielded box and aligned to the beam axis. The trigger box contains a scintillator read out with two photomultipliers via wavelength-shifting fibers.

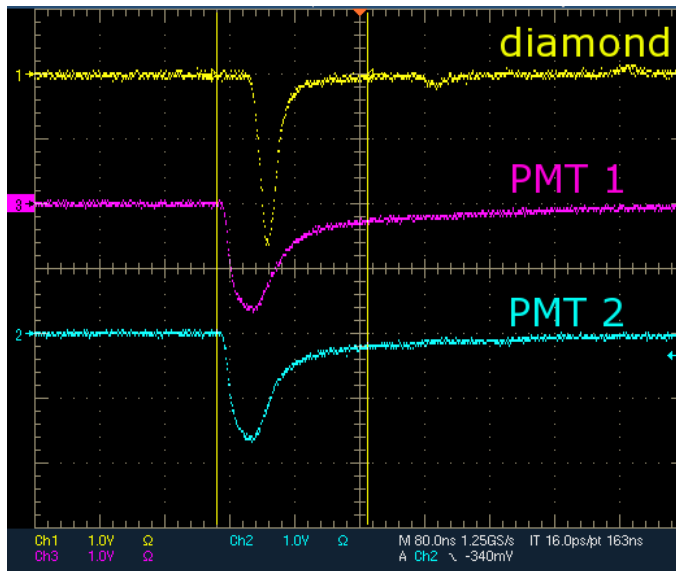


Figure 6.28: The oscilloscope screen-shot shows the signal from a diamond sample (yellow). The signals from two photomultipliers (PMT 1 and PMT 2) are shown in magenta and blue.

for the current bunch.

Since the measurements were performed over a wide range of beam intensity, the high voltages applied to the photomultipliers had to be varied according to the particle fluence to minimize the nonlinearity caused by a possible saturation of the photomultipliers. However, every photomultiplier was operated at the same voltage for at least two different beam intensities. Thus the relative particle fluence can be derived for every bunch tracing through a chain of consecutive runs.

Despite very low operating voltages, a nonlinear response of the photomultipliers due to the saturation was expected in the high intensity runs. To correct the testbeam measurement results for this nonlinearity, the photomultipliers were calibrated after the testbeam.

6.6.2 Calibration of the photomultiplier response

The linearity of the photomultipliers used in the testbeam measurements was studied using an ultra-bright light emitting diode (LED) LU 575 with a luminous intensity of about 12 cd [119]. The LED was operated in a pulsed mode, the duration of the current pulse was chosen to be about 20 ns what is comparable to the time regime at the testbeam. The driver unit of the LED provides a synchronous trigger pulse which was used as a trigger for the ADC. Fig. 6.29 shows the scheme of the calibration setup.

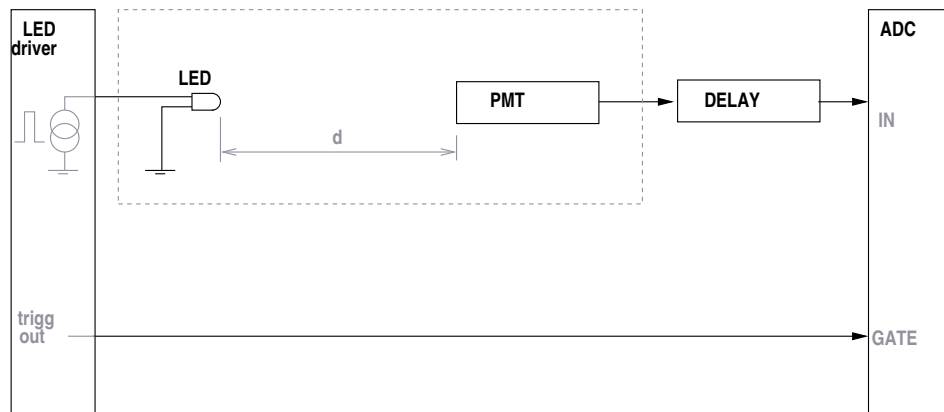


Figure 6.29: A setup for the photomultiplier calibration. An LED is placed in a shielded and optically isolated box together with a photomultiplier (PMT). An LED driver feeds current pulses of about 20 ns duration through the LED and provides synchronous trigger signals. Signals from the photomultiplier are digitized with an ADC.

To measure the phototube response to different light intensities I , the distance d between the LED and the phototube was varied. The intensity of optical photons hitting the photocathode surface of the photomultiplier depends on the distance as $1/d^2$, assuming the LED to be an ideal point light source. Thus

$$I(d) \propto \frac{1}{d^2}, \quad d \gg D_{LED} \quad \text{and} \quad d \gg \frac{R_{PMT}}{\tan \phi_{1/2}},$$

where D_{LED} is the diameter of the light-emitting surface of the LED, R_{PMT} is the photocathode radius of the photomultiplier and $2\phi_{1/2}$ is the half emittance angle of the LED.

Since only relative intensity values can be derived from these measurements, the nonlinearity correction δ is defined as a correction to the response of the photomultiplier at a certain operating voltage HV :

$$\delta(Q, HV) = \frac{Q(HV, d_0)}{d^2} d_0^2 - Q(HV, d),$$

where the reference distance d_0 corresponds to a light intensity small enough not to cause saturation of the phototube and Q is the photomultiplier response in units of ADC channels. The distances d are chosen such as to provide Q in the range of signals obtained during the testbeam measurements.

However, due to the very high light intensity required for the calibration, the measurements had to be done up to small distances $d \sim \frac{R_{PMT}}{\tan \phi_{1/2}}$. To take into account a geometry factor appearing due to the small half emittance angle $2\phi_{1/2} = 30^\circ$ of the LED, control measurements to disentangle the geometrical effects and the nonlinearity of a response for the photomultipliers under calibration were done. The measurements are described in Appendix C and yield a correction factor for the light intensity at small distances.

Calibration results

For both XP1911 phototubes used at the testbeam the measurements of the response to LED light were done for all values of the operating voltage at which the testbeam measurements were carried out. For every value of the applied voltage the phototube response was measured as a function of the distance d . The relative light intensity $I_{REL}(d) = d^2/d_0^2$ was corrected for the geometrical effect. Fig. 6.30 (a) shows the phototube response as a function of the corrected relative intensity. The red line shows the expected linear dependence $Q_{lin}(d) = const \cdot I_{REL}(d)$. The nonlinearity correction δ is the

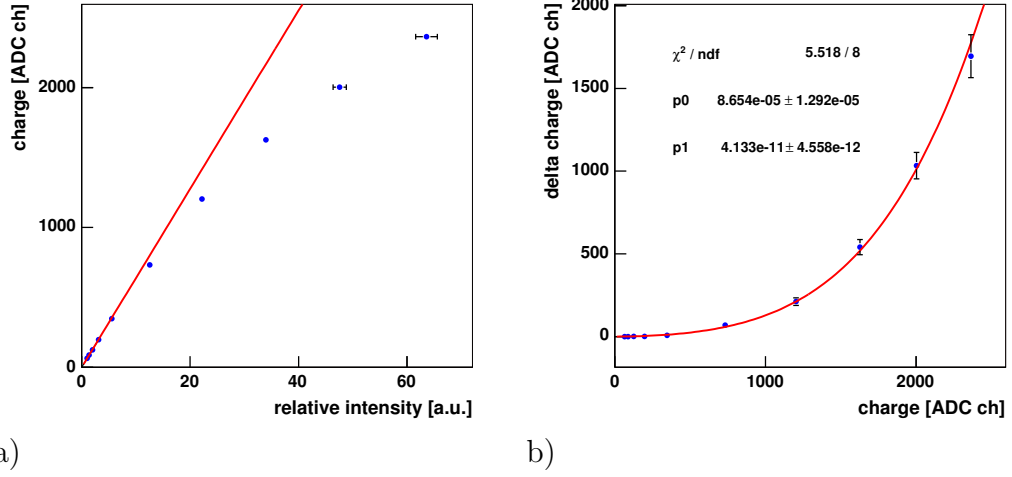


Figure 6.30: a) The phototube response as a function of the relative intensity. The red line shows the extrapolation of the linear photomultiplier response obtained for the low intensity to the higher intensities. b) The nonlinearity correction δ as a function of the measured phototube response. The operating voltage is 500 V.

difference between the expected linear response and the actual values:

$$\delta(Q) = Q_{lin}(d) - Q(d) .$$

The nonlinearity correction as a function of the measured response $\delta(Q)$ is shown in Fig. 6.30 (b). The dependence $\delta(Q)$ was fitted as

$$\delta(Q) = p_0 \cdot Q^2 + p_1 \cdot Q^4 ,$$

where the fit parameters p_0 and p_1 are determined for each photomultiplier and for each voltage setting used in the testbeam measurements.

6.6.3 Testbeam measurement results

The response of both photomultipliers was corrected for the nonlinearity according to the calibration measurements. A certain beam bunch was chosen as a reference. A chain of runs at different intensities was used to calculate the relative values of particle fluence through the scintillator for every bunch. The full range of the relative fluence covered by all runs is between 1 and 120.

Fig. 6.31 shows the signal of one of the phototubes as a function of the calculated relative fluence per bunch (a) and the corresponding deviation from the linear behavior (b). The maximal deviation of about 10% is seen

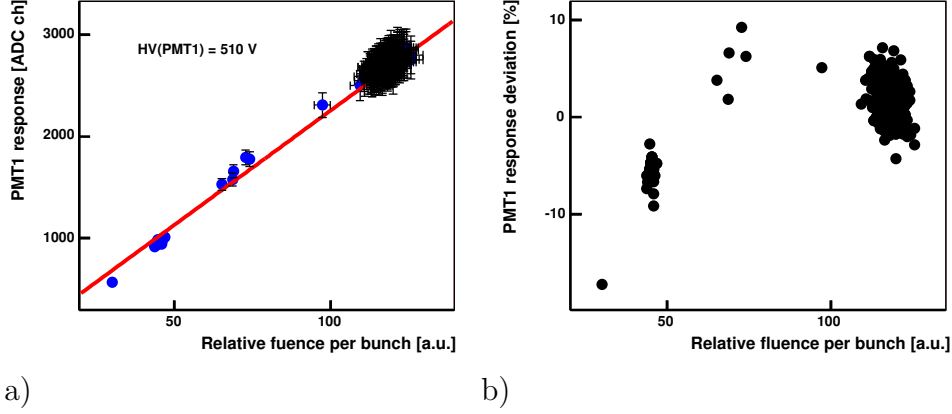


Figure 6.31: Photomultiplier response as a function of the calculated relative fluence (a) and the deviation from a linear fit (b).

for the covered range between 30 and 120 of the relative fluence. Larger deviations are obtained for the low particle fluence. The deviation plot indicates the level of the systematic error in the relative fluence calculations, however does not allow to estimate it for the full range of the operated intensities. The phototube response calibration, described in the previous sections, is the most probable source of the systematic error.

An absolute calibration of the particle fluence was done by the CMS BCM group during the testbeam [120]. The particle fluence was measured for several runs by means of the thermoluminescence dosimetry for a $5 \times 5 \text{ mm}^2$ area centered on the beam axis. The fluence Φ measured for a certain run is proportional to the relative fluences summed for every bunch over the run:

$$\Phi = k \cdot \sum_i \phi_i^{REL},$$

where ϕ_i^{REL} is the relative fluence calculated for the i^{th} bunch and k is the calibration coefficient.

Assuming a homogeneous particle density over the $10 \times 10 \text{ mm}^2$ diamond area, the factor k was found from the calibration runs to be $(2.72 \pm 0.29) \cdot 10^4 \text{ MIP/cm}^2$.

The response of two different diamond samples produced by Fraunhofer IAF (FAP#2.2) and by Element Six (E6#4) as functions of the particle fluence are shown in Fig. 6.32 (a) and (b) respectively. Since diamond sample E6#4 has a 4-pad structure, the diamond response is summed over the pads. The obtained response is fitted to a linear dependence $Q_{diam}(\phi) = p_0 \cdot \phi$. The

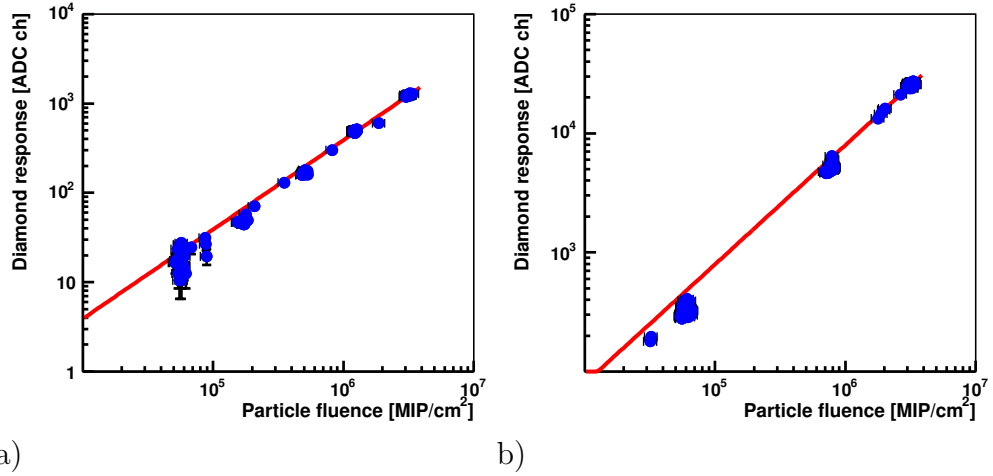


Figure 6.32: The response from FAP#2.2 (a) and E6#4 (b) diamond samples as functions of the particle fluence. The voltage applied to the sensors corresponded to the electric field strength of $2 \text{ V}/\mu\text{m}$ and $0.8 \text{ V}/\mu\text{m}$, respectively.

deviation from the linear behavior does not exceed $\pm 27\%$.

Fig. 6.33 shows three continuous runs with different beam intensities done with E6#4 diamond sample. The particle fluence for every bunch of these runs is shown in Fig. 6.33 (a) as a function of time. Before every run, the voltage applied to the diamond was set to correspond to the $0.8 \text{ V}/\mu\text{m}$ electric field. Fig. 6.33 (b) shows the diamond response normalized to the particle fluence of the corresponding bunch as a function of the time. The mentioned deviation from the linear response is clearly seen for the different runs.

Two possible reasons for the deviation can be considered. First, this might result from the systematic error of the particle fluence calculation. As in the case of the photomultiplier response, shown in Fig. 6.31, the deviations of diamond response from the linear fit are larger at lower particle fluence.

The same time, the beam profile was different for the runs of different intensities. The particle fluence through a diamond sample was calculated from the relative fluence measured with the scintillator of $5 \times 5 \text{ mm}^2$ area centered on the beam axis. The extrapolation to the $10 \times 10 \text{ mm}^2$ area of the diamond samples might also lead to errors in particle fluence calculations.

The slight decrease in the diamond response seen in Fig. 6.33 (b) for individual runs may be caused by the voltage change done before every run. The dependence of a diamond response on the time after a voltage change was already discussed in Section 6.5.2.

The homogeneity of the diamond response is demonstrated in Fig. 6.34.

The signals obtained from each individual pad of E6#4 sample are normalized to the total response from the sensor. The normalized values are shown as a function of time for run #1 discussed above. The stable signals were obtained from all pads. For the careful alignment of the sample in respect to the beam axis, each pad provides about 25% of the total response.

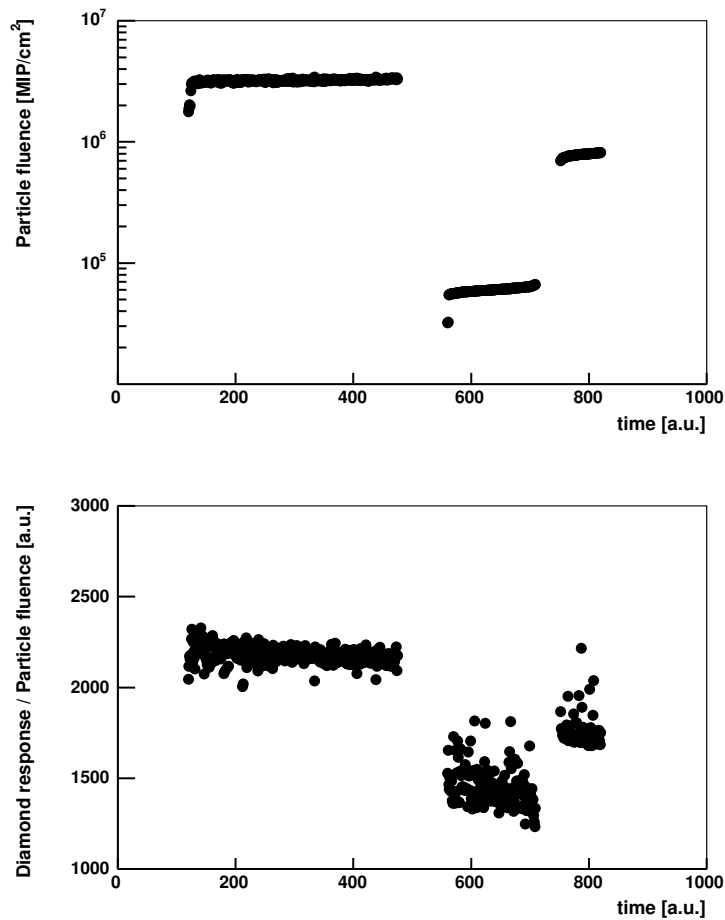


Figure 6.33: Three runs with different beam intensities done with E6#4 diamond sample operated at $0.8 \text{ V}/\mu\text{m}$ electric field. (a) The particle fluence per bunch as a function of time. (b) The diamond response normalized to the corresponding particle fluence as a function of time.

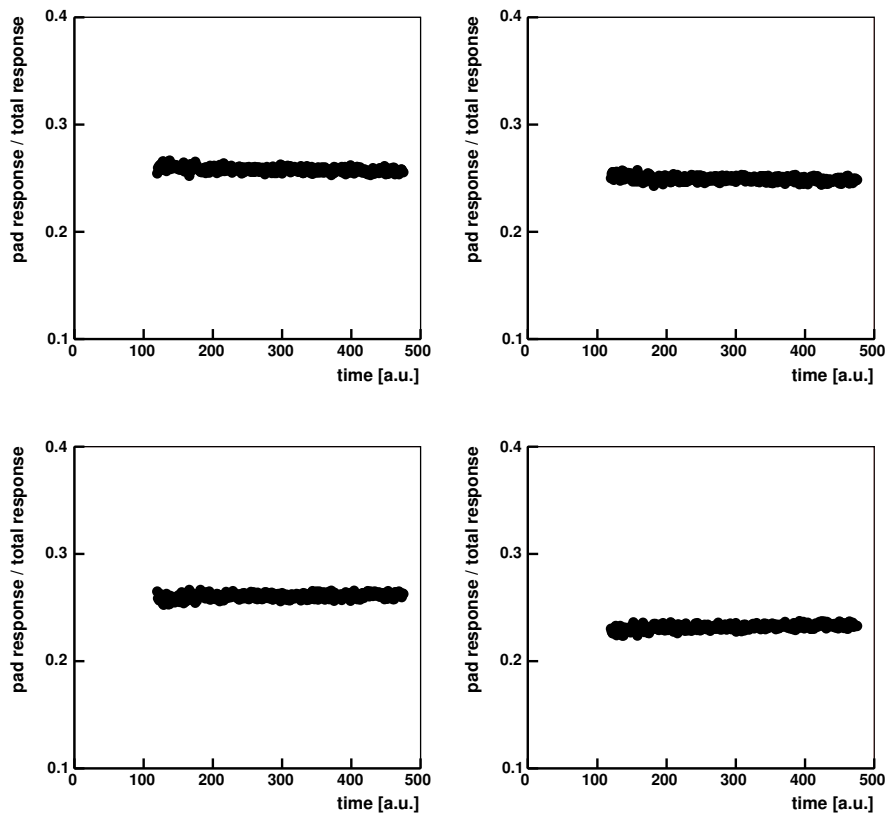


Figure 6.34: The response from individual pads of E6#4 sample normalized to the sum over all pads. The normalized values are shown as functions of time for run #1.

Chapter 7

Summary

The International Linear Collider is being designed to explore particle physics at the TeV scale. This facility would allow to test the mechanism of the electroweak symmetry breaking, to search for new particles and to perform precision measurements of diverse physics parameters.

The instrumentation of the Very Forward Region of the ILC detector is important for the new particle searches and luminosity measurements. Two electromagnetic calorimeters are located there. The LumiCal is purposed for the luminosity measurements. The Beam Calorimeter provides a good hermeticity of the detector measuring high energy electrons, positrons and photons down to very low polar angles, serves for fast beam diagnostics and shields the inner part of the detector from backscattered beamstrahlung remnants and synchrotron radiation.

The e^+e^- pairs originating from beamstrahlung - a new phenomenon at the ILC - cause a huge energy deposition in the BeamCal. This deposition is used for the fast beam diagnostics, but forms a background for the detection of a single high energy electron or photon.

The measurement of a single high energy electron on top of the beamstrahlung background is a challenging task and requires a small Moliere radius and a fine segmentation of the calorimeter. Moreover, due to the harsh radiation condition the BeamCal needs radiation hard active sensors.

Two technologies are studied for the BeamCal: a homogeneous heavy-element crystal calorimeter with optical fiber read out and a diamond-tungsten sampling calorimeter.

The latter one was considered in this work. In the diamond-tungsten option, a Moliere radius of about 1 cm can be reached. CVD diamonds are found to be radiation resistant up to the dose of 10 MGy.

In order to explore the suitability of the diamond-tungsten design for the BeamCal objectives, detailed simulation studies were done. Measurements

on pCVD diamond samples were done to explore their performance for the detection of ionizing particles in a calorimeter.

7.1 Simulation studies

The simulation studies were done for a diamond-tungsten sandwich calorimeter with a fine transverse segmentation of about half a Moliere radius. The TESLA TDR detector design and beam parameters were assumed in the studies. Detection efficiency, energy and angular resolution for electromagnetic showers in the BeamCal were studied.

The efficient detection of electrons with energy of 100 GeV and higher is possible in most of the polar angle coverage of the calorimeter except for several segments strongly affected by the background. Electrons with lower energies can be efficiently detected only at polar angles larger than $\theta \sim 15$ mrad.

The intrinsic energy resolution of the considered calorimeter was estimated to be $\sigma_E/E = 22\%/\sqrt{E}$, where E is expressed in GeV. Under realistic conditions the energy resolution is defined by fluctuations of the beamstrahlung background and depends on the polar and azimuthal angles. The energy resolution can be parameterized as

$$\frac{\sigma_E}{E} = \frac{p_0}{\sqrt{E}} \oplus \frac{p_1}{E},$$

where the coefficients p_0 and p_1 depend on the polar and azimuthal angles and vary in the ranges of from 38 to 360% and from 0 to 1200%, respectively.

The polar angle resolution was found to be at the level of 10^{-4} rad for regions with high detection efficiency. The azimuthal angle resolution at these regions is at the level of 10^{-2} rad. For the high background regions the angular resolution is defined by the calorimeter segment size.

At the simulation level the diamond-tungsten design was found to match the requirements on the BeamCal performance.

Simulation studies have shown that a linear response from the BeamCal is needed in the dynamic range between 10 and 10^4 MIPs for the TESLA conditions.

7.2 pCVD diamond sensor tests

The diamond sensor tests were done with samples of pCVD diamonds produced by Fraunhofer IAF, Element Six and GPI. The main goal of the studies

was to check if the quality of pCVD diamonds corresponds to the requirements on the BeamCal sensor material.

Studies of electrical properties of the diamond samples involved the measurements of the capacitance-voltage and current-voltage characteristics. At this stage the samples with an ohmic behavior and low leakage current were selected.

To characterize the response of the samples to minimum ionizing particles Charge Collection Distance measurements were done. The measurements of the CCD as a function of the electric field strength were done to select diamond samples for further detailed studies. For an electric field of $1 \text{ V}/\mu\text{m}$ the CCD was found to be in the range $5 - 50 \mu\text{m}$ for the Fraunhofer IAF diamonds and about $150 \mu\text{m}$ for the Element Six ones. No response to ionizing particles was observed for the GPI samples.

To explore the stability of a diamond response under electromagnetic radiation the CCD was measured as a function of the absorbed dose up to 50 Gy. For most of pCVD diamonds a stable signal was reached after several Gy of the dose. However, for some of the studied samples a signal deterioration was observed starting with very low doses. A decreasing charge collection efficiency was observed along with a leakage current growth.

The linearity of the response from diamond samples was studied in a test beam. The response of the diamond samples to a particle fluence up to about $10^7 \text{ MIP}/\text{cm}^2$ per bunch was measured. For the explored fluence range the deviation from a linear response was found to be about 30% what is comparable with the level of systematic uncertainty of the fluence calibration.

In order to compare the quality of pCVD diamond material and the detection performance of the studied samples Raman and PL analyses were done for several samples.

From a Raman spectrum a quality factor is defined as the ratio of the diamond peak area to the area of the graphite peak. A correlation of the quality factor and the CCD value measured before irradiation was observed. However, the stability of detection performance under irradiation has no correlation with the quality factor.

The PL spectra have shown nitrogen and silicon contaminations in almost all Fraunhofer IAF samples. For Element Six samples only silicon was detected. A broad range of states inside the band gap was indicated for the Fraunhofer IAF samples and was not observed for the Element Six ones.

7.3 Conclusion

The simulation studies have shown that a diamond-tungsten sandwich calorimeter will match the requirements on the BeamCal performance. The hardware tests have shown pCVD diamond to be an acceptable material for the BeamCal sensors. The diamond sensors produced by Fraunhofer IAF were found to be promising, however more studies have to be done in cooperation with the manufacturer in order to obtain a stable quality.

Appendix A

Fast Beam Diagnostics

The spatial and spectral distributions of both the beamstrahlung photons and the pairs originating from the beamstrahlung photons are sensitive to beam parameters. This gives the possibility for a fast beam diagnostics.

The total energy of beamstrahlung photons is extremely high ($\sim 1.6 \cdot 10^{11}$ GeV per bunch crossing) and their detection will be difficult. In this case the beam diagnostics can be done using the tails of the photon polar angle distribution, detected with a calorimeter placed far downstream of the IP [35].

The beam diagnostics using the pairs originating from the beamstrahlung photons will be done with the BeamCal. The spatial and spectral distributions of the pairs are measured to derive beam parameters. As an example, Fig. A.1 shows the sensitivity of the first radial moment $\langle R \rangle$ of the spatial energy distribution to the horizontal beam size [48]. A radial segmentation of the (xy) -plane at $z = 365$ cm with a segment size of 0.5 cm is assumed and

$$\langle R \rangle = \frac{\sum_i R_i \cdot E_i}{\sum_i E_i}$$

is determined. The sum is taken over all the segments, R_i is the radial coordinate at segment center and E_i is the energy deposition in the segment.

More observables depending on the beam parameters can be introduced, for example, the azimuthal moment, the thrust value, left-right and top-bottom asymmetries of the energy distribution. For a small deviation δx of a beam parameter x from its nominal value x_0 every observable y can be expanded in a Taylor series in the vicinity of x_0 :

$$y(x_0 + \delta x) = y_0 + \partial y / \partial x \cdot \delta x ,$$

where $y_0 = y(x_0)$. The partial derivatives can be obtained from a fit of the corresponding dependencies, like in Fig. A.1. A set (vector) of deviations of

the beam parameters $\delta X = X - X_0$ can be found from the set of measured observables Y using the matrix equation:

$$Y = Y_0 + M \times \delta X ,$$

where M is a matrix of the partial derivatives. Thus

$$\delta X = M^{-1} \times \delta Y ,$$

where $\delta Y = Y - Y_0$.

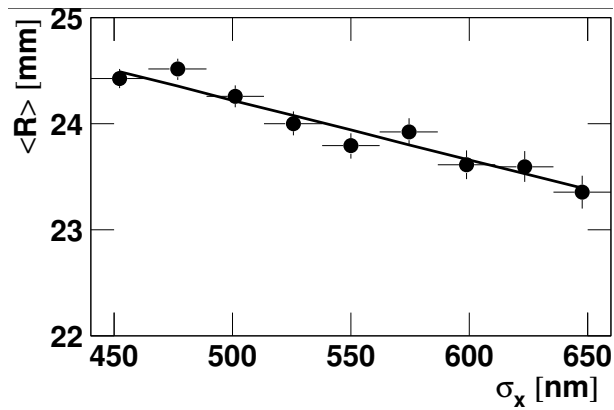


Figure A.1: First radial moment of the beamstrahlung pairs energy as a function of the horizontal beam size σ_x (after Reference [48]).

Table A.1 shows the precision of the parameter determination reached for several beam parameters [121]. The analysis for each single parameter is done keeping all other parameters at their nominal values.

Quantity (x)	nominal value (x_0)	precision
bunch size, σ_x	553 nm	1.2 nm
bunch size, σ_y	5.0 nm	0.1 nm
bunch length	300 μm	4.3 μm
beam offset in x	0	7 nm
beam offset in y	0	0.2 nm

Table A.1: The accuracies reached for several beam parameters from the analysis of the pair energy distributions using the deposition of one bunch crossing. After Reference [121].

Appendix B

Material analysis

B.1 Raman spectroscopy

When monochromatic photons are incident on material, most of them undergo an elastic coherent scattering on atoms or molecules (Rayleigh scattering) and the emitted photon has the same wavelength as the absorbed one. Just a very small fraction (about 1 per 10^5) of the photons are scattered inelastically. This was discovered by C. V. Raman in 1928 [122]. In the case of photon scattering on a crystal, the difference in frequency of the initial photon and the scattered one, or the Raman shift, corresponds to a phonon transition between atomic or molecular vibrational levels. Depending on whether the system has lost or gained vibrational energy, the Raman shift can be positive or negative. These components are called respectively the Stokes and anti-Stokes lines. Since different materials have different vibrational modes, the Raman spectroscopy is a useful technique for material identification.

For diamond the Raman line is 1333.5 cm^{-1} at 149 K and 1332.5 cm^{-1} at 300 K. The temperature broadening, which defines the minimum width of the Raman line, is 1.48 cm^{-1} and 1.65 cm^{-1} at 149 K and 300 K respectively [124].

The existence of chemical impurities and structural defects distorts the lattice vibration levels that causes a broadening and skewing of the Raman line. Under compressive or tensile stress in a sample the Raman line is shifted, respectively, to lower or higher frequency. Thus the Raman spectroscopy provides general information on a sample quality.

The presence of graphite in a diamond causes a strong line at 1580 cm^{-1} , microcrystalline graphite provides also a 1355 cm^{-1} line. Amorphous carbon gives a broad peak between 1100 and 1700 cm^{-1} [76]. The Raman spectra of different carbon allotropes are shown in Fig. B.1.

An example of a Raman spectrum of a graphite-containing diamond sam-

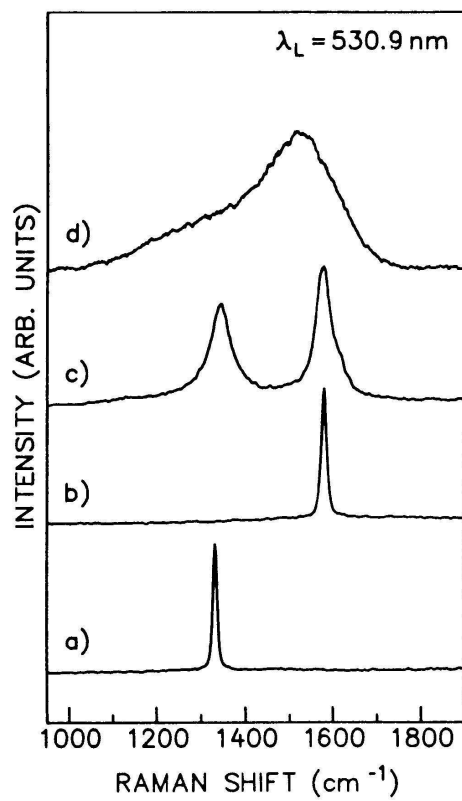


Figure B.1: The Raman spectra of different carbon allotropes (after Reference [123]): a) diamond, b) Highly Oriented Pyrolytic Graphite, c) microcrystalline graphite, d) amorphous carbon.

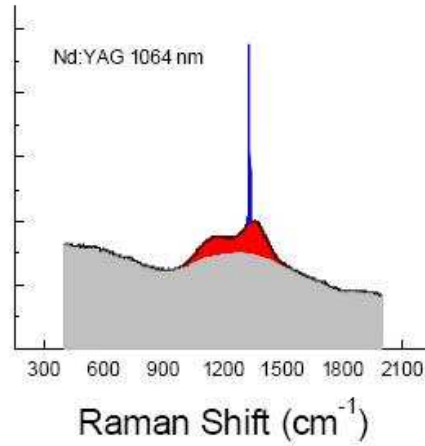


Figure B.2: An example of the Raman spectrum of a polycrystalline diamond. A presence of graphite and disordered carbon causes broadening of the diamond Raman line and corresponds to the red area.

ple is shown in Fig. B.2. The ratio of the diamond peak area to the area of the non-diamond carbon peak is often defined as a quality factor and shows the relative content of non-diamond carbon in the examined sample.

B.2 Photo-induced luminescence

The photoluminescence analysis is based on light excitation of electrons of the material under investigation. The excited electrons may undergo deexcitation to the ground state accompanied with a photon emission. The energy of the emitted light is related to the difference in energy levels between the two electron states, the quantity of the emitted light is related to the relative contribution of the radiative processes.

The information provided by the method may be used for the bandgap width determination since most radiative transitions occur between states in the conduction and valence bands. If a transition from localized states caused by impurities or defects is radiative, an identification of the impurities and defect energy levels is possible.

Appendix C

Correction for a geometry effect of the LED light intensity

To take into account a geometry factor appearing due to the small half emittance angle $\phi_{1/2} = 15^\circ$ of the LED, control measurements of the relative intensity were done with a HAMAMATSU R7400U metal package photomultiplier tube [125]. This photomultiplier has a relatively low quantum efficiency and was expected to have a linear response for intensities used in the calibration. This allows to disentangle the geometrical effects and the nonlinearity of a response for the photomultipliers under calibration.

The measurement setup is discussed in Section 6.6.2. To see the geometry effect a series of measurements with different LED driving currents was done. For each value of the LED current, a response of the reference photomultiplier was measured as a function of the distance d . This allowed to find the LED current value which provides the light intensity low enough that the photomultiplier response stays linear even at small distances.

Fig. C.1 (a) shows the response of the reference photomultiplier as a function of the distance d at different LED currents. Fig. C.1 (b) shows the corresponding normalized intensities

$$\frac{I_{NORM}(d)}{I_{NORM}(d_0)} = \frac{I(d) d^2}{I(d_0) d_0^2} = \frac{Q(d) d^2}{Q(d_0) d_0^2}$$

as functions of the distance. The distance d_0 in this case is chosen large enough that no nonlinearity of the photomultiplier response and no geometry effect are observed.

As seen from Fig. C.1 (b), the intensity reduction at distances between 100 and 400 mm is the same for the low LED currents of 50 and 55 mA. This demonstrates that for the corresponding light intensities the saturation effect is negligible and the intensity reduction in these cases originates from

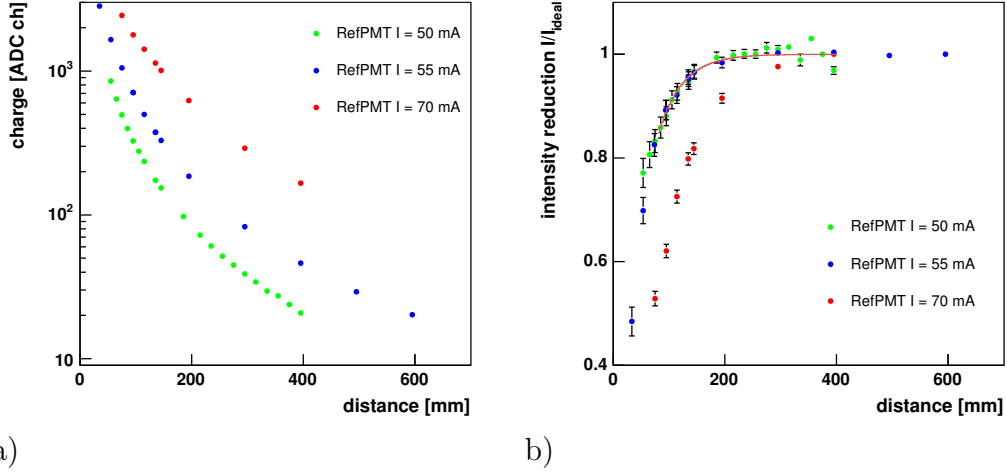


Figure C.1: a) The response of the reference photomultiplier as a function of the distance d at different LED currents. The measurements are done at the same operating voltage of the photomultiplier. b) The corresponding normalized intensities of LED light.

the geometrical effect. The intensity reduction due the geometrical effect was fitted as

$$I_{NORM}(d) = I_{NORM}(d_0) \cdot (1 - e^{-\alpha d}), \quad 100 \text{ mm} \leq d \leq 400 \text{ mm}, \quad \alpha > 0.$$

As an example of the superposition of the geometrical effect and nonlinearity of the photomultiplier response, the results obtained with the higher LED current of 70 mA are also shown in Fig. C.1.

Bibliography

- [1] Sheldon L. Glashow. Partial-Symmetries of Weak Interactions. *Nuclear Physics*, 22:579–588, 1961.
- [2] Steven Weinberg. A Model of Leptons. *Phys. Rev. Lett.*, 19:1264–1266, 1967.
- [3] Abdus Salam. Weak And Electromagnetic Interactions. Originally printed in Svartholm: Elementary Particle Theory, Proceedings Of The Nobel Symposium Held 1968 At Lerum, Sweden, Stockholm 1968, 367–377.
- [4] M. Gell-Mann H. Fritzsch and H. Leutwyler. Advantages of the Color Octet Gluon Picture. *Phys. Lett. B.*, 47:365–368, 1973.
- [5] David J. Gross and Frank Wilczek. Ultraviolet Behavior of Non-Abelian Gauge Theories. *Phys. Rev. Lett.*, 30:1343–1346, 1973.
- [6] H. David Politzer. Reliable Perturbative Results for Strong Interactions. *Phys. Rev. Lett.*, 30:1346–1349, 1973.
- [7] Peter W. Higgs. Broken Symmetries, Massless Particles And Gauge Fields. *Phys. Lett.*, 12:132–133, 1964.
- [8] Peter W. Higgs. Broken Symmetries and the Masses of Gauge Bosons. *Phys. Rev. Lett.*, 13:508–509, 1964.
- [9] G. S. Guralnik, C. R. Hagen, and T. W. B. Kibble. Global Conservation Laws and Massless Particles. *Phys. Rev. Lett.*, 13:585–587, 1964.
- [10] The LEP Electroweak Working Group. Status of Summer 2005. URL <http://lepewwg.web.cern.ch/LEPEWWG>.
- [11] R. Barate et al. Search for the Standard Model Higgs Boson at LEP. *Phys. Lett. B*, 565:61–75, 2003. arXiv.org:hep-ex/0306033.

- [12] D. N. Spergel et al. First Year Wilkinson Microwave Anisotropy Probe (WMAP) Observations: Determination of Cosmological Parameters. *Astrophys. J. Suppl.*, 148:175, 2003. arXiv.org:astro-ph/0302209.
- [13] Yu. A. Golfand and E. P. Likhtman. Extension of the Algebra of Poincare Group Generators and Violation of P Invariance. *JETP Lett.*, 13:323–326, 1971.
- [14] D. V. Volkov and V. P. Akulov. Is the Neutrino a Goldstone Particle? *Phys. Lett. B*, 46:109–110, 1973.
- [15] M. Jacob., editor. *Supersymmetry and Supergravity: A reprint volume of Physics Reports*. World Scientific, 1986.
- [16] P. Bambade, M. Berggren, F. Richard, and Z. Zhang. Experimental Implications for a Linear Collider of the SUSY Dark Matter Scenario. arXiv.org:hep-ph/0406010, 2004.
- [17] J. Erler, S. Heinemeyer, W. Hollik, G. Weiglein, and P. M. Zerwas. Physics Impact of GigaZ. *Phys. Lett. B*, 486:125–133, 2000. arXiv.org:hep-ph/0005024.
- [18] TESLA Technical Design Report, 2001.
- [19] NLC 2003 Configuration Documentation, 2003. URL http://www-project.slac.stanford.edu/lc/local/documentation/2003_Doc.htm.
- [20] GLC Project Report, 2003. URL <http://lcdev.kek.jp/RMdraft>.
- [21] International Technology Recommendation Panel (ITRP) Final Report, September 2004. URL http://www.ligo.caltech.edu/%7Eskammer/ITRP/ITRP_Report_Final2.pdf.
- [22] Gudrid A. Moortgat-Pick et al. The Role of Polarized Positrons and Electrons in Revealing Fundamental Interactions at the Linear Collider. arXiv.org:hep-ph/0507011, 2005.
- [23] P. Bambade, T. Tauchi, and M. Woods. Mashine Detector Interface (MDI) Panel First Report, June 2005. URL http://www.ilcldc.org/meetings/archive/23june2005/MDI_Panel_Report0.4.pdf.
- [24] Pablo Garcia-Abia and Wolfgang Lohmann. Measurement of the Higgs Cross Section and Mass with Linear Colliders. *Eur. Phys. J. direct*, C2, 2000. arXiv.org:hep-ex/9908065.

- [25] T. Barklow. Physics Impact of Detector Performance. Talk at "2005 International Linear Collider Workshop (LCWS05)", Stanford, 2005.
- [26] P. Zerwas. ILC: Physics Scenarios. Talk at "2005 ALCPG & ILC Snowmass Workshop", 2005.
- [27] Wolfgang Lohmann. R & D for a Detector at the International Linear Collider. DESY-05-141, 2005.
- [28] Klaus Mönig. Physics Requirements on Forward Calorimeters for GigaZ and Particle Searches. URL http://www-zeuthen.desy.de/lcdet/Aug_04_WS/talks/moenig_lum04.pdf. Talk at "V Workshop on Instrumentation of the Forward Region of a Linear Collider Detector", 2004.
- [29] Tord Riemann. Forward Bhabha Scattering Theoretical Problems. URL <http://alzt.tau.ac.il/~fcal/talks/TR.pdf>. Talk at "VII Workshop on Instrumentation of the Forward Region of a Linear Collider Detector", 2005.
- [30] GLD detector Concept Study, 2005. URL <http://ilcphys.kek.jp/gld/documents/glddoc>.
- [31] Scetch for a Large Detector Concept, 2005. URL <http://www.ilcldc.org/documents>.
- [32] J. E. Brau, M. Breidenbach, and Y. Fujii. The silicon detector (SiD) and linear collider detector R&D in Asia and North America. DESY-PROC-2004-01. Prepared for 4th ECFA / DESY Workshop on Physics and Detectors for a 90-GeV to 800-GeV Linear e+ e- Collider, Amsterdam, The Netherlands, 1-4 Apr 2003.
- [33] ATLAS Detector and Physics Performance Technical Design Report. LHCC 99-14/15, 1999.
- [34] Alexei Raspereza. Particle Flow Algorithms. Talk at "2005 ALCPG&ILC Snowmass Workshop", 2005.
- [35] U Druhakou et al. R & D of the TESLA-Detector: Instrumentation of the Very Forward Region, 2004. URL http://www.desy.de/f/prc/docs_rd/prc_rd_02_01_update_02_04.pdf. PRC R&D 02/01 status report 02/04.

- [36] G. Abbiendi et al. Precision Luminosity for Z^0 Lineshape Measurements with a Silicon-Tungsten Calorimeter. *European Physical Journal C*, 14:373–425, 2000.
- [37] Halina Abramowicz. Luminosity Measurement. Talk at "2005 AL-CPG&ILC Snowmass Workshop", 2005.
- [38] Achim Stahl. Luminosity Measurement via Bhabha Scattering: Precision Requirements for the Luminosity Calorimeter. URL <http://www-flc.desy.de/lcnotes/notes/LC-DET-2005-004.ps.gz>. LC-DET-2005-004, 2005.
- [39] H. Abramowicz, R. Ingbir, S. Kananov, and A. Levy. Monte Carlo study of a luminosity detector for the International Linear Collider. arXiv.org/physics/0508074, 2005.
- [40] S. Jadach, W. Płaczek, E. Richter-Was, B. F. L. Ward, and Z. Was. Upgrade of the Monte Carlo program BHLUMI for Bhabha scattering at low angles to version 4.04. *Comput. Phys. Commun.*, 102:229–251, 1997.
- [41] S. Jadach, W. Płaczek, and B. F. L. Ward. BHWIDE 1.00: $O(\alpha)$ YFS exponentiated Monte Carlo for Bhabha scattering at wide angles for LEP1/SLC and LEP2. *Phys. Lett. B*, 390:298–308, 1997. arXiv.org/hep-ph/9608412.
- [42] Thorsten Ohl. CIRCE version 1.0: Beam spectra for simulating linear collider physics. *Comput. Phys. Commun.*, 101:269–288, 1997. arXiv.org/hep-ph/9607454.
- [43] Kaoru Yokoya and Pisin Chen. Beam-Beam Phenomena in Linear Colliders. *Lect. Notes Phys.*, 400:415–445, 1992.
- [44] K. A. Thompson and T. O. Raubenheimer. Luminosity for NLC Design Variations. SLAC-TN-04-028, LCC-0014, 1999.
- [45] Daniel Schulte. *Study of Electromagnetic and Hadronic Background in the interaction Region of TESLA*. PhD thesis, University of Hamburg, 1996.
- [46] Karsten Brüßer. Status of the Detector Background Simulations and Comparison of Beamstrahlung Pairs Creation. URL <http://www-flc.desy.de/bdir/meetingagenda190104.html>. Talk at "Crossing Angle Meeting", Zeuthen, 2004.

- [47] T. Behnke et al. Electromagnetic Radiation Hardness of Diamond Detectors. *Nucl. Instrum. Meth. A*, 489:230–240, 2002. arXiv:hep-ex/0108038.
- [48] H. Abramowicz et al. Instrumentation of the Very Forward Region of a Linear Collider Detector. *IEEE Trans. Nucl. Sci.*, 51:2983–2989, 2004.
- [49] Ralph Dollan. Investigation of a Crystal Calorimeter Technology with longitudinal Segmentation. Master’s thesis, Humboldt University of Berlin, 2004.
- [50] T. Behnke et al. *Brahms. A Monte Carlo for a Detector at a 500/800 GeV Linear Collider*. URL http://www-zeuthen.desy.de/linear_collider.
- [51] C. W. Fabian and T. Ludlam. Calorimetry in High-Energy Physics. CERN-EP/82-37, 1982.
- [52] C. Leroy and P. Rancoita. Physics of Cascading Shower Generation and Propagation in Matter: Principles of High-Energy, Ultrahigh-Energy and Compenstaing Calorimetry. *Rept. Prog. Phys.*, 63:505–506, 2000.
- [53] Krammer M. et al. Development of CVD Diamond Radiation Detectors. In *Proc. of VERTEX 97, Rio de Janeiro*, 1997.
- [54] C. E. Nebel. Electronic Properties of CVD Diamond. *Semicond. Sci. Technol.*, 18:S1–S11, 2003.
- [55] E. Berdermann, K. Blasche, P. Moritz, H. Stelzer, and F. Zeytouni. Diamond Detectors for Heavy-Ion Measurements. GSI-PREPRINT-98-23. Talk given at 36th International Winter Meeting on Nuclear Physics, Bormio, Italy, 1998, 1998.
- [56] Jan Isberg, Johan Hammersberg, Erik Johansson, Tobias Wikström, Daniel J. Twitchen, Andrew J. Whitehead, Steven E. Coe, and Geoffrey A. Scarsbrook. High Carrier Mobility in Single-Crystal Plasma-Deposited Diamond. *Science*, 297:1670–1672, 2002.
- [57] H. Yoneda, K. Tokuyama, K. i. Ueda, H. Yamamoto, and K. Bab. High-Power Terahertz Radiation Emitter with a Diamond Photoconductive Switch Array. *Appl. Opt.*, 40:6733–6736, 2001.
- [58] J. Hammersberg, J Isberg, E. Johansson, T. Lundström, O. Hjortstam, and H. Bernhoff. Injection dependent long carrier lifetimes in high quality CVD diamond. *Diamond Relat. Mater.*, 10:574–579, 2001.

- [59] W. Adam et al. Review of the Development of Diamond Radiation Sensors. *Nucl. Instrum. Meth. A*, 434:131–145, 1999.
- [60] W. Adam et al. Developing of Diamond Tracking Detectors for High Luminosity Experiments at LHC. CERN/LHCC 2002-010 LHCC-RD-01, 2002.
- [61] M. Bruinsma et al. Cvd diamonds in the babar radiation monitoring system. physics/0406097, 2006.
- [62] E. Berdermann, K. Blasche, P. Moritz, H. Stelzer, and B Voss. The use of CVD-diamond for heavy-ion detection. *Diamond Relat. Mater.*, 10:1770–1777, 2001.
- [63] E. Berdermann et al. The Diamond Project at GSI - Perspectives. In *Proc. of the 7th Int. Conf. on Advanced Technology and Particle Physics (ICATPP-7), October 2001, Como, Italy*, 2001. URL http://www-wnt.gsi.de/detlab/cvd_status.pdf.
- [64] R. J. Tesarek et al. Performance of a diamond-tungsten sampling calorimeter. *Nucl. Instrum. Meth. A*, 349:96–105, 1994.
- [65] Stuart M. Leeds. *Characterisation of the Gas-Phase Environment in a Microwave Plasma Enhanced Diamond Chemical Vapour Deposition Reactor using Molecular Beam Mass Spectrometry*. PhD thesis, University of Bristol, 1999.
- [66] Hugh O. Pierson. *Handbook Of Carbon, Graphite, Diamond And Fullerenes*. Noyes Publications, Park Ridge, New Jersey, USA, 1993.
- [67] B. V. Derjaguin, D. V. Fedoseev, V. M. Lukyanovich, B. V. Spitzin, V. A. Ryabov, and A. V. Lavrentyev. Filamentary diamond crystals. *J. Cryst. Growth*, 2:380–384, 1968.
- [68] W. G. Eversole, 1958. US Patent 3030187, 3030188.
- [69] John C. Angus, Herbert A. Will, and Wayne S. Stanko. Growth of Diamond Seed Crystals by Vapor Deposition. *J. Appl. Phys.*, 39:2915–2922, 1968.
- [70] Paul W. May. Diamond Thin Films: A 21st Century Material. *Phil. Trans. R. Soc. Lond. A*, 358:473–495, 2000.

- [71] Karl E. Spear and Michael Frenklach. High temperature chemistry of cvd (chemical vapor deposition) diamond growth. *Pure and Appl. Chem.*, 66:1773–1783, 1994.
- [72] L. K. Bigelow and M. P. D’Evelyn. Role of surface and interface science in chemical vapor deposition diamond technology. *Surface Science*, 500: 986–100, 2002.
- [73] James R. Petherbridge. *Diagnostics of Microwave Activated Novel Gas Mixtures for Diamond Chemical Vapour Deposition*. PhD thesis, University of Bristol, 2002.
- [74] URL <http://www.cvd-diamond.com>. Fraunhofer Institute für Angewandte Festkörperphysik, IR/diamond.
- [75] URL <http://www.aixtron.de>. AIXTRON AG.
- [76] Michael Fünér. *Mikrowellen-Plasmareaktoren für die Niederdruck-Diamantabscheidung*. PhD thesis, Albert-Ludwigs-Universität Freiburg i. Brsg., 1999.
- [77] D. S. Dandy and M. E. Coltrin. *Diamond Thin Film Handbook*, chapter 4. Marcel Dekker Inc., NY, USA, 2002.
- [78] W. Piekarczyk. Crystal growth of cvd diamond and some of its peculiarities. *Cryst. Res. Technol.*, 34:553–563, 1999.
- [79] Dirk Meier. *Diamond Detectors for Particle Detection and Tracking*. PhD thesis, University of Heidelberg, 1999.
- [80] A. Mainwood. Point defects in Natural and Synthetic Diamond: What They Can Tell Us about CVD Diamond. *Phys. Stat. Sol.(a)*, 172:25–35, 1999.
- [81] J. P. Goss, P. R. Briddon, R. Jones, and S. Sque. Donor and acceptor states in diamond. *Diamond Relat. Mater.*, 13:684–690, 2004.
- [82] John Y. W. Seto. The electrical properties of polycrystalline silicon films. *J. Appl. Phys.*, 46:5247–5254, 1975.
- [83] E. K. Souw, R. J. Meilunas, C. Szeles, N. M. Ravindra, and F. M. Tong. Photoconductivity of CVD diamond under bandgap and subbandgap irradiations. *Diamond Relat. Mater.*, 6:1157–1171, 1996.

- [84] Mara Bruzzi, Fred Hartjes, Stefano Lagomarsino, David Menichelli, Stefano Mersi, Stefania Miglio, Monica Scaringella, and Silvio Sciortino. Defect analysis of a diamond particle detector by means of photoconductivity and thermal spectroscopy characterization. *Phys. Stat. Sol.(a)*, 199:138–144, 2003.
- [85] M. Nesládek, K. Meykens, L. M. Stals, M. Vaněček, and J. Rosa. Origin of characteristic subgap optical absorption in CVD diamond films. *Phys. Rev. B*, 54(8):5552–5561, 1996.
- [86] F. Lacher, C. Wild, D. Behr, and P. Koidl. Electron field emission from thin fine-grained CVD diamond films. *Diamond Relat. Mater.*, 6: 1111–1116, 1996.
- [87] C. E. Nebel, A. Waltenspiel, M. Stutzmann, M. Paul, and L. Schäfer. Persistent photocurrents in CVD diamond. *Diamond Relat. Mater.*, 9: 404–407, 2000.
- [88] R. M. Hill. *Philos. Mag.*, 23:59, 1971.
- [89] P. Gonon, A. Deneuve, F. Fontaine, and E. Gheeraert. Electrical conduction and deep levels in polycrystalline diamond films. *J. Appl. Phys.*, 78:6633–6638, 1995.
- [90] P. Gonon, Y. Boiko, S. Praver, and D. Jamieson. Poole-Frenkel conduction in polycrystalline diamond. *J. Appl. Phys.*, 79:3778–3780, 1996.
- [91] A. Göhl, B. Günther, T. Habermann, G. Müller, M. Schreck, K. H. Thüerer, and B. Stritzker. Field emission mechanism from undoped chemical vapor deposition diamond films. *J. Vac. Sci. Technol. B*, 18: 1031–1034, 2000.
- [92] Anders Jauhiainen, Stefan Bengtsson, and Olof Engström. Steady-state and transient current transport in undoped polycrystalline diamond films. *J. Appl. Phys.*, 82:4966–4976, 1997.
- [93] B. Fiegl, M. Kuhnert, R. Ben-Chorin, and F. Koch. Evidence for grain boundary hopping transport in polycrystalline diamond films. *Appl. Phys. Lett.*, 65:371–373, 1994.
- [94] S. Ashok, K. Srikanth, A. Badzian, T. Badzian, and R. Messier. Space-charge-limited current in thin-film diamond. *Appl. Phys. Lett.*, 50:763–765, 1987.

- [95] P. N. Murgatroyd. Theory of space-charge-limited current enhanced by Frenkel effect. *J. Phys. D: Appl. Phys*, 3:151–156, 1970.
- [96] S. M. Sze. *Semiconductor devices, physics and technology*. John Wiley, New York, USA, 1985.
- [97] Alexander Oh. *Particle detection with CVD diamond*. PhD thesis, University of Hamburg, 1999.
- [98] T. Tachibana, B. E. Williams, and J. T. Glass. Correlation of the electrical properties of metal contacts on diamond films with the chemical nature of the metal-diamond interface. ii. titanium contacts: A carbide-forming metal. *Phys. Rev. B*, 45(20):11975–11981, May 1992.
- [99] S. Miller, R. Fischer, H. Plank, J. Roth, and V. Dose. Characterization of the temperature dependent phase transition of evaporated Ti films on diamond: Phase identification using maximum entropy data analysis. *J. Appl. Phys.*, 82:3314–3320, 1997.
- [100] T. Tachibana, B. E. Williams, and J. T. Glass. Correlation of the electrical properties of metal contacts on diamond films with the chemical nature of the metal-diamond interface. I. Gold contacts: A non-carbide-forming metal. *Phys. Rev. B*, 45(20):11968–11974, May 1992.
- [101] Gustavo Pastor-Moreno. *Electrochemical Applications of CVD Diamond*. PhD thesis, University of Bristol, 2002.
- [102] L. D. Landau. On the Energy Loss of Fast Particles by Ionisation. *J. Phys. (USSR)*, 8:201, 1944.
- [103] Simon Ramo. Currents induced by electron motion. *Proc. Ire*, 27: 584–585, 1939.
- [104] HP 4263A Precision LCR Meter Operation Manual. Yokogawa-Hewlett-Packard, Ltd.
- [105] URL <http://www.cvd-diamond.com>. Keithley Instruments Inc.
- [106] Harvey Scher and Elliott W. Montroll. Anomalous transit-time dispersion in amorphous solids. *Phys. Rev. B*, 12(6):2455–2477, Sep 1975.
- [107] G. J. Adriaenssens, S. D. Baranovskii, W. Fuhs, J. Jansen, and Ö. Öktü. Photoconductivity response time in amorphous semiconductors. *Phys. Rev. B*, 51(15):9661–9667, Apr 1995.

- [108] S. O. Kasap. The demarcation energy concept in the analysis of charge carrier emission kinetics from deep mobility gap states in amorphous semiconductors. *J. Phys. D: Appl. Phys.*, 21:841–844, 1988.
- [109] URL <http://www.iseg-hv.de>. ISEG Spezialelektronik GmbH.
- [110] W. R. Leo. *Techniques for Nuclear and Particle Physics Experiment*. Springer-Verlag, Berlin, Germany, 1994.
- [111] VV50-3 Ladungssensitiver Vorverstärker, Physikalisches Institut der Universität Heidelberg.
- [112] Specifications of AMPTEK A250 charge-sensitive preamplifier. URL <http://www.amptek.com/a250.html>.
- [113] URL <http://www.caen.it>. CAEN S.p.A.
- [114] J. Wagner, C. Wild, and P. Koidl. Resonance effects in Raman scattering from polycrystalline diamond films. *Appl. Phys. Lett.*, 59:779–781, 1991.
- [115] K. Iakoubovskii, G. J. Adriaenssens, M. Nesládek, and L. M. Stals. Photoluminescence excitation and quenching spectra in CVD diamond films. *Diamond Relat. Mater.*, 8:717–720, 1999.
- [116] K. Iakoubovskii, G. J. Adriaenssens, and M. Nesládek. Photochromism of vacancy-related centres in diamond. *J. Phys.: Condens. Matter*, 12: 189–199, 2000.
- [117] M. C. Rossi, S. Salvatori, F. Galluzzi, F. Somma, and R. M. Montekali. Diamond photoluminescence spectra: Dependence on excitation energy and microstructure. *Diamond Relat. Mater.*, 7:255–260, 1998.
- [118] URL <http://www.photonis.com>. PHOTONIS imaging sensors.
- [119] URL <http://signal-construct.de>. Signal-Construct GmbH.
- [120] D. Chong, L. Fernandez-Hernando, R. Gray, C.J. Ilgner, A.L. Macpherson, A. Oh, T.W. Pritchard, R. Stone, and S. Worm. Validation of synthetic diamond for a beam condition monitor for the compact muon solenoid experiment. *Nuclear Science Symposium Conference Record, 2004 IEEE*, 3:1812– 1815, 2004.
- [121] Achim Stahl. Diagnostics of Colliding Bunches from Pair Production and Beam Strahlung at the IP. URL <http://www-flc.desy.de/lcnotes/notes/LC-DET-2005-003.ps.gz>. LC-DET-2005-003, 2005.

- [122] C. V. Raman. *Nature*, 121:619, 1928.
- [123] Niederdruckabscheidung und Charakterisierung polykristalliner Diamantschichten und Untersuchungen zur Dynamik von Ladungsträgern in HF-Entladungen. Inaugural-Dissertation, Freiburg, 1990.
- [124] S. Zhao. *Characterization of the Electrical Properties of Polycrystalline Diamond Films*. PhD thesis, Ohio State University, 1994.
- [125] HAMAMATSU Manual and final test sheet: Metal Package Photomultiplier Tube R7400U Series, HAMAMATSU PHOTONICS K.K, Electron Tube Center.

Acknowledgements

I am deeply grateful to Dr. Wolfgang Lohmann and Dr. Wolfgang Lange for their support and guidance during these years. I am very thankful to them for sharing their experience and knowledge with me. I would like to express my especial gratitude to Dr. Wolfgang Lohmann for many helpful and very educational discussions and for patient and careful reading of this work.

I would like to thank Dr. Harald Vogt and Dr. Michael Winde for their support and advice on computing. I am very thankful to Konstantin Afanaciev for his assistance on measurements, to Ilia Tsourine for his help and advice on electronics and to Christian Grah for careful reading of this work. I would like to express my gratitude to the staff of the mechanical and electronic workshops of DESY-Zeuthen, especially to Mr. Peter Pohl, Mr. Wolfgang Philipp and Mr. Juergen Pieper. I thank the CMS BCM group for the beam test opportunity.

I would like to thank all members of the LC group in DESY-Zeuthen for very creative and friendly atmosphere, for providing their help whenever I asked for.

I am very grateful to the 'smoking PhD community': Jadranka, Ralph, Karim and Predrag for support, help, discussions and just for being as they are. And I am very much thankful to my mother and to my friends from Petersburg and Gatchina for their patience and strong psychological support.

I would like to thank Deutsches Elektronen-Synchrotron and Dr. Ulrich Gensch for the official support.

Selbständigkeitserklärung

Hiermit erkläre ich, die Dissertation selbständig und nur unter Verwendung der angegebenen Hilfen und Hilfsmittel angefertigt zu haben.

Ich habe mich anderweitig nicht um einen Doktorgrad beworben und besitze einen entsprechenden Doktorgrad nicht.

Ich erkläre die Kenntnisnahme der dem Verfahren zugrunde liegenden Promotionsordnung der Mathematisch-Naturwissenschaftlichen Fakultät I der Humboldt-Universität zu Berlin.

Berlin, 30.11.2005

Ekaterina Kuznetsova.